TÉCNICO LISBOA

Evil Waveform Detection in GNSS AltBOC Signals

Manuel Diogo Marques Pinho Pimentel

Thesis to obtain the Master of Science Degree in

Aerospace Engineering

Supervisor: Prof. Fernando Duarte Nunes

Examination Committee

Chairperson: Prof. Paulo Jorge Coelho Ramalho Oliveira
Supervisor: Prof. Fernando Duarte Nunes
Member of the Committee: Prof. Fernando Manuel Gomes de Sousa

December 2021

Acknowledgments

I would like to thank my supervisor Professor Fernando Nunes, for all the support provided during the development of this work.

I also want to express my gratitude to my family and friends, who have always been there giving me all the support imaginable.

Resumo

A presente dissertação aborda a problemática da deteção de formas de onda maliciosas (EWFs) em sinais AltBOC, utilizados, nomeadamente, na constelação Galileo. Estes sinais são projetados com o objetivo de permitir uma estimação da posição com grande precisão. Como tal, qualquer distorção que possa afetar negativamente o sinal de GNSS tem de ser caracterizada. Com o surgimento de novos sinais de GNSS, vem a necessidade de definir novos modelos de ameaça (TM). A abordagem neste trabalho passa por replicar para os sinais AltBOC o modelo 2OS da ICAO desenvolvido para os sinais de GPS L1 C/A. Dada a complexidade do sinal AltBOC, o recetor pode optar por processar todo o sinal AltBOC, apenas uma das suas sub-bandas ou ambas as sub-bandas de forma independente. É apresentada a computação dos modelos de ameaça para cada uma destas opções de processamento do sinal. Adicionalmente, são descritos várias métricas e testes baseados na arquitetura de multicorreladores. Estes testes são, posteriormente, utilizados para realizar monitorização de qualidade do sinal (SQM) com o objetivo de detetar distorções no mesmo. Por fim, foram realizadas várias simulações com o objetivo de testar o desempenho da monitorização de sinal utilizando cada uma das opções de processamento. Os resultados demonstraram que processar todo o sinal AltBOC apresenta um resultado substancialmente superior às outras opções. Verificou-se também que processando ambas as sub-bandas separadamente se obtém resultados ligeiramente superiores aos do processamento de uma única banda.

Palavras-chave: EWF, Modulação AltBOC, SQM, GNSS, TM

Abstract

This dissertation addresses the problematic of Evil Waveforms (EWFs) detection for AltBOC signals, which are used namely in the constellation Galileo. These signals are designed to enable high precision position estimates. Thus, any signal distortions that can affect the GNSS signal in an hazardous way needs to be characterized. With the emergence of new GNSS signals, comes the need to define new threat models (TMs). The approach in this work is to replicate for the AltBOC signal the 2OS ICAO threat model developed for the GPS L1 C/A. Given the complexity of the AltBOC signal, the receiver can either process the entire AltBOC signal, one sub-band or both sub-bands separately. The computation of the threat models for each processing option is presented. Additionally, several metrics and tests based on a multicorrelator architecture are described. These tests are, subsequently, used to perform signal quality monitoring (SQM) in order to detect signal distortions. Several simulations were conducted to test the performance of monitoring the signal distortions using each one of the processing options. Simulation results showed that processing the whole AltBOC signal heavily outperforms the other options. Processing both sub-bands separately was seen to be slightly superior to the processing of only one sub-band.

Keywords: EWF, AltBOC modulation, SQM, GNSS, TM

Contents

List of Tables

List of Figures

Nomenclature

Greek symbols

Ω	Normalized frequency
σ	Damping factor
θ_{BOC}	BOC Phase
ξ	Normalized damping factor

Roman symbols

$\Im\{\cdot\}$	Imaginary part
$\mathcal{F}\{\cdot\}$	Fourier transform
$\Re\{\cdot\}$	Real part
B_{RF}	Radiofrequency Bandwidth
C/N_0	Signal-to-noise ratio
$E\{\cdot\}$	Expected Value
f_c	Chip frequency
f_d	Ressonant frequency
f_s	Sub-carrier frequency
$G_X(f)$	Power Spectral density of signal X
$H(f)$	Filter frequency response
P_{fa}	Probability of false alarm
P_{md}	Probability of missed detection
$Q\{\cdot\}$	Quantum function
$R_{XY}(\tau)$	Crosscorrelation function of signal X and Y
$R_X(\tau)$	Autocorrelation function of signal X

$sign\{\cdot\}$ Sign function

T_c Chip time

T Correlation interval

Glossary

2OS	2^{nd} - order Step model
8-PSK	8 Phase Shift Keying
ACF	Autocorrelation function
AltBOC	Alternative Binary Offset Carrier
AltLOC	Alternative Linear Offset Carrier
BOC	Binary Offset Carrier
BPSK	Binary Phase Shift Keying
C/A	Coarse/Acquisition
CCF	Crosscorrelation function
CNES	Centre national d'études spatiales
CS	Commercial Service
DLL	Delay Lock-Loop
EWF	Evil Waveform
F/NAV	Freely accessible Navigation Message
GLONASS	Globalnaya Navigatsionnaya Sputnikovaya System
GNSS	Global Navigation Satellite System
GPS	Global Navigation System
HPA	High Power Amplifier
I/NAV	Integrity Navigation Message
ICAO	International Civil Aviation Organization
ICD	Interface Control Document
LFSR	Linear Feedback Shift Registers
LUT	Look-Up Table
MERR	Maximum-allowable Error in Range
NDU	Navigation Data Unit
OS	Open Service
PLL	Phase Lock-Loop
PRN	Pseudo Random Noise
PSD	Power Spectral Density

QPSK	Quadrature Phase Shift Keying
SBT	Side-Band Translation
SQM	Signal Quality Monitoring
SV	Space Vehicle
TM	Threat Model
TS	Threat Space

Chapter 1

Introduction

This chapter is an introduction to the present dissertation, on the research topic ”Evil Waveform Detection in GNSS AltBOC Signals”. The motivation behind the presented topic is addressed in section 1.1. Section 1.2 states the proposed objectives of this work while section 1.3 outlines the dissertation's structure.

1.1 Motivation

Global Navigation Satellite Systems (GNSS) play an important role on the world economy as well as on our everyday life. There are several systems in operation, such as the GPS (American), the Galileo (European Union), the Beidou (China) and the Glonass (Russia) [1, 2]. Their use can range from civil to military applications. Among these applications is civil aviation that requires a very high quality of service for the most demanding phases of flight [3]. Another important use that has been a case of study in the past years are autonomous vehicles (see for instance [4–6]. Both these applications have in common rigid requirements to ensure safety. In order to meet these requirements, any source of potential degradation has to be accounted for.

Ionospheric, tropospheric errors, multipathing, group delay errors, noise and intentional (spoofing and jamming) and non-intentional interference are some of the most common sources of degradation of the signal. These effects have been thoroughly studied and are usually taken account for in the receivers [1, 2].

However, there are other sources of degradation, namely, distortions in the signal caused by a satellite payload failure. These type of distortions are called Evil WaveForms (EWFs). The first occurrence of an EWF failure on a GPS satellite was in 1993 on space vehicle 19 (SV19). It was noted that differential position accuracies without SV19 were less than 50 cm, while using SV19 degraded to anywhere from 2 to 8 meters [7]. Since then, there have been some other minor signal deformation events [8].

Several threat models were proposed to explain the SV19 event. The preferred threat model was ”2^{nd} - order Step” (2OS). Not only is this model able to explain the SV19 failure but also generates causal waveforms making it more plausible for future failure modes of the satellite signal generating

hardware [9]. This model can be subdivided into three classes of failure modes: digital (threat model A, TM-A), analog (threat model B, TM-B) and combination of both of them (threat model C, TM-C). This proposition has been adopted by ICAO for the GPS/GLONASS C/A code signal [10]. Ever since, many other articles have been published on this subject, more specifically, on the extension of this model to the new modernized GNSS signals [11–15].

In order to detect these distortions, signal quality monitoring (SQM) architectures have been developed. The initial research on EWFs detection was performed by Phelts in [16] where a multicorrelator technique to detect GPS C/A EWFs is presented. This technique consists of using several correlator outputs to create metrics. These metrics are then compared with their nominal value in order to create tests. Over the last few years, there has been several work published on signal quality monitoring for new modernized GNSS signals [6, 17–19]. Most of this work is based on the multicorrelator technique.

Due to the complexity of the AltBOC modulation, the formulation of the 2OS model for this signal is a challenging task. In fact, as far as the author is aware, there isn't any work published on this subject. In general, the receiver designer can choose among 3 options for processing the AltBOC signal: (i) process the entire AltBOC signal as a wideband 8-phase signal; (ii) process both sub-bands, but separately; (iii) process only one of the sub-bands [2]. This dissertation provides a comparative performance analysis between the use of each processing option for SQM of EWFs.

1.2 Objectives

The main objective of this work is the performance comparison between the SQM using each processing option. For that matter, it is necessary to first extend the 2OS model presented in the literature for the AltBOC signal.

The objectives of this work are now enumerated:

- Gain insight into the AltBOC modulation
- Extend the 2OS model for the AltBOC modulation
- Implement a SQM architecture using the multicorrelator technique
- Devise several simulation scenarios to study the performance of the SQM architecture
- Compare the results obtained with the three processing options

1.3 Thesis Outline

This document consists of 7 chapters and 5 appendices.

- Chapter 2 provides a theoretical background on the Galileo E5 AltBOC signal, addressing how it was derived from the BOC modulation and listing the characteristics of the signal mainly obtained from the official Interface Control Document (ICD) [20].

- Chapter 3 introduces the different receiver architectures for processing the AltBOC signal.
- Chapter 4 contains the extension of the 2OS model for the AltBOC signal. The analytical computation of the correlation expressions for each threat model is presented.
- In chapter 5 the SQM techniques used to detect the anomalous signals are presented. A statistical analysis of the employed metrics and tests is developed.
- In chapter 6 the metrics and tests introduced in chapter 5 are tested to detect the presence of the signal distortions described in chapter 4.
- Finally, in chapter 7, the conclusions drawn from this work are reported, alongside some suggestions for future work.
- Appendix A computes the cross-correlation between two rectangular pulses; appendix B presents an extension of the error model of chapter 4 for threat model TM-A1; appendix C addresses the method with which we can generate vectors of correlated noise; appendix D provides an in-depth statistical analysis of the tests presented in chapter 5; appendix E develops a halt criterion to compute the required number of Monte Carlo runs to obtain a desired confidence interval.

Chapter 2

Galileo E5 AltBOC Signal

In this chapter, we will define and characterize the AltBOC(15,10) modulation used in Galileo E5 and Beidou B2 bands, which will be used in the threat models and the signal quality monitoring architectures developed in this work. The AltBOC(15,10) modulation was first suggested in 2000. At that time, the Galileo signal plan was being discussed and there was the need to transmit 2 independent signals in two close bands using an unique High Power Amplifier (HPA). In fact, since each signal would be composed of a pilot and a data channel, a 4-code AltBOC would have been needed. A 4 code AltLOC was studied at the time but ended up not being used because its envelope was not constant. It is really important that a modulation has constant envelope so that the HPA can be used at saturation (leading to an higher efficiency). Later on, in 2001, CNES discovered that a 4 code constant AltBOC signal is possible and this is the AltBOC that was proposed for the E5a and E5b bands [21].

Nowadays, this modulation is used both in the Galileo E5 signal and BeiDou B2 signal [2]. In this dissertation, the Galileo E5 signal is explored due to larger amount of information available.

There are some advantages in using AltBOC over other modulations [22]. Firstly, it greatly simplifies the baseband generator of the satellite since it uses only a wideband modulator for the entire E5 band instead of two separate QPSK modulators for E5a and E5b. Besides that, it permits to use the amplifier in the saturation region (due to the AltBOC constant envelope) which makes it much more efficient. Furthermore, it allows for an optimization of the receiver architecture because the receiver can demodulate simultaneously the navigation data in E5a and E5b sidebands. Finally, it has been shown in [23] that wideband signals perform better in the presence of noise and multipath than narrow band signals.

Section 2.1 introduces the BOC modulation that serves as a baseline to AltBOC. Section 2.2 defines the Standard AltBOC modulation while section 2.3 presents the AltBOC modulation used in E5 signal. Section 2.4 presents an equivalent signal representation. Finally, section 2.5 determines the autocorrelation function (ACF) and power spectral density (PSD) of the E5 AltBOC signal.

2.1 BOC modulation

An accurate definition of AltBOC modulation was given in [24]: "An Alternative-BOC signal is a BOC-like signal having different PRN codes in the lower and upper main split lobes. Alternative-BOCs allow one signal service per lobe". Therefore, in order to understand AltBOC, one needs to study BOC first.

Consider $s(t)$ as a combination of the binary data message $d(t)$, with symbol period T_d, and the chips of the PRN code $c(t)$, with a chip period T_c ($T_d > T_c$), as follows

$$s(t) = d(t)c(t) \tag{2.1}$$

with $d(t)$,$c(t) \in \{-1, 1\}$.

The BOC(m, n) modulated signal is obtained by multiplying $s(t)$ by a rectangular subcarrier. This rectangular subcarrier can be obtained by computing the signal of a sinusoidal function with frequency $f_s = m \times 1.023$ MHz:

$$sc(t) = \text{sign}\{\sin(2\pi f_s t)\} \tag{2.2}$$

with the function $\text{sign}\{x\}$ given by

$$\text{sign}\{x\} = \begin{cases} -1, & x < 0 \\ 0, & x = 0 \\ +1, & x > 0 \end{cases} \tag{2.3}$$

A period of the subcarrier is illustrated in Fig. 2.1. The subcarrier frequency is usually equal or greater than the chip rate, $f_c = \frac{1}{T_c} = n \times 1.023$ MHz. We can define the BOC ratio as

$$k = \frac{2m}{n} \tag{2.4}$$

This parameter represents the number of half periods of the subcarrier that fit in a code chip and is of great importance when analyzing this modulation (see [25]).

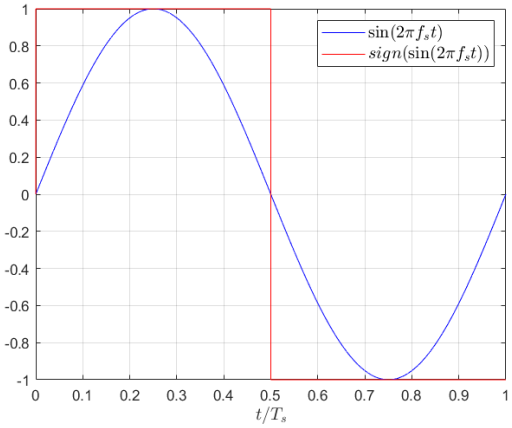

Figure 2.1: Subcarrier function for BOC modulation.

In Fig. 2.1 we have assumed a BOC phase $\theta_{BOC} = 0$. Typically, it is assumed that if no phasing is indicated explicitly, it is a sine-phased BOC. Likewise, there is also the cosine-phased BOC, indicated by BOC_c, for $\theta_{BOC} = \pi/2$ [2].

The ACF of a BOC(m,n) signal is [26]

$$R_{\mathrm{BOC(m,n)}}(\tau) = \Lambda_{T_c/k}(\tau) + \sum_{p=1}^{k-1}(-1)^p \left(1 - \frac{p}{k}\right) \Lambda_{T_c/k}\left(|\tau| - p\frac{T_c}{k}\right) \tag{2.5}$$

The corresponding PSD can be obtained computing the Fourier Transform of Eq. 2.5 and is as follows [26]

$$G_{\mathrm{BOC(m,n)}}(f) = T_c \mathrm{sinc}^2(fT_c) \tan^2\left(\frac{\pi f T_c}{k}\right) \tag{2.6}$$

A comparison between the PSD of the signal $s(t)$ before and after the BOC(1,1) modulation is represented in Fig. 2.2. It is shown that the modulation splits the spectrum into two symmetrical parts. Furthermore, there is no power at the central frequency and the main lobes are shifted to the subcarrier frequency, $\pm f_s$. This means that with a proper choice of the BOC parameters it is possible to achieve sufficient spectral separation to allow multiple signals to share the same band with minimal loss and interference [22].

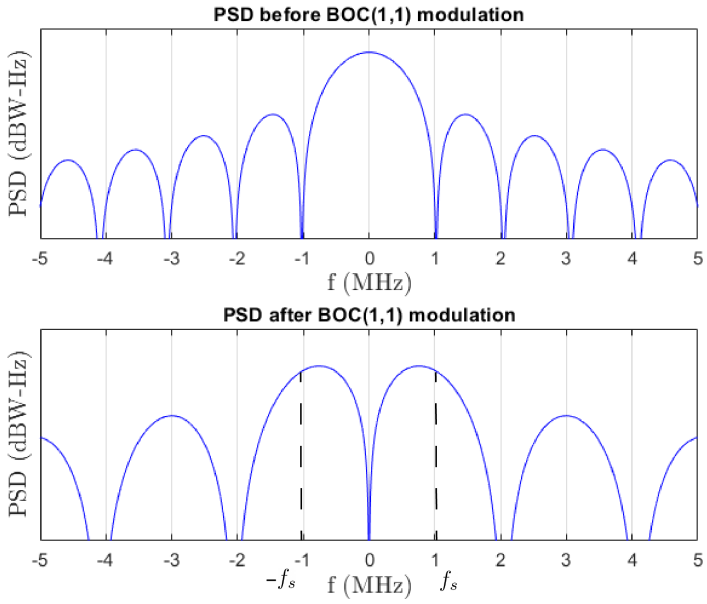

Figure 2.2: PSD of $s(t)$, before (above) and after (below) the BOC Modulation.

2.2 Standard AltBOC modulation

The idea behind the Standard AltBOC is to perform the same operation as in the BOC modulation but using complex rectangular subcarriers instead. To understand this concept, it is important to first introduce the Complex-BOC modulation.

Considering the same baseband signal in Eq. 2.1, the Complex-BOC modulation can be obtained by multiplying it by the following complex subcarrier:

$$sc(t) = \text{sign}\{\cos(2\pi f_s t)\} + j\text{sign}\{\sin(2\pi f_s t)\} \tag{2.7}$$

This subcarrier has a similar performance to the complex exponential, $\exp(j2\pi f_s t) = \cos(2\pi f_s t) + j\sin(2\pi f_s t)$. However, their power spectrum is slightly different. While the spectrum of the complex exponential is a delta function centered at f_s, the subcarrier $sc(t)$ has infinite harmonics (see, for instance, [25]).

A representation of the power spectrum before and after the modulation is applied is shown in Fig. 2.3. Notice how the baseband signal $s(t)$ is frequency shifted to the frequency f_s. Furthermore, there is also a second lobe that appears at $-3f_s$ due to the harmonics of the subcarrier. However, this second lobe has much lower amplitude than the main peak, thus, being neglectable. As stated before, besides the lobe at $-3f_s$ there are other higher frequency harmonics that, for the sake of simplicity, were not represented. It can be concluded that, while the BOC modulation splits the spectrum into two symmetrical parts centered at $\pm f_s$, Complex-BOC shifts the power spectrum by f_s. Even though it was only represented a shift to a higher frequency, the same could be done for a lower frequency taking instead the conjugate of the subcarrier, $sc^*(t)$.

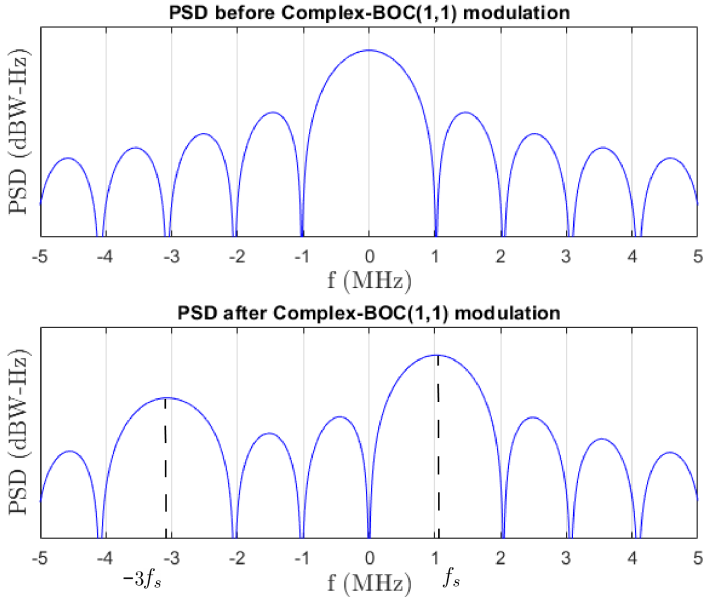

Figure 2.3: PSD of $s(t)$, before (above) and after (below) the Complex-BOC Modulation.

This technique is used by Standard AltBOC to transmit four channels (E5a-I, E5a-Q, E5b-I, E5b-Q) in two separate sidebands (E5a and E5b). Each sideband contains two channels that are allocated in the in-phase channel (E5a-I/E5b-I) and in the quadrature channel (E5a-Q/E5b-Q). The binary signal components for each channel are [20]:

$$
\begin{aligned}
e_{E5a-I} &= d_1 c_1 \\
e_{E5a-Q} &= c_2 \\
e_{E5b-I} &= d_2 c_3 \\
e_{E5b-Q} &= c_4
\end{aligned}
\tag{2.8}
$$

The quantities $e_{E5a-I} \in \{-1, +1\}$ and $e_{E5b-I} \in \{-1, +1\}$ are data sequences plus independent code while $e_{E5a-Q} \in \{-1, +1\}$ and $e_{E5b-Q} \in \{-1, +1\}$ are independent code (dataless) sequences. The Standard AltBOC can be obtained combining the signal components of Eq. 2.8 as follows:

$$
s_{\text{Standard-AltBOC}}(t) = [e_{E5a-I} + j e_{E5a-Q}] sc^*(t) + [e_{E5b-I} + j e_{E5b-Q}] sc(t) \tag{2.9}
$$

Similarly to what was seen for the Complex-BOC, the Standard AltBOC modulation shifts the E5a components to a lower frequency and the E5b components to a higher one. This modulation can be written in terms of the equivalent expression [24]:

$$
s_{\text{Standard-AltBOC}}(t) = A_k \exp(jk(t)\pi/4) \tag{2.10}
$$

where

$$
A_k = \begin{cases} 0 & \text{if } k(t) = 0 \\ 2\sqrt{2} & \text{if } k(t) \text{ is odd} \\ 4 & \text{if } k(t) \text{ is even} \end{cases} \quad , \; k(t) \in \{0, 1, 2, 3, 4, 5, 6, 7, 8\} \tag{2.11}
$$

The corresponding scattered plot is presented in Fig. 2.4 for $m = 15$ and $n = 10$. It can be seen that this modulation doesn't have a constant envelope. This is a problem for satellite communications because amplifiers need to work in the saturation level to obtain the best efficiency and minimum distortions. If the signal does not have constant envelope, this is not possible.

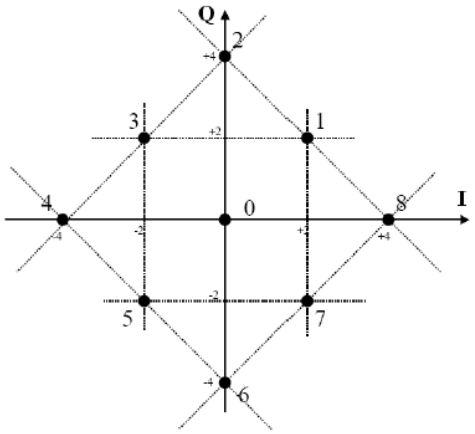

Figure 2.4: Scattered plots for Standard AltBOC with $m = 15$ and $n = 10$ [24].

2.3 E5 AltBOC(15,10)

The modulation adopted for the Galileo E5 signal is a modified version of the Standard AltBOC, with some changes in order to obtain a constant envelope. This modulation uses the same notation as BOC. It is denoted AltBOC(15,10) as it uses a $f_s = 15 \times 1.023$ MHz and $f_c = 10 \times 1.023$ MHz.

The E5 complex baseband signal is generated according to Fig. 2.5. As we can see, only the in-phase components have data bits in their composition, the quadrature components are only used as pilot codes.

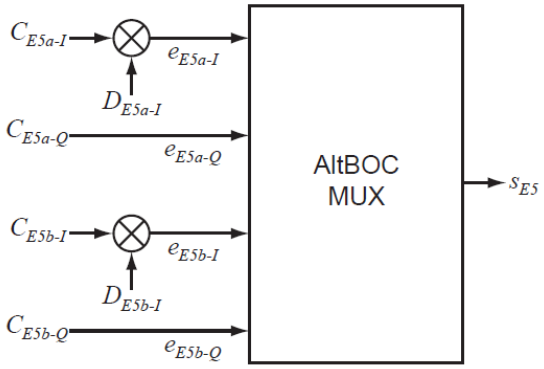

Figure 2.5: Modulation Scheme for the E5 Signal [20].

It is composed by four signal components that are generated according to:

- e_{E5a-I} from the F/NAV navigation data stream D_{E5a-I} modulated with the ranging code C_{E5a-I}
- e_{E5a-Q} (pilot component) from the ranging code C_{E5a-Q}
- e_{E5b-I} from the I/NAV navigation data stream D_{E5b-I} modulated with the ranging code C_{E5b-I}
- e_{E5b-Q} (pilot component) from the ranging code C_{E5b-Q}

The F/NAV type of message is used in the OS (Open Service) while I/NAV is employed in the OS and CS (commercial service). The analytical expression for each one of the components is

$$\begin{aligned}
e_{E5a-I} &= \sum_{i=-\infty}^{+\infty} \left[c_{E5a-I,|i|_{L_{E5a-I}}} d_{E5a-I,[i]_{DC_{E5a-I}}} \Pi_{T_c}(t - iT_c) \right] \\
e_{E5a-Q} &= \sum_{i=-\infty}^{+\infty} \left[c_{E5a-Q,|i|_{L_{E5a-Q}}} \Pi_{T_c}(t - iT_c) \right] \\
e_{E5b-I} &= \sum_{i=-\infty}^{+\infty} \left[c_{E5b-I,|i|_{L_{E5b-I}}} d_{E5b-I,[i]_{DC_{E5b-I}}} \Pi_{T_c}(t - iT_c) \right] \\
e_{E5a-I} &= \sum_{i=-\infty}^{+\infty} \left[c_{E5b-Q,|i|_{L_{E5b-Q}}} \Pi_{T_c}(t - iT_c) \right]
\end{aligned} \tag{2.12}$$

where the rectangle function is defined as:

$$\Pi_L(t) = \begin{cases} 1, & 0 \leq t \leq L \\ 0, & \text{otherwise} \end{cases} \tag{2.13}$$

The wideband E5 signal is generated with the AltBOC modulation and can be represented with the following expression [20]

$$\begin{aligned} s_{E5}(t) = & \frac{1}{2\sqrt{2}} \left(e_{E5a-I} + je_{E5a-Q}\right) \left[sc_{E5-S}(t) - jsc_{E5-S}(t - T_s/4)\right] \\ & \frac{1}{2\sqrt{2}} \left(e_{E5b-I} + je_{E5b-Q}\right) \left[sc_{E5-S}(t) + jsc_{E5-S}(t - T_s/4)\right] \\ & \frac{1}{2\sqrt{2}} \left(\overline{e}_{E5a-I} + j\overline{e}_{E5a-Q}\right) \left[sc_{E5-P}(t) - jsc_{E5-P}(t - T_s/4)\right] \\ & \frac{1}{2\sqrt{2}} \left(\overline{e}_{E5b-I} + j\overline{e}_{E5b-Q}\right) \left[sc_{E5-P}(t) + jsc_{E5-P}(t - T_s/4)\right] \end{aligned} \tag{2.14}$$

The dashed signal components in Eq. 2.14 represent the product signals and are used to make the envelope of the signal constant [22]. They are defined as:

$$\begin{aligned} \overline{e}_{E5a-I} &= e_{E5a-Q}e_{E5b-I}e_{E5b-Q} \\ \overline{e}_{E5a-Q} &= e_{E5a-I}e_{E5b-I}e_{E5b-Q} \\ \overline{e}_{E5b-I} &= e_{E5b-Q}e_{E5a-I}e_{E5a-Q} \\ \overline{e}_{E5b-Q} &= e_{E5b-I}e_{E5a-I}e_{E5a-Q} \end{aligned} \tag{2.15}$$

The subcarriers $sc_{E5-S}(t)$ and $sc_{E5-P}(t)$ are the four-level single and product subcarriers, respectively, and are represented by:

$$\begin{aligned} sc_{E5-S}(t) &= \sum_{i=-\infty}^{+\infty} AS_{|i|_8} \Pi_{T_{s,E5}/8}(t - iT_s/8) \\ sc_{E5-P}(t) &= \sum_{i=-\infty}^{+\infty} AP_{|i|_8} \Pi_{T_{s,E5}/8}(t - iT_s/8) \end{aligned} \tag{2.16}$$

Each subcarrier has a frequency $f_s = 1.5f_c = 15.345$ MHz $(15 \times 1.023$ MHz) and the AS_i and AP_i coefficients are given in table 2.1.

Table 2.1: AltBOC subcarrier Coefficients [20].

i	0	1	2	3	4	5	6	7
$2 \cdot AS_i$	$\sqrt{2}+1$	1	-1	$-\sqrt{2}-1$	$-\sqrt{2}-1$	-1	1	$\sqrt{2}+1$
$2 \cdot AP_i$	$-\sqrt{2}+1$	1	-1	$\sqrt{2}-1$	$\sqrt{2}-1$	-1	1	$-\sqrt{2}+1$

Eq. 2.16 with coefficients given by table 2.1 results in the subdivided leveled sinusoidal kind of wave shown in Fig. 2.6. From the comparison of subcarrier functions for single and product signals, the

relative power in the product signals is roughly 15% [27].

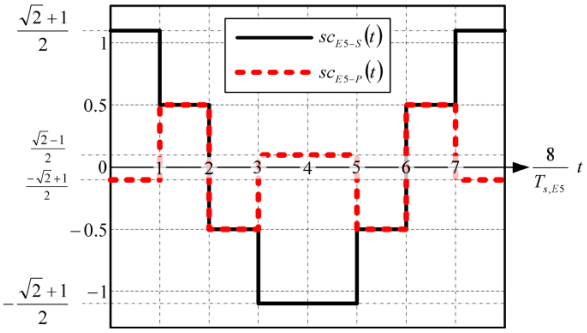

Figure 2.6: One Period of the Two subcarrier Functions Involved in AltBOC Modulation [20].

2.4 Equivalent Modulation Type

The rather complex modulation scheme in Eq. 2.14 can also be described as an 8-PSK signal defined by Eq. 2.17. This representation allows to generate the signal using a simple Look-Up Table (LUT) for phase assignments and greatly reduce the hardware complexity [22]. The corresponding phase states are illustrated in Fig. 2.7

$$s_{E5}(t) = \exp\left(j\frac{\pi}{4}k(t)\right) \quad \text{with} \quad k \in \{1,2,3,4,5,6,7,8\} \tag{2.17}$$

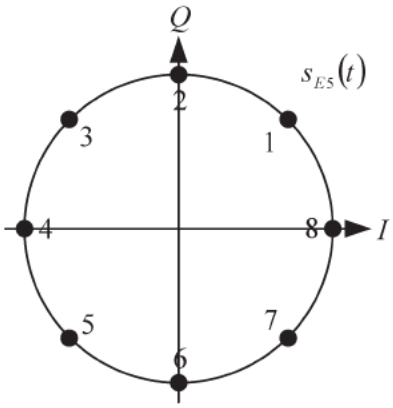

Figure 2.7: 8-PSK Phase-State Diagram of E5 AltBOC Signal [20].

The relation of the 8 phase states to the 16 different possible states of [e_{E5a-I}; e_{E5b-I};e_{E5a-Q}; e_{E5b-Q}] depends also on time. Therefore, time is partitioned first in subcarrier intervals T_s and further sub-divided in 8 equal sub-periods. The index i_{T_s} of the actual sub-period is given by Eq. 2.18 and determines which relation between input quadruple and phase states has to be used.

$$i_{T_s} = \text{integer part}\left[\frac{8}{T_s}(t \text{ modulo } T_s)\right] \quad \text{with} \quad i_{T_s} \in \{0,1,2,3,4,5,6,7\} \tag{2.18}$$

The dependency of phase-states from input-quadruples and time is given in table 2.2. The table

is composed of 128 (8×16) different entries which means that a 8×16 LUT could be used to greatly simplify the hardware and computational burden of generating the E5 signal.

Table 2.2: Look-up Table for AltBOC Phase States [20].

		Input Quadruples															
eE5a-I		-1	-1	-1	-1	-1	-1	-1	-1	1	1	1	1	1	1	1	1
eE5b-I		-1	-1	-1	-1	1	1	1	1	-1	-1	-1	-1	1	1	1	1
eE5a-Q		-1	-1	1	1	-1	-1	1	1	-1	-1	1	1	-1	-1	1	1
eE5b-Q		-1	1	-1	1	-1	1	-1	1	-1	1	-1	1	-1	1	-1	1
$t' = t$ modulo $T_{s,E5}$		k according to $s_{E5}(t)=\exp(jk\pi/4)$															
i_{T_s}	t'																
0	$[0, T_{s,E5}/8[$	5	4	4	3	6	3	1	2	6	5	7	2	7	8	8	1
1	$[T_{s,E5}/8, 2\ T_{s,E5}/8[$	5	4	8	3	2	3	1	2	6	5	7	6	7	4	8	1
2	$[2\ T_{s,E5}/8, 3\ T_{s,E5}/8[$	1	4	8	7	2	3	1	2	6	5	7	6	3	4	8	5
3	$[3\ T_{s,E5}/8, 4\ T_{s,E5}/8[$	1	8	8	7	2	3	1	6	2	5	7	6	3	4	4	5
4	$[4\ T_{s,E5}/8, 5\ T_{s,E5}/8[$	1	8	8	7	2	7	5	6	2	1	3	6	3	4	4	5
5	$[5\ T_{s,E5}/8, 6\ T_{s,E5}/8[$	1	8	4	7	6	7	5	6	2	1	3	2	3	8	4	5
6	$[6\ T_{s,E5}/8, 7\ T_{s,E5}/8[$	5	8	4	3	6	7	5	6	2	1	3	2	7	8	4	1
7	$[7\ T_{s,E5}/8, T_{s,E5}[$	5	4	4	3	6	7	5	2	6	1	3	2	7	8	8	1

2.5 Autocorrelation Function and Power Spectral Density

When dealing with GNSS signals, two very important characteristics are the autocorrelation function and the power spectrum, since they determine the navigation performance of a signal [25].

2.5.1 Autocorrelation Function

The normalized ACF for the E5 AltBOC signal can be analytically calculated as [26]:

$$\begin{aligned} R_{AltBOC(15,10)}(\tau) = {} & \Lambda_{T_c/6}(\tau) - \frac{2}{3}\Lambda_{T_c/6}\left(|\tau| - \frac{T_c}{3}\right) + \frac{1}{3}\Lambda_{T_c/6}\left(|\tau| - \frac{2T_c}{3}\right) \\ & - \frac{1}{24}\Lambda_{T_c/12}\left(|\tau| - \frac{T_c}{12}\right) - \frac{1}{24}\Lambda_{T_c/12}\left(|\tau| - \frac{3T_c}{12}\right) \\ & + \frac{1}{24}\Lambda_{T_c/12}\left(|\tau| - \frac{5T_c}{12}\right) + \frac{1}{24}\Lambda_{T_c/12}\left(|\tau| - \frac{7T_c}{12}\right) \\ & - \frac{1}{24}\Lambda_{T_c/12}\left(|\tau| - \frac{9T_c}{12}\right) - \frac{1}{24}\Lambda_{T_c/12}\left(|\tau| - \frac{11T_c}{12}\right) \end{aligned} \tag{2.19}$$

where T_c is the chip duration $\left(\frac{1}{10*1.023*10^6}\right)$, τ is the delay and Λ is the triangle function defined as

$$\Lambda_L(t) = \begin{cases} 1 - \frac{|t|}{L}, & |t| < L \\ 0, & \text{otherwise} \end{cases} \tag{2.20}$$

Fig. 2.8 represents the autocorrelation function of the Galileo E5 AltBOC signal. It can be seen that the ACF of the AltBOC presents a narrow correlation peak. However, it also presents secondary peaks with considerable amplitude (roughly 70% of the power of the main peak). These secondary peaks can

become a problem because they can lead to false lock in the acquisition and tracking stages, resulting in wrong values of time delay (see, for instance [22]).

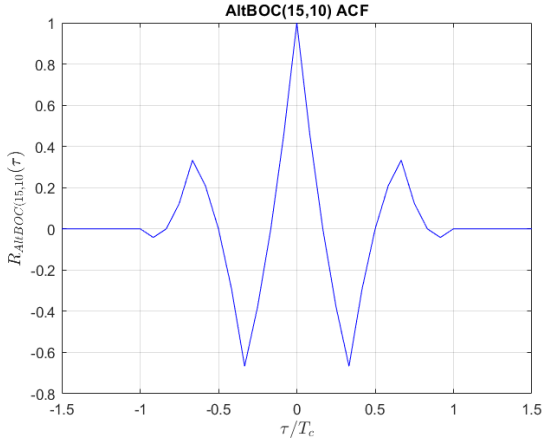

Figure 2.8: AltBOC(15,10) autocorrelation function.

2.5.2 Power Spectral Density

The normalized PSD represents the signal in the frequency domain. The AltBOC PSD can be obtained by computing the Fourier Transform of the ACF expression given by Eq. 2.19, yielding [26]:

$$G_{AltBOC(15,10)}(f) = \frac{T_c \cos^2(\pi f T_c)}{72 \cos\left(\frac{\pi f T_c}{3}\right)} \left[\frac{4\text{sinc}^2\left(\frac{fT_c}{6}\right)}{\cos\left(\frac{\pi f T_c}{3}\right)} - \text{sinc}^2\left(\frac{fT_c}{12}\right) \cos\left(\frac{\pi f T_c}{6}\right) \right] \tag{2.21}$$

The resulting graph for the normalised PSD is shown in Fig. 2.9.

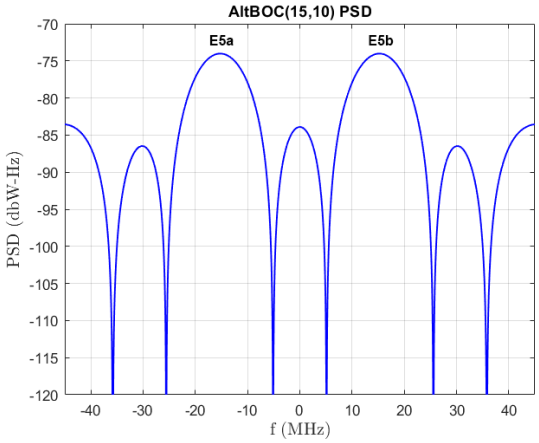

Figure 2.9: AltBOC(15,10) PSD.

Chapter 3

AltBOC Receiver Architectures

Due to the complexity of the AltBOC signal, the receiver designer can choose among three options for processing the signal [2, 22, 28]:

- Process entire E5 signal as a wideband 8-phase signal;
- Process both E5a and E5b, but separately;
- Process only the E5a or the E5b component;

Processing the entire E5 signal has the advantage of accessing all the signal power including use of the widest bandwidth GNSS signal with opportunities to minimize interference, multipath and reduce code tracking errors. The typical front-end filter bandwidth for a receiver that processes the whole signal is 51.15MHz [25]. However, there are some drawbacks as well. The use of a large fractional bandwidth, typically defined as the null-to-null bandwidth divided by the center frequency, implies the risk of significantly different Doppler effects over the signal bandwidth, potentially limiting integration times if significant satellite-to-receiver dynamics is expected. Dispersive effects due to the ionosphere [29] and the receiver front-end hardware may also present a problem. Furthermore, a high sampling rate is associated to the use of a wide bandwidth receiver which tends to increase the power consumption of the front-end and the digital processing blocks [2]. Initial synchronization (code and Doppler acquisition) of the entire wideband signal may also represent a problem due to its complexity. Thus, signal processing at the receiver is usually done using sideband processing because of the narrow correlation function that arises with wideband processing [2].

Coherently processing each E5a and E5b signal separately and combining the measurements in a single receiver channel is a compromise both in terms of benefits and implementation burden, while still making use of the entire signal. On the other hand, processing only the E5a or E5b signal reduces the implementation to that of a BPSK(10) signal but neglects more than half the signal power.

Taking these options into account, three different receiver architectures are proposed in [22]:

- **coherent dual band receiver**, based on the combined AltBOC correlation of E5a and E5b (entire signal). This receiver achieves the best performance, but is more complex than the others;

- **single band receiver**, based on a BPSK(10) demodulator for processing only the E5a or E5b component. This arrangement could be used in simple low-cost receivers, with high precision;
- **separate dual band receiver**, with non-coherent reception of E5a and E5b bands. It works with two separate BPSK(10) demodulators and offer slightly better performance than the previous one.

In the following sections these receiver architectures are presented in detail.

3.1 Coherent dual band receiver

The coherent dual band receiver is the one that can achieve the best performance. This receiver takes advantage of the coherence between the two E5 sidebands. The block diagram of this receiver architecture is presented in Fig. 3.1. Each correlation operation is implemented with a complex correlator block that uses the the two pilot codes (c_{E5a-Q} and c_{E5b-Q}) and the subcarrier with correct timing (sc_{E5-S}) and its delayed version ($sc^{off}_{E5-S} = sc_{E5-S}(t - T_s/4)$) to construct the signal local replica. A detailed explanation of each one of the blocks can be found in [22].

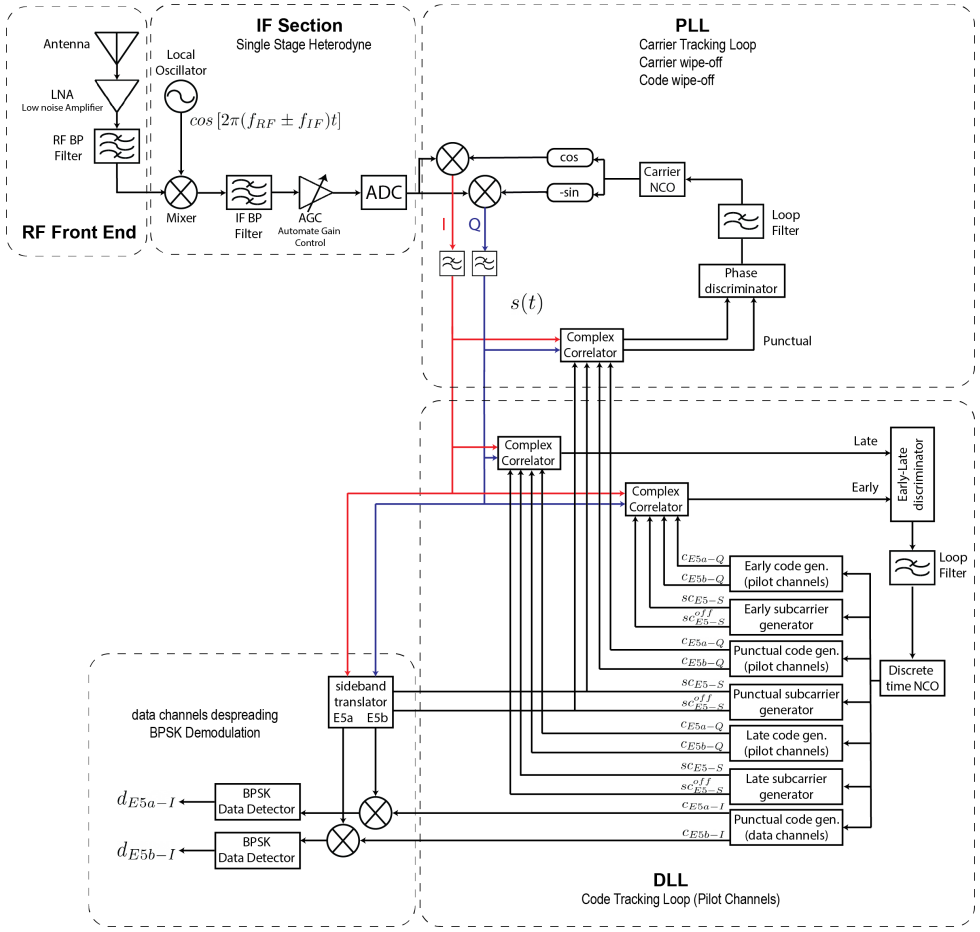

Figure 3.1: Coherent dual band receiver block diagram [22].

The early and late arms of the DLL perform a complex correlation between the incoming baseband signal and the pilot signal replica generated in the receiver.

Assuming correct synchronization of the receiver (PLL and DLL correctly locked) and neglecting the noise, the distortions and other propagation effects, the incoming baseband signal can be given by Eq. 2.14.

However, it was seen in [30] that for a front-end filter with bandwidth $B_{RF} \leq 92.07$MHz, the product subcarrier is eliminated. Given that the typical bandwidth is $B_{RF} = 51.15$MHz, the signal in Eq. 2.14 can be well approximated by:

$$\begin{aligned} s_{E5}(t) \approx & \frac{1}{2\sqrt{2}} \left(e_{E5a-I} + je_{E5a-Q}\right) \left[sc_{E5-S}(t) - jsc_{E5-S}(t - T_s/4)\right] \\ & + \frac{1}{2\sqrt{2}} \left(e_{E5b-I} + je_{E5b-Q}\right) \left[sc_{E5-S}(t) + jsc_{E5-S}(t - T_s/4)\right] \end{aligned} \tag{3.1}$$

The pilot signal replica generated in the receiver is described as

$$\begin{aligned} s_{E5p}(t) = & \frac{1}{2\sqrt{2}} je_{E5a-Q} \left[sc_{E5-S}(t) - jsc_{E5-S}(t - T_s/4)\right] \\ & + \frac{1}{2\sqrt{2}} je_{E5b-Q} \left[sc_{E5-S}(t) + jsc_{E5-S}(t - T_s/4)\right] \end{aligned} \tag{3.2}$$

Define now the cross-correlation function (CCF) operator as

$$R_{xy}(\tau) = < x(t)y^*(t-\tau) > = \frac{1}{T}\int_0^T x(t)y^*(t-\tau)dt \tag{3.3}$$

with T denoting the correlation interval. The output of the complex correlation computed in the DLL is, mathematically defined as

$$R_{ss_p}(\tau) = \frac{1}{T}\int_0^T s_{E5}(t)s^*_{E5p}(t-\tau)dt \tag{3.4}$$

where $T >> T_c$.

The quantities $e_{E5a-I}(t)$, $e_{E5a-Q}(t)$, $e_{E5a-Q}(t)$ and $e_{E5a-Q}(t)$ are independent code sequences. That is, $E\{e_{E5a-I}(t)e_{E5a-Q}(t)\} = 0$, $E\{e_{E5a-I}(t)e_{E5b-I}(t)\} = 0$, etc. Furthermore, $E\{|e_{E5a-I}(t)|^2\} = 1$, $E\{|e_{E5a-Q}(t)|^2\} = 1$, etc. Thus, Eq. 3.4 can be written as

$$\begin{aligned} R_{ss_p}(\tau) = & \frac{1}{4T_c}\int_{|\tau|}^{T_c} sc_{E5-S}(t)sc_{E5-S}(t-\tau)dt \\ & + \frac{1}{4T_c}\int_{|\tau|}^{T_c} sc_{E5-S}(t - T_s/4)sc_{E5-S}(t - T_s/4 - \tau)dt \end{aligned} \tag{3.5}$$

A method to compute this CCF that takes advantage of the fact that the subcarriers are a sum of rectangle functions is described in [26]. First, consider the CCF as the sum of partial CCFs, as follows

$$R_{ss_p}(\tau) = \sum_{j=1}^{2} R_j(\tau) \tag{3.6}$$

where

$$R_1(\tau) = \frac{1}{4T_c}\int_{|\tau|}^{T_c} sc_{E5-S}(t)sc_{E5-S}(t-\tau)dt \tag{3.7}$$

$$R_2(\tau) = \frac{1}{4T_c}\int_{|\tau|}^{T_c} sc_{E5-S}(t-T_s/4)sc_{E5-S}(t-T_s/4-\tau)dt \tag{3.8}$$

Taking Eq. 2.16 into account, the subcarrier can be written as a sum of rectangle functions leading to

$$R_1(\tau) = \frac{1}{4T_c}\sum_{i=1}^{12}\sum_{k=1}^{12} AS_{|i|_8}AS_{|k|_8}\int_{|\tau|}^{T_c}\Pi_{T_s}(t-iT_s/8)\Pi_{T_s}(t-kT_s/8-|\tau|)dt \tag{3.9}$$

It is shown that in the interval $lT_c/12 \leq |\tau| \leq (l+1)T_c/12$, $l = 0, ..., 11$, the integrals in the previous expression are given by

$$\int_{|\tau|}^{T_c}\Pi_{T_s}(t-iT_s/8)\Pi_{T_s}(t-kT_s/8-|\tau|)dt = \begin{cases}(l+1)T_s/8-|\tau|, & i=l+1,...,12,\ k=i-l\\ |\tau|-lT_s/8, & i=l+2,...,12,\ k=i-l-1\\ 0, & \text{otherwise}\end{cases} \tag{3.10}$$

Using this result, we obtain for the partial CCFs $R_j(\tau)$ in the interval $lT_c/12 \leq |\tau| \leq (l+1)T_c/12$, with $l = 0, ..., 10$:

$$\begin{bmatrix}R_1(\tau)\\ R_2(\tau)\end{bmatrix} = \left(\frac{l+1}{12}-\frac{|\tau|}{T_c}\right)\sum_{i=l+1}^{12}\begin{bmatrix}AS_{|i|_8}AS_{|i-l|_8}\\ AS_{|i-2|_8}AS_{|i-2-l|_8}\end{bmatrix} + \left(\frac{|\tau|}{T_c}-\frac{l}{12}\right)\sum_{i=l+2}^{12}\begin{bmatrix}AS_{|i|_8}AS_{|i-l-1|_8}\\ AS_{|i-2|_8}AS_{|i-3-l|_8}\end{bmatrix} \tag{3.11}$$

For $11T_c/12 \leq |\tau| \leq T_c$ we have

$$\begin{bmatrix}R_1(\tau)\\ R_2(\tau)\end{bmatrix} = \left(1-\frac{|\tau|}{T_c}\right)\sum_{i=l+1}^{12}\begin{bmatrix}AS_{|1|_8}AS_{|12|_8}\\ AS_{|-2|_8}AS_{|10|_8}\end{bmatrix} \tag{3.12}$$

Equations 3.11, 3.12 show that the CCF is picewise linear. Thus, can be expressed as

$$R_{ss_p}(\tau) = \alpha_l + \beta_l\frac{|\tau|}{T_c},\ \ l = 0, ..., 11 \tag{3.13}$$

with the parameters α_l and β_l indicated in table 3.1.

Table 3.1: Parameters α_l and β_l for the AltBOC(15,10) pilot ACF.

l	0	1	2	3	4	5	6	7	8	9	10	11
α_l	$\frac{1189}{2786}$	$\frac{535}{967}$	$\frac{569}{1257}$	$-\frac{51}{985}$	$-\frac{2123}{2955}$	$-\frac{620}{587}$	$-\frac{1189}{1576}$	$\frac{34}{3363}$	$\frac{781}{1154}$	$\frac{1189}{1576}$	$\frac{552}{2195}$	$-\frac{1138}{3771}$
β_l	$-\frac{609}{338}$	$-\frac{2327}{701}$	$-\frac{1138}{419}$	$-\frac{2633}{3771}$	$\frac{4909}{3771}$	$\frac{1240}{587}$	$\frac{1189}{788}$	$\frac{357}{1801}$	$-\frac{1444}{1801}$	$-\frac{1138}{1257}$	$-\frac{1138}{3771}$	$\frac{1138}{3771}$

The CCF can also be described in terms of a sum of triangle functions. In each interval $lT_c/12 \leq |\tau| \leq (l+1)T_c/12$, the ACF is given by the sum of the triangles $B_m \Lambda_{T_c/6}(|\tau| - mT_c/3)$, $m = 0, 1, 2$ and $C_n \Lambda_{T_c/12}(|\tau| - nT_c/6 - T_c/12)$, $n = 0, ..., 5$ with the weights B_m and C_n computed from Eq. 3.13. The result is

$$R_{ss_p}(\tau) = \sum_{m=0}^{2} B_m \Lambda_{T_c/6}\left(|\tau| - \frac{mT_c}{3}\right) + \sum_{n=0}^{5} C_n \Lambda_{T_c/12}\left(|\tau| - \frac{(2n+1)T_c}{12}\right) \tag{3.14}$$

with

$$B_m = \frac{1393}{3264}\begin{bmatrix} 1 & -\frac{2}{3} & \frac{1}{3} \end{bmatrix} \tag{3.15}$$

$$C_n = \begin{bmatrix} \frac{235}{3716} & -\frac{265}{3152} & -\frac{180}{5329} & \frac{228}{4175} & \frac{89}{20627} & -\frac{276}{10975} \end{bmatrix} \tag{3.16}$$

Notice how, despite both signals being complex, the correlation result in Eq. 3.14 is real. A hardware implementation model for the complex correlator block diagram is described in [22] and presented in Fig. 3.2 where all the correlation components were expanded and simplified. If the signal is undistorted and correctly tracked by the PLL and the DLL, the quadrature component, defined as c_Q in Fig. 3.2, is equal to zero. This component can be used, for instance, to detect tracking errors such as the presence of ionospheric error.

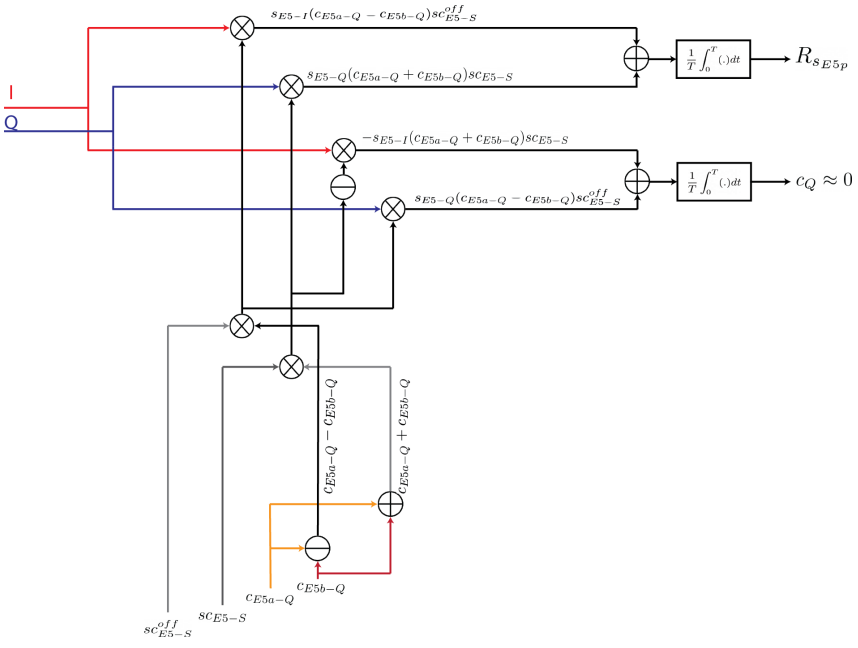

Figure 3.2: Complex Correlator block diagram [22].

Fig. 3.3 displays the ACF function for the AltBOC(15,10) pilot signal (Eq. 3.14) and the ACF for the complete AltBOC(15,10) signal (Eq. 2.19) for comparison. It can be seen that the pilot signal ACF is less sharper than the complete signal ACF (leading to worse performance). This has to do with the fact that the product subcarrier was filtered out. Furthermore, it can also be seen that more than half the power is being neglected (only 42% is used). Once more, this is a result of filtering the product subcarrier, that

recall, was approximately 15% of the signal power.

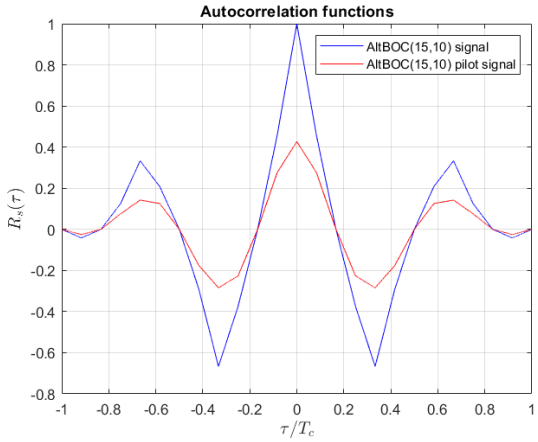

Figure 3.3: AltBOC(15,10) pilot signal autocorrelation function.

The PSD can be found by computing the fourier transform of Eq. 3.14 yielding

$$G_{ss_p}(f) = \frac{B_0 T_c}{6}\text{sinc}^2\left(fT_c/6\right) + \sum_{m=1}^{2}\frac{B_m T_c}{3}\text{sinc}^2\left(fT_c/6\right)\cos\left(2\pi f\frac{mT_c}{3}\right) + \sum_{n=0}^{5}\frac{C_n T_c}{6}\text{sinc}^2\left(fT_c/12\right)\cos\left(2\pi f\frac{(2n+1)T_c}{12}\right) \tag{3.17}$$

3.2 Single band receiver

The single band receiver architecture is the simplest receiver model. It works using only one side-band (for example E5a) that is translated from its center frequency to the baseband, process known as Side-band Translation (SBT) [28]. Thus, the demodulation of the signal is performed tracking the center frequency of the sideband (1176.45MHz, for E5a band and 1207.14MHz, for E5b band) as shown in Fig. 3.4. The received signal is down-converted and then low-pass filtered. The typical front-end bandwidth for the E5a or E5b signal is 20.46MHz [25].

A block diagram for this type of receiver is presented in Fig. 3.5.

At the output of the PLL in Fig. 3.5 the signal is split into its in-phase and quadrature components. Assuming correct synchronization of the receiver (PLL and DLL correctly locked) and neglecting the noise, the distortions and other propagation effects, the unity normalized components can be given by

$$s_{E5a-I}(t) = e_{E5a-I}(t) \tag{3.18}$$

$$s_{E5a-Q}(t) = e_{E5a-Q}(t) \tag{3.19}$$

These signals are obtained by filtering only a sub-band of the AltBOC signal as depicted in Fig. 3.4.

The quadrature component is then used in the DLL to track the pilot signal. Tracking only the pilot signal allows for larger correlation times. If it was necessary to track also the data channels, their data

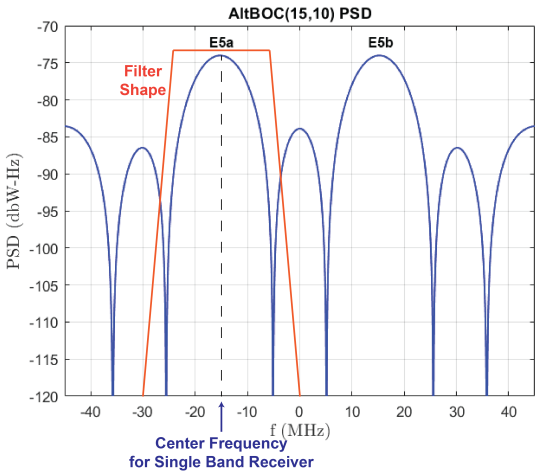

Figure 3.4: Signal bandwidth selection for a single band receiver using sub-band E5a [22].

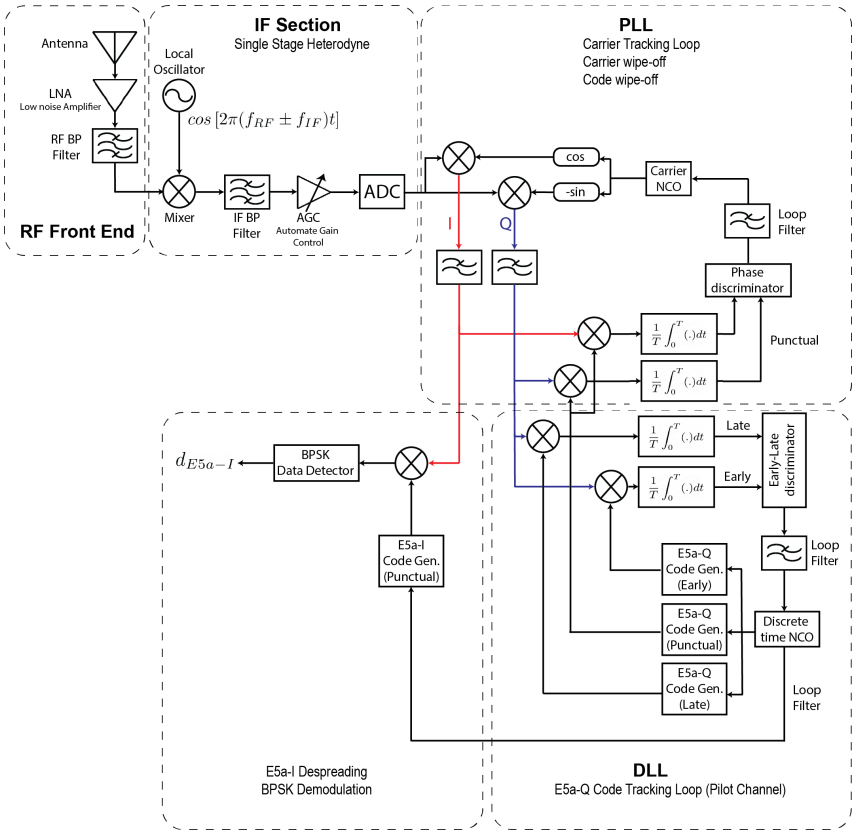

Figure 3.5: Signal band receiver block diagram [22].

bits would have to be wiped off [22].

The CCF between the quadrature component of the incoming signal and the pilot signal replica can be computed by

$$
\begin{aligned}
R_{ss_p}(\tau) &= \frac{1}{T}\int_0^T s_{E5a-Q}(t)s_p(t-\tau)dt \\
&= \frac{1}{T}\int_0^T s_{E5a-Q}(t)s_{E5a-Q}(t-\tau)dt \\
&= \frac{1}{T}\int_0^T e_{E5a-Q}(t)e_{E5a-Q}(t-\tau)dt
\end{aligned}
\tag{3.20}
$$

But, $e_{E5a-Q}(t)$ is an independent code sequence such that $E\{|e_{E5a-Q}(t)|^2\} = 1$. Thus

$$
R_{ss_p}(\tau) = \frac{1}{T_c}\int_{|\tau|}^{T_c} dt = 1 - \frac{|\tau|}{T_c} = \Lambda_{T_c}(\tau) \tag{3.21}
$$

Notice how the CCF obtained is equal to the one of the BPSK(10) signal. In [31] it is stated that using this SBT technique, there is a power sharing of 21%, i.e., only 21% of the whole E5 signal is used for tracking. Normalizing the power to the power of E5 signal we get

$$
R_{ss_p}(\tau) \approx 0.21\Lambda_{T_c}(\tau) \tag{3.22}
$$

The PSD can be found by taking the Fourier transform of Eq. 3.22 yielding

$$
G_{ss_p}(f) \approx 0.21T_c\mathrm{sinc}^2(fT_c) \tag{3.23}
$$

3.3 Separate dual band receiver

The separate dual band receiver allows the processing of both the sidebands individually. It is an extension of the single band receiver obtained by duplicating all the hardware after the radio-frequency front-end. The block diagram of this receiver architecture is presented in Fig. 3.6.

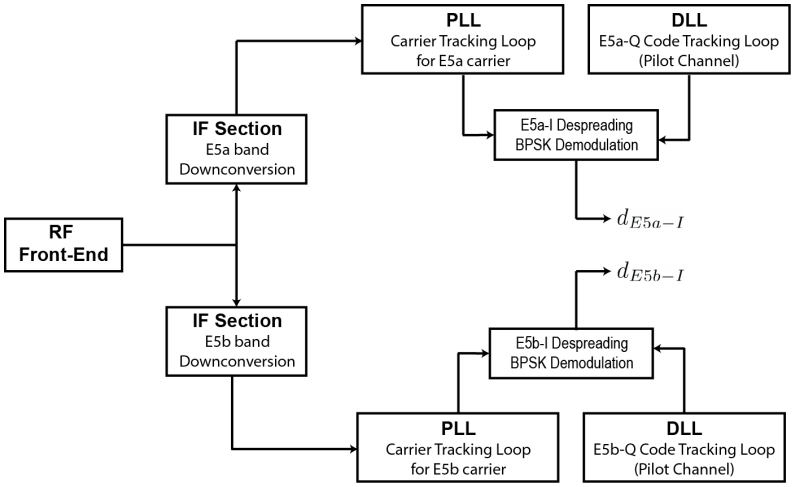

Figure 3.6: Separate dual band receiver block diagram [22].

The main advantage of this receiver is the possibility to correct the ionospheric error as two sub-bands with different subcarrier frequency are tracked simultaneously.

Chapter 4

Threat Models

Threat Models are based on modeling possible phenomena occurring at the satellite level in faulty conditions, inducing distortions on the GNSS Signals. The analysis of threat models was motivated by the occurrence of the SV19 event. In March 1993, a pseudorange bias between C/A and P(Y) code measurements of approximately 4 m was observed with SV19 during aircraft experiments. Follow on experiments noted that the differential position accuracy without SV19 were less than 50 cm [7]. After the SV19 discovery, considerable effort was made to explain and model this anomaly.

These investigations led to the identification of three primary correlation function deformations: asymmetry, dead zones and false peaks [16]. The underlying reason for this is that correlation function distortions can be mapped into DLL, and thus pseudoranges biases. In 1999 the 2OS model was proposed for the GPS L1 C/A, model which was capable of generating all the correlation distortions aforementioned [9]. This model consists in three classes of failure modes: digital (threat model A, TM-A), analog (threat model B, TM-B) and combination of both of them (threat model C, TM-C).This proposition has been adopted by ICAO for the GPS/GLONASS C/A code signal [10].

With the emergence of new and modernized GNSS signals, comes the need to define new TMs. The strategy presented in the literature has been to adapt the distortion models characterized by TM-A, TM-B and TM-C to new signals. For instance, threat models for Galileo E1C and Galileo E5a were defined in [12]. In [13], the same threat models were extended to account for BOC and CBOC modulations.

In this chapter we develop the threat models for the AltBOC modulation. As it was seen previously, there are three processing options when it comes to the AltBOC signal. When processing either one (single band receiver model) or both sub-bands independently (separate dual band receiver model), it was seen that the CCF used in tracking is equal to the one of the BPSK(10) signal one, given by Eq. 3.22. On the other hand, when processing the whole AltBOC signal (coherent dual band receiver), the CCF considered in tracking is the AltBOC(15,10) pilot correlation function given by Eq. 3.14. Therefore, in this chapter were developed threat models both for the BPSK(10) and AltBOC(15,10) signals in order to cover these three types of processing options. It is important to note that, in this work, the distortion models used for the single band and separate dual band receiver models were applied directly to the BPSK(10) modulation, which is a simplification. In reality, the distortions would happen at the satellite

payload, hence, in the AltBOC(15,10) modulation. This distorted signal would then be processed as a BPSK(10).

In section 4.1 the correlation functions' expressions for the Threat Model A (TM-A) are computed. This threat model can be subdivided into two different models, TM-A1 and TM-A2, that are covered in section 4.1.1 and 4.1.2, respectively. Section 4.2 presents the expressions for the Threat Model B (TM-B). Finally, section 4.3 develops the threat model C (TM-C) that, once more, is subdivided into two models, TM-C1 and TM-C2, that are covered in section 4.3.1 and 4.3.2, respectively.

4.1 Threat Model A

Threat Model A consists of the normal code signal except that all the positive chips have a falling edge that leads or lags relative to the correct end-time for that chip. This threat model is associated with a failure in the navigation data unit (NDU), the digital partition of a GNSS satellite [10].

4.1.1 Threat Model TM-A1

This threat model corresponds a lead/lag (Δ) on every falling transitions after modulation by the code signal.

In this section will be studied two different signals, BPSK(10) and AltBOC(15,10). As stated previously, the BPSK(10) signal formulation can be employed when processing one or both sub-bands using either a single band or separate dual band receiver, respectively. On the other hand, when processing the whole E5 signal (coherent dual band receiver), we need to consider the AltBOC(15,10) signal.

4.1.1.1 BPSK(10) signal

Typical waveforms for TM-A1 with BPSK(10) signals are represented in Fig. 4.1.

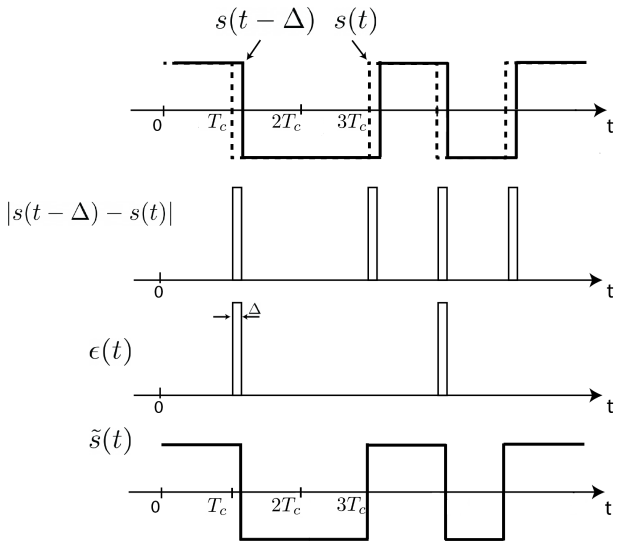

Figure 4.1: Typical waveform for TM-A1 with BPSK(10) signal and $|\Delta| < T_c/2$.

Let $s(t)$ be the undistorted BPSK(10) signal. The distorted signal can be formulated as [13]

$$\tilde{s}(t) = s(t) + \epsilon(t) \tag{4.1}$$

where the error signal, $\epsilon(t)$ is

$$\epsilon(t) = \frac{1}{2}[s\,(t-\Delta) - s\,(t)][1 + \mathrm{sign}\{s\,(t-\Delta) - s\,(t)\}] \tag{4.2}$$

where the function $\mathrm{sign}\{x\}$ is given by Eq. 2.3 .

There are two sub-bands to be considered, E5a and E5b, with similar properties. Both of them yield the same correlation functions. Therefore, for simplicity, we will only consider the sub-band E5a. The receiver's locally generated signal, $s_p(t)$, is, in this case, described by Eq. 3.19. The receiver's locally generated signal only contains the pilot signal in order to avoid data bit transitions, allowing for larger correlation times.

Multiplying the error model in Eq. 4.2 by the delayed version of the pilot signal yields

$$\begin{aligned}\epsilon(t)s_p(t-\tau) &= \frac{1}{2}[s\,(t-\Delta) - s\,(t)][1 + \mathrm{sign}\{s\,(t-\Delta) - s\,(t)\}]s_p(t-\tau) \\ &= \frac{1}{2}[s\,(t-\Delta) - s\,(t)]s_p(t-\tau) + \frac{1}{2}|s\,(t-\Delta) - s\,(t)\,|s_p(t-\tau)\end{aligned} \tag{4.3}$$

By time averaging Eq. 4.3 we obtain

$$R_{\epsilon s_p}(\tau) =< \epsilon(t)s_p(t-\tau) >= \frac{1}{2}[R_{ss_p}(\tau-\Delta) - R_{ss_p}(\tau)] + \frac{1}{2} < |s\,(t-\Delta) - s\,(t)\,|s_p(t-\tau) > \tag{4.4}$$

with $R_{ss_p}(\tau)$ equal to the CCF given by Eq. 3.22.

Notice that Eq. 4.4 is well defined apart from the last term that can be further simplified.

$$\begin{aligned}< |s\,(t-\Delta) - s\,(t)\,|s_p(t-\tau) > =< [s\,(t-\Delta) - s\,(t)]s_p(t-\tau) \times \mathrm{prob}\{s\,(t-\Delta) - s\,(t) > 0\} \\ - [s\,(t-\Delta) - s\,(t)]s_p(t-\tau) \times \mathrm{prob}\{s\,(t-\Delta) - s\,(t) < 0\} >\end{aligned} \tag{4.5}$$

However, for practical codes where every symbol has a similar probability of occurrence, it can be seen that $\mathrm{prob}\{s\,(t-\Delta) - s\,(t) > 0\} \approx \mathrm{prob}\{s\,(t-\Delta) - s\,(t) < 0\}$ which leads to

$$< |s\,(t-\Delta) - s\,(t)\,|s_p(t-\tau) > \approx 0 \tag{4.6}$$

Thus, Eq. 4.4 can be simplified to $R_{\epsilon s_p}(\tau) = \frac{1}{2}[R_{ss_p}(\tau-\Delta) - R_{ss_p}(\tau)]$ and the crosscorrelation of $\tilde{s}(t)$ and $s_p(t)$ is

$$\begin{aligned}R_{\tilde{s}s_p}(\tau) &=< \tilde{s}(t)s_p(t-\tau) >=< [s(t) + \epsilon(t)]s_p(t-\tau)] > \\ &= R_{ss_p}(\tau) + R_{\epsilon s_p}(\tau) = \frac{1}{2}[R_{ss_p}(\tau) + R_{ss_p}(\tau-\Delta)]\end{aligned} \tag{4.7}$$

Consider now the effect of lowpass filtering the distorted signal $\tilde{s}(t)$. This is particularly useful as every GNSS receiver possesses a front-end filter, as shown in Fig. 3.5 and Fig. 3.6 for a single band and separate dual band receiver, respectively. It is proven in [13] that the crosscorrelation function between the filtered distorted signal and the local replica is given by the inverse Fourier transform of the cross-spectrum times the frequency response of the lowpass filter. Let $R_A(\tau)$ be the filtered crosscorrelation function, we have that

$$\begin{aligned} R_A(\tau) &= \mathcal{F}^{-1}\{G_{\tilde{s}s_p}(f)H(f)\} \\ &= \int_{-\infty}^{+\infty} G_{\tilde{s}s_p}(f)H(f)\exp(j2\pi f\tau)df \end{aligned} \tag{4.8}$$

where $G_{\tilde{s}s_p}$ is the cross-spectrum given by the Fourier transform of the crosscorrelation function in Eq. 4.7.

For an ideal rectangular filter of bandwidth B with unity gain and group delay τ_0, i.e.

$$H(f) = \prod_{2B}(f)\exp(-j2\pi f\tau_0) \tag{4.9}$$

Eq. 4.8 can be simplified to

$$R_A(\tau) = \int_{-B}^{+B} G_{\tilde{s}s_p}(f)\exp(j2\pi f(\tau-\tau_0))df \tag{4.10}$$

Doing $\tau' = \tau - \tau_0$ results

$$R_A(\tau') = \int_{-B}^{+B} G_{\tilde{s}s_p}(f)\exp(j2\pi f\tau')df \tag{4.11}$$

Even though this expression is an approximation due to the assumption of an ideal rectangular filter, it was proven in [13] to be a good approximation to the response of a 6th order Butterworth filter. This filter has special interest because it is often employed in GNSS receivers [3].

Doing the Fourier transform of Eq. 4.7

$$G_{\tilde{s}s_p}(f) = \mathcal{F}\{R_{\tilde{s}s_p}(\tau)\} = \frac{1}{2}G_{ss_p}(f)[1+\exp(-j2\pi f\Delta)] \tag{4.12}$$

Using Eq. 3.23 we obtain

$$G_{\tilde{s}s_p}(f) = 0.105T_c\mathrm{sinc}^2(fT_c)[1+\exp(-j2\pi f\Delta)] \tag{4.13}$$

Replacing this expression in Eq. 4.11 we get

$$R_A(\tau') = 0.105T_c\int_{-B}^{+B}\mathrm{sinc}^2(fT_c)\exp(j2\pi f\tau')df + 0.105T_c\int_{-B}^{+B}\mathrm{sinc}^2(fT_c)\exp(j2\pi f(\tau'-\Delta))df \tag{4.14}$$

Doing $fT_c = x$ and $\Delta/T_c = D$

$$R_A(\tau') = 0.105 \int_{-BT_c}^{+BT_c} \operatorname{sinc}^2(x) \cos\left(2\pi f \frac{\tau'}{T_c} x\right) dx + 0.105 \int_{-BT_c}^{+BT_c} \operatorname{sinc}^2(x) \cos\left[2\pi f \left(\frac{\tau'}{T_c} - D\right) x\right] dx \tag{4.15}$$

Fig. 4.2 shows the normalized CCF for TM-A1 with a BPSK(10) signal and different delays. In the figure only positive values of Δ are represented because the effects of negative values are simply to advancing the correlation function rather than delaying it.

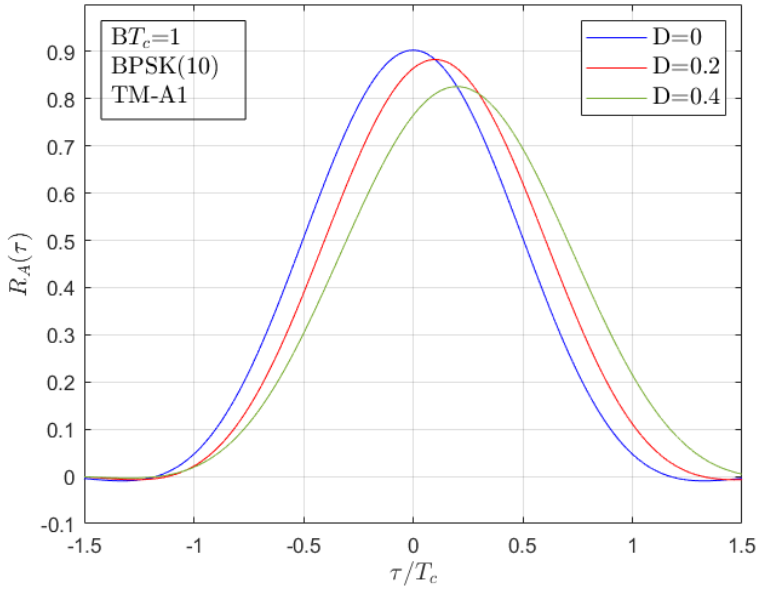

Figure 4.2: Normalized crosscorrelations $R_A(\tau)$ for BT_c = 1. TM-A1. Modulation: BPSK(10).

4.1.1.2 AltBOC(15,10) signal

Typical waveforms for TM-A1 with real/imaginary part of AltBOC(15,10) signals is represented in Fig. 4.3.

Note that the AltBOC(15,10) is a complex signal, hence, in Fig. 4.3 there is only represented what a typical waveform of the real/imaginary part would look like and not the whole signal.

The distorted signal is given by Eq. 4.1, where this time the error signal, $\epsilon(t)$ is

$$\epsilon(t) = \frac{1}{2}\Re\{s(t-\Delta) - s(t)\}[1 + \operatorname{sign}\{\Re\{s(t-\Delta) - s(t)\}\}] + \frac{j}{2}\Im\{s(t-\Delta) - s(t)\}[1 + \operatorname{sign}\{\Im\{s(t-\Delta) - s(t)\}\}] \tag{4.16}$$

or

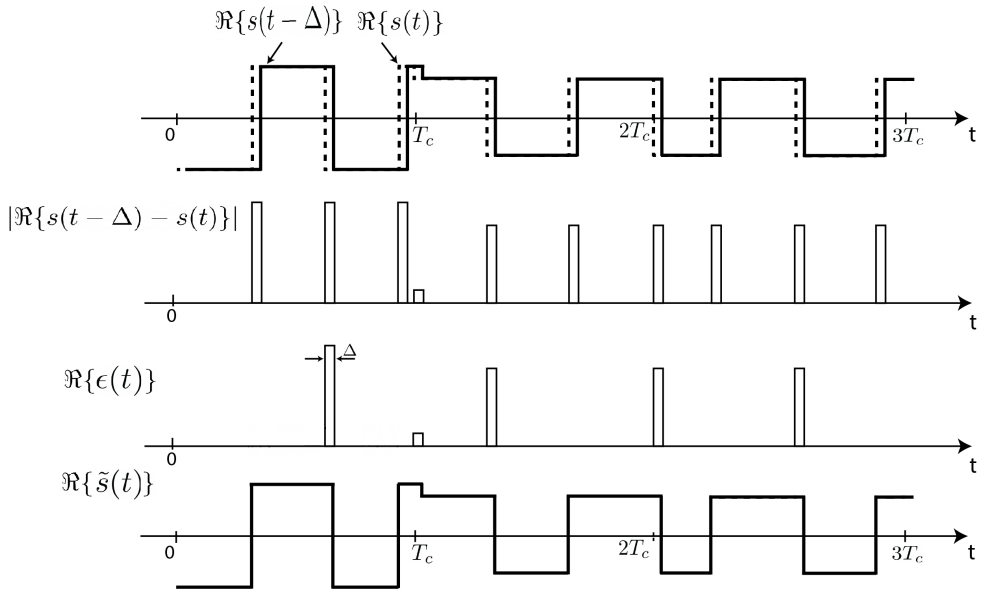

Figure 4.3: Typical waveform for TM-A1 with real/imaginary part of AltBOC(15,10) signal and $|\Delta| < T_c/12$.

$$\begin{aligned}\epsilon(t) &= \frac{1}{2}\Re\{s(t-\Delta)-s(t)\} + \frac{1}{2}|\Re\{s(t-\Delta)-s(t)\}| \\ &+ \frac{j}{2}\Im\{s(t-\Delta)-s(t)\} + \frac{j}{2}|\Im\{s(t-\Delta)-s(t)\}| \\ &= \frac{1}{2}[s(t-\Delta)-s(t)] + \frac{1}{2}|\Re\{s(t-\Delta)-s(t)\}| \\ &+ \frac{j}{2}|\Im\{s(t-\Delta)-s(t)\}|\end{aligned} \tag{4.17}$$

with $\Re\{x\}$ denoting the real part of x and $\Im\{x\}$ the imaginary part and the function $\mathrm{sign}\{x\}$ given by Eq. 2.3.

The error model in Eq. 4.16 is the extension of the model presented in Eq. 4.2 for the case of a complex signal.

For the case of a coherent dual band receiver, the incoming signal is complex correlated with a replica of the pilot signal. Multiplying the error model in Eq. 4.16 by the delayed version of the conjugate of the pilot signal we have that

$$\begin{aligned}\epsilon(t)\,s_p^*(t-\tau) =& \frac{1}{2}\Re\{s(t-\Delta)-s(t)\}s_p^*(t-\tau) + \frac{1}{2}|\Re\{s(t-\Delta)-s(t)\}|s_p^*(t-\tau) \\ &+ \frac{j}{2}\Im\{s(t-\Delta)-s(t)\}s_p^*(t-\tau) + \frac{j}{2}|\Im\{s(t-\Delta)-s(t)\}|s_p^*(t-\tau) \\ =& \frac{1}{2}[s(t-\Delta)-s(t)]s_p^*(t-\tau) + \frac{1}{2}|\Re\{s(t-\Delta)-s(t)\}|s_p^*(t-\tau) \\ & \frac{j}{2}|\Im\{s(t-\Delta)-s(t)\}|s_p^*(t-\tau)\end{aligned} \tag{4.18}$$

By time averaging Eq. 4.18 we obtain

$$R_{\epsilon s_p}(\tau) =< \epsilon\left(t\right) s_p^*\left(t-\tau\right) >=\frac{1}{2}[R_{ss_p}(\tau-\Delta)-R_{ss_p}(\tau)]+\frac{1}{2}< |\Re\{s\left(t-\Delta\right)-s\left(t\right)\}|s_p^*\left(t-\tau\right) > \\ \frac{j}{2}< |\Im\{s\left(t-\Delta\right)-s\left(t\right)\}|s_p^*\left(t-\tau\right) > \tag{4.19}$$

Note that Eq. 4.19 is well defined apart from the last two terms that can be further simplified.

$$< |\Re\{s\left(t-\Delta\right)-s\left(t\right)\}|s_p^*\left(t-\tau\right) > =< [\Re\{s\left(t-\Delta\right)-s\left(t\right)\}]s_p^*\left(t-\tau\right)\times \mathrm{prob}\{\Re\{s\left(t-\Delta\right)-s\left(t\right)\}>0\} \\ -[\Re\{s\left(t-\Delta\right)-s\left(t\right)\}]s_p^*\left(t-\tau\right)\times \mathrm{prob}\{\Re\{s\left(t-\Delta\right)-s\left(t\right)\}<0\} > \tag{4.20}$$

However, for practical codes where every symbol has a similar probability of occurrence, it can be seen that $\mathrm{prob}\{\Re\{s\left(t-\Delta\right)-s\left(t\right)\}>0\}\approx \mathrm{prob}\{\Re\{s\left(t-\Delta\right)-s\left(t\right)\}>0\}$ which leads to

$$< |\Re\{s\left(t-\Delta\right)-s\left(t\right)\}|s_p^*\left(t-\tau\right) >= 0 \tag{4.21}$$

Similarly, it can be obtained that

$$< |\Im\{s\left(t-\Delta\right)-s\left(t\right)\}|s_p^*\left(t-\tau\right) >= 0 \tag{4.22}$$

Thus, Eq. 4.19 can be simplified to $R_{\epsilon s_p}(\tau)=\frac{1}{2}[R_{ss_p}(\tau-\Delta)-R_{ss_p}(\tau)]$ and the crosscorrelation of $\tilde{s}(t)$ and $s_p(t)$ is

$$R_{\tilde{s}s_p}(\tau) =< \tilde{s}(t)s_p^*(t-\tau) >=< [s(t)+\epsilon(t)]s_p^*(t-\tau)] > \\ = R_{ss_p}(\tau)+R_{\epsilon s_p}(\tau)=\frac{1}{2}[R_{ss_p}(\tau)+R_{ss_p}(\tau-\Delta)] \tag{4.23}$$

This is the same expression obtained for the BPSK(10) signal apart from the fact that $R_{ss_p}(\tau)$ is now given by the AltBOC(15,10) pilot autocorrelation expression in Eq. 3.14.

Consider, once again, the effect of lowpass filtering the distorted signal $\tilde{s}(t)$, as shown in Fig. 3.1 for a typical coherent dual band receiver. For an ideal rectangular filter, it was seen previously that the filtered crosscorrelation function is given by Eq. 4.11 with the cross-spectrum defined in Eq. 4.12.

Using Eq. 3.17 in Eq. 4.12 yields

$$G_{\tilde{s}s_p}(f)=\frac{1}{2}\left[\frac{B_0T_c}{6}\mathrm{sinc}^2\left(fT_c/6\right)+\sum_{m=1}^{2}\frac{B_mT_c}{3}\mathrm{sinc}^2\left(fT_c/6\right)\cos\left(2\pi f\frac{mT_c}{3}\right)\right. \\ \left.+\sum_{n=0}^{5}\frac{C_nT_c}{6}\mathrm{sinc}^2\left(fT_c/12\right)\cos\left(2\pi f\frac{(2n+1)T_c}{12}\right)\right]\left[1+\exp(-j2\pi f\Delta)\right] \tag{4.24}$$

Replacing this expression in Eq. 4.11 we get

$$
\begin{aligned}
R_A(\tau') = & \frac{1}{2}\int_{-B}^{+B} \frac{B_0 T_c}{6}\mathrm{sinc}^2(fT_c/6)\exp(j2\pi f\tau')\,df + \frac{1}{2}\int_{-B}^{+B} \frac{B_0 T_c}{6}\mathrm{sinc}^2(fT_c/6)\exp(j2\pi f(\tau'-\Delta))\,df \\
& + \frac{1}{2}\int_{-B}^{+B} \sum_{m=1}^{2} \frac{B_m T_c}{3}\mathrm{sinc}^2(fT_c/6)\cos\left(2\pi f\frac{mT_c}{3}\right)\exp(j2\pi f\tau')\,df \\
& + \frac{1}{2}\int_{-B}^{+B} \sum_{m=1}^{2} \frac{B_m T_c}{3}\mathrm{sinc}^2(fT_c/6)\cos\left(2\pi f\frac{mT_c}{3}\right)\exp(j2\pi f(\tau'-\Delta))\,df \\
& + \frac{1}{2}\int_{-B}^{+B} \sum_{n=0}^{5} \frac{C_n T_c}{6}\mathrm{sinc}^2(fT_c/12)\cos\left(2\pi f\frac{(2n+1)T_c}{12}\right)\exp(j2\pi f\tau')\,df \\
& + \frac{1}{2}\int_{-B}^{+B} \sum_{n=0}^{5} \frac{C_n T_c}{6}\mathrm{sinc}^2(fT_c/12)\cos\left(2\pi f\frac{(2n+1)T_c}{12}\right)\exp(j2\pi f(\tau'-\Delta))\,df
\end{aligned}
\tag{4.25}
$$

Doing $fT_c = x$ and $\Delta/T_c = D$

$$
\begin{aligned}
R_A(\tau') = & \frac{B_0}{12}\int_{-BT_c}^{+BT_c} \mathrm{sinc}^2\left(\frac{x}{6}\right)\cos\left(2\pi\frac{\tau'}{T_c}x\right)dx + \frac{B_0}{12}\int_{-BT_c}^{+BT_c} \mathrm{sinc}^2\left(\frac{x}{6}\right)\cos\left(2\pi\left(\frac{\tau'}{T_c}-D\right)x\right)dx \\
& + \sum_{m=1}^{2}\frac{B_m}{6}\int_{-BT_c}^{+BT_c} \mathrm{sinc}^2\left(\frac{x}{6}\right)\cos\left(2\pi\frac{mx}{3}\right)\cos\left(2\pi\frac{\tau'}{T_c}x\right)dx \\
& + \sum_{m=1}^{2}\frac{B_m}{6}\int_{-BT_c}^{+BT_c} \mathrm{sinc}^2\left(\frac{x}{6}\right)\cos\left(2\pi\frac{mx}{3}\right)\cos\left(2\pi\left(\frac{\tau'}{T_c}-D\right)x\right)dx \\
& + \sum_{n=0}^{5}\frac{C_n}{12}\int_{-BT_c}^{+BT_c} \mathrm{sinc}^2\left(\frac{x}{12}\right)\cos\left(2\pi\frac{(2n+1)x}{12}\right)\cos\left(2\pi\frac{\tau'}{T_c}x\right)dx \\
& + \sum_{n=0}^{5}\frac{C_n}{12}\int_{-BT_c}^{+BT_c} \mathrm{sinc}^2\left(\frac{x}{12}\right)\cos\left(2\pi\frac{(2n+1)x}{12}\right)\cos\left(2\pi\left(\frac{\tau'}{T_c}-D\right)x\right)dx
\end{aligned}
\tag{4.26}
$$

Eq. 4.26 represents the crosscorrelation function between a TM-A1 distorted AltBOC(15,10) signal with its pilot signal.

However, the mathematical error model presented in Eq. 4.16 is only coherent with the physical model of a lead/lag on every falling transition for $|\Delta| < T_c/12$ which was seen to not be sufficient to test the SQM techniques. Hence, there was the need to develop a model that would be suitable for larger leads/lags. Therefore, herein is proposed an algorithm, developed in Appendix B, that consists in adding new terms to extend the model up to $|\Delta| < T_c/6$.

Employing this new model, we have that the crosscorrelation for $|\Delta| < T_c/6$ can be rewritten as (Eq. B.8)

$$
\begin{aligned}
R_A(\tau') = & \frac{B_0}{12}\int_{-BT_c}^{+BT_c} \operatorname{sinc}^2\left(\frac{x}{6}\right)\cos\left(2\pi\frac{\tau'}{T_c}x\right)dx + \frac{B_0}{12}\int_{-BT_c}^{+BT_c} \operatorname{sinc}^2\left(\frac{x}{6}\right)\cos\left(2\pi\left(\frac{\tau'}{T_c}-D\right)x\right)dx \\
& + \sum_{m=1}^{2}\frac{B_m}{6}\int_{-BT_c}^{+BT_c} \operatorname{sinc}^2\left(\frac{x}{6}\right)\cos\left(2\pi\frac{mx}{3}\right)\cos\left(2\pi\frac{\tau'}{T_c}x\right)dx \\
& + \sum_{m=1}^{2}\frac{B_m}{6}\int_{-BT_c}^{+BT_c} \operatorname{sinc}^2\left(\frac{x}{6}\right)\cos\left(2\pi\frac{mx}{3}\right)\cos\left(2\pi\left(\frac{\tau'}{T_c}-D\right)x\right)dx \\
& + \sum_{n=0}^{5}\frac{C_n}{12}\int_{-BT_c}^{+BT_c} \operatorname{sinc}^2\left(\frac{x}{12}\right)\cos\left(2\pi\frac{(2n+1)x}{12}\right)\cos\left(2\pi\frac{\tau'}{T_c}x\right)dx \\
& + \sum_{n=0}^{5}\frac{C_n}{12}\int_{-BT_c}^{+BT_c} \operatorname{sinc}^2\left(\frac{x}{12}\right)\cos\left(2\pi\frac{(2n+1)x}{12}\right)\cos\left(2\pi\left(\frac{\tau'}{T_c}-D\right)x\right)df \\
& + \sum_{n=-11}^{13}\int_{-BT_c}^{+BT_c}\gamma_n\left[\frac{1}{24}+\frac{D_1}{2}\right]^2 \operatorname{sinc}^2\left(x\left[\frac{1}{24}+\frac{D_1}{2}\right]\right)\cos\left(2\pi\left[\frac{\tau'}{T_c}-\frac{1}{12}\left(n-\frac{1}{2}+6D_1\right)\right]x\right)dx \\
& - \sum_{n=-11}^{13}\int_{-BT_c}^{+BT_c}\gamma_n\left[\frac{1}{24}-\frac{D_1}{2}\right]^2 \operatorname{sinc}^2\left(x\left[\frac{1}{24}-\frac{D_1}{2}\right]\right)\cos\left(2\pi\left[\frac{\tau'}{T_c}-\frac{1}{12}\left(n-\frac{1}{2}+6D_1\right)\right]x\right)dx
\end{aligned}
\tag{4.27}
$$

where

$$
D_1 = \begin{cases} D - 1/12, & 1/12 < D \leq 1/6 \\ 0, & \text{otherwise} \end{cases}
\tag{4.28}
$$

The coefficients γ_n are given in table B.1. Notice that for $D < 1/12$, Eq. 4.27 is equal to Eq. 4.26.

Fig. 4.4 shows the normalized crosscorrelation function for TM-A1 with AltBOC(15,10) signal and different delays.

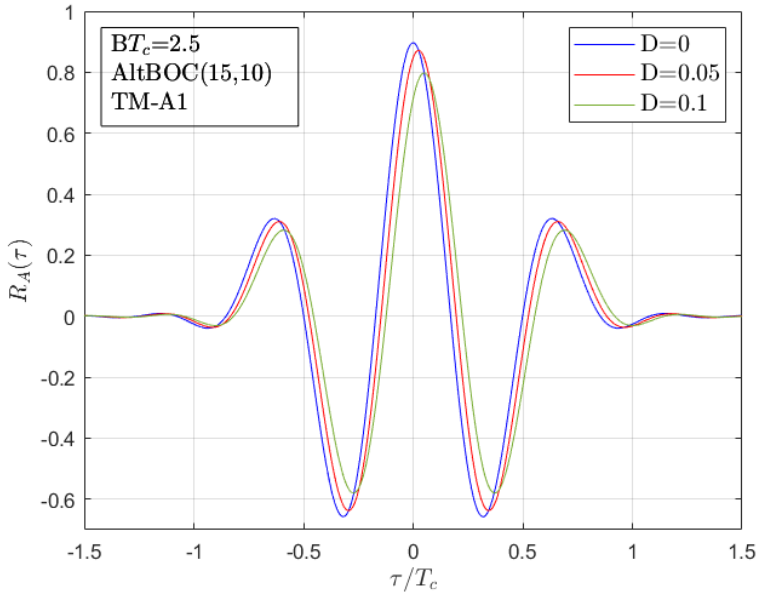

Figure 4.4: Normalized crosscorrelations $R_A(\tau)$ for BT_c = 2.5. TM-A1. Modulation: AltBOC(15,10).

4.1.2 Threat Model TM-A2

This threat model corresponds to a lead/lag (Δ_s) on every falling transition in the subcarriers before modulation by the code signal. It corresponds to the digital distortion 2 described in [3].

In this subsection we will only consider the AltBOC(15,10) signal as it is the only one that possesses subcarriers.

4.1.2.1 AltBOC(15,10) signal

In the AltBOC(15,10) modulation there are 2 subcarriers, the single subcarrier , $sc_{E5-S}(t)$, and the product subcarrier, $sc_{E5-P}(t)$. For the threat model TM-A2, we will only consider an anomaly on the single subcarrier since most of the energy of the product subcarrier is filtered by the receivers' front-end. Therefore, if by any chance, there was a distortion in the product subcarrier, that distortion would be filtered out. Hence, the subscript "s" on the variable Δ_s.

The waveform for TM-A2 of the single subcarrier is represented in Fig. 4.5. Two code periods are depicted to show the signal's dependence on time.

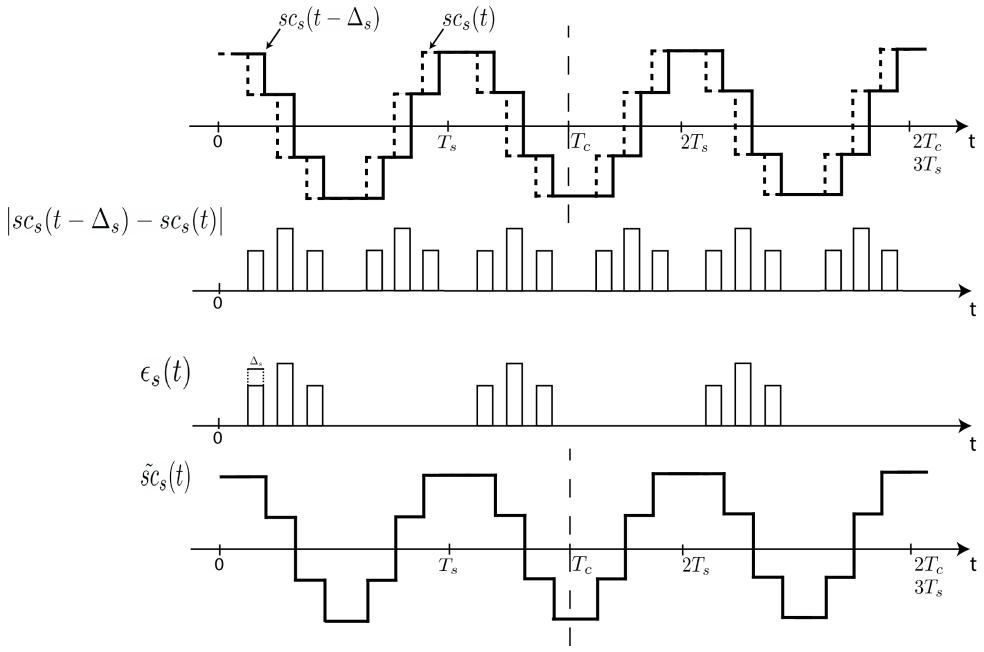

Figure 4.5: Typical waveforms for TM-A2 of the single subcarrier for $|\Delta_s| < T_c/12$.

The distorted single subcarrier can be given by

$$\tilde{sc}_{E5-S}(t) = sc_{E5-S}(t) + \epsilon_s(t) \tag{4.29}$$

with

$$\epsilon_s(t) = \frac{1}{2}\left[sc_{E5-S}(t-\Delta_s) - sc_{E5-S}(t)\right]\left[1 + \text{sign}\{sc_{E5-S}(t-\Delta_s) - sc_{E5-S}(t)\}\right] \tag{4.30}$$

Due to the lack of information about the payload and for simplicity, it is assumed that if there was a

problem, both $sc_{E5-S}(t)$ and $sc_{E5-S}(t-T_s/4)$ would be affected similarly. This assumption relies on the premise that both these signals are generated dependently.

The distorted AltBOC(15,10) signal can, neglecting the product components, be defined as

$$\begin{aligned}\tilde{s}(t) \approx & \frac{1}{2\sqrt{2}}[e_{E5a-I}(t)+je_{E5a-Q}(t)][\tilde{sc}_{E5-S}(t)-j\tilde{sc}_{E5-S}(t-T_s/4)] \\ & +\frac{1}{2\sqrt{2}}[e_{E5b-I}(t)+je_{E5b-Q}(t)][\tilde{sc}_{E5-S}(t)+j\tilde{sc}_{E5-S}(t-T_s/4)] \\ = & \frac{1}{2\sqrt{2}}[e_{E5a-I}(t)+je_{E5a-Q}(t)][sc_{E5-S}(t)+\epsilon_s(t)-j(sc_{E5-S}(t-T_s/4)+\epsilon_s(t-T_s/4))] \\ & +\frac{1}{2\sqrt{2}}[e_{E5b-I}(t)+je_{E5b-Q}(t)][sc_{E5-S}(t)+\epsilon_s(t)+j(sc_{E5-S}(t-T_s/4)+\epsilon_s(t-T_s/4))\end{aligned} \tag{4.31}$$

Multiplying the incoming signal described in Eq. 4.31 by the conjugate of the delayed pilot signal we obtain

$$\begin{aligned}\tilde{s}(t)s_p^*(t-\tau) = & s(t)s_p^*(t-\tau)+\frac{1}{2\sqrt{2}}[e_{E5a-I}(t)+je_{E5a-Q}(t)][\epsilon_s(t)-j+\epsilon_s(t-T_s/4)]s_p^*(t-\tau) \\ & +\frac{1}{2\sqrt{2}}[e_{E5b-I}(t)+je_{E5b-Q}(t)][\epsilon_s(t)+j+\epsilon_s(t-T_s/4)]s_p^*(t-\tau)\end{aligned} \tag{4.32}$$

By time averaging

$$\begin{aligned}R_{\tilde{s}s_p}(\tau) = & <\tilde{s}(t)s_p^*(t-\tau)> \\ & = R_{ss_p}(\tau)+<\frac{1}{2\sqrt{2}}[e_{E5a-I}(t)+je_{E5a-Q}(t)][\epsilon_s(t)-j\epsilon_s(t-T_s/4)]s_p^*(t-\tau)> \\ & +<\frac{1}{2\sqrt{2}}[e_{E5b-I}(t)+je_{E5b-Q}(t)][\epsilon_s(t)+j\epsilon_s(t-T_s/4)]s_p^*(t-\tau)>\end{aligned} \tag{4.33}$$

There are two terms from Eq. 4.33 that are still not well defined. Knowing that all 4 codes are independent to each other and using Eq. 3.2 for the local replica, we can obtain

$$\begin{aligned}& <\frac{1}{2\sqrt{2}}[e_{E5a-I}(t)+je_{E5a-Q}(t)][\epsilon_s(t)-j\epsilon_s(t-T_s/4)]s_p^*(t-\tau)> \\ = & \frac{1}{8}<e_{E5a-Q}(t)e_{E5a-Q}(t-\tau)[\epsilon_s(t)-j\epsilon_s(t-T_s/4)][sc_{E5-S}(t-\tau)+jsc_{E5-S}(t-T_s/4-\tau)]> \\ = & \frac{1}{8}<e_{E5a-Q}(t)e_{E5a-Q}(t-\tau)[\epsilon_s(t)sc_{E5-S}(t-\tau)+\epsilon_s(t-T_s/4)sc_{E5-S}(t-T_s/4-\tau)]> \\ & +\frac{j}{8}<e_{E5a-Q}(t)e_{E5a-Q}(t-\tau)[\epsilon_s(t)sc_{E5-S}(t-T_s/4-\tau)-\epsilon_s(t-T_s/4)sc_{E5-S}(t-\tau)]> \\ \approx & \left[\frac{1}{8}<\epsilon_s(t)sc_{E5-S}(t-\tau)+\epsilon_s(t-T_s/4)sc_{E5-S}(t-T_s/4-\tau)>\right. \\ & \left.+\frac{j}{8}<\epsilon_s(t)sc_{E5-S}(t-T_s/4-\tau)-\epsilon_s(t-T_s/4)sc_{E5-S}(t-\tau)>\right]\Lambda_{T_c}(\tau)\end{aligned} \tag{4.34}$$

We can do the same analysis for the second term and obtain

$$
\begin{aligned}
&< \frac{1}{2\sqrt{2}}[e_{E5b-I}(t) + je_{E5b-Q}(t)][\epsilon_s(t) + j\epsilon_s(t - T_s/4)]s_p^*(t-\tau) > \\
\approx &\left[\frac{1}{8} < \epsilon_s(t)sc_{E5-S}(t-\tau) + \epsilon_s(t - T_s/4)sc_{E5-S}(t - T_s/4 - \tau) > \right. \\
&\left. + \frac{j}{8} < -\epsilon_s(t)sc_{E5-S}(t - T_s/4 - \tau) + \epsilon_s(t - T_s/4)sc_{E5-S}(t-\tau) > \right] \Lambda_{T_c}(\tau)
\end{aligned} \tag{4.35}
$$

Note how the real parts of Eq. 4.34 and Eq. 4.35 are equal to each other while the imaginary parts are symmetric, and therefore, will cancel out when summed. Thus, we only need to compute the real part. Considering, first, the term with dependency on the in phase subcarrier

$$
\begin{aligned}
&< \epsilon_s(t)sc_{E5-S}(t-\tau) > \\
=&< \frac{1}{2}\left[sc_{E5-S}\left(t - \Delta_s\right) - sc_{E5-S}\left(t\right)\right]\left[1 + \text{sign}\{sc_{E5-S}\left(t - \Delta_s\right) - sc_{E5-S}\left(t\right)\}\right] sc_{E5-S}\left(t-\tau\right) > \\
=&\frac{1}{2} < \left(sc_{E5-S}\left(t - \Delta_s\right) - sc_{E5-S}\left(t\right)\right) sc_{E5-S}\left(t-\tau\right) > \\
+&\frac{1}{2} < \left|sc_{E5-S}\left(t - \Delta_s\right) - sc_{E5-S}\left(t\right)\right| sc_{E5-S}\left(t-\tau\right) >
\end{aligned} \tag{4.36}
$$

Taking a closer look at the second term, we get

$$
\begin{aligned}
&< \left|sc_{E5-S}\left(t - \Delta_s\right) - sc_{E5-S}\left(t\right)\right| sc_{E5-S}\left(t-\tau\right) > \\
=&< \left[sc_{E5-S}\left(t - \Delta_s\right) - sc_{E5-S}\left(t\right)\right] sc_{E5-S}\left(t-\tau\right) \times \text{prob}\{sc_{E5-S}\left(t - \Delta_s\right) - sc_{E5-S}\left(t\right) > 0\} \\
&- \left[sc_{E5-S}\left(t - \Delta_s\right) - sc_{E5-S}\left(t\right)\right] sc_{E5-S}\left(t-\tau\right) \times \text{prob}\{sc_{E5-S}\left(t - \Delta_s\right) - sc_{E5-S}\left(t\right) < 0\} >
\end{aligned} \tag{4.37}
$$

Analysing Fig. 4.5 we come to the conclusion that the single subcarrier can have two distinct waveforms which are symmetric to each other. Particularly, in the second graph we can see that $sc_{E5-S}(t - \Delta_s) - sc_{E5-S}(t) = -(sc_{E5-S}(t - T_c - \Delta_s) - sc_{E5-S}(t - T_c))$ for $0 \leq t \leq T_c$. Thus, we can conclude that $\text{prob}\{sc_{E5-S}\left(t - \Delta_s\right) - sc_{E5-S}\left(t\right) > 0\} = \text{prob}\{sc_{E5-S}\left(t - \Delta_s\right) - sc_{E5-S}\left(t\right) < 0\}$ and therefore, Eq. 4.37 is equal to 0.

As for the first term of Eq. 4.36, we will consider an approximation. In [30], it is demonstrated that for a mild amount of filtering, the inphase and quadrature single subcarriers are well approximated by

$$
sc_{E5-S}(t) \approx \frac{4}{\pi}\cos(2\pi f_s t) \tag{4.38}
$$

$$
sc_{E5-S}(t - T_s/4) \approx \frac{4}{\pi}\sin(2\pi f_s t) \tag{4.39}
$$

Using these approximations in Eq. 4.36 we obtain

$$
\begin{aligned}
< \epsilon_s(t) sc_{E5-S}(t-\tau) > &\approx \frac{4}{\pi^2} < (\cos(2\pi f_s(t-\Delta_s)) - \cos(2\pi f_s t))\cos(2\pi f_s(t-\tau)) > \\
&= \frac{4}{\pi^2}[\cos(2\pi f_s(\tau-\Delta_s)) - \cos(2\pi f_s \tau)]
\end{aligned}
\tag{4.40}
$$

This analysis can also be conducted for the term with dependency on the quadrature subcarrier yielding

$$
\begin{aligned}
< \epsilon_s(t-T_s/4) sc_{E5-S}(t-T_s/4-\tau) > &\approx \frac{4}{\pi^2} < (\sin(2\pi f_s(t-\Delta_s)) - \sin(2\pi f_s t))\sin(2\pi f_s(t-\tau)) > \\
&= \frac{4}{\pi^2}[\cos(2\pi f_s(\tau-\Delta_s)) - \cos(2\pi f_s \tau)]
\end{aligned}
\tag{4.41}
$$

Substituting these results in Eq. 4.33 we obtain

$$
\begin{aligned}
R_{\tilde{s}s_p}(\tau) &\approx R_{ss_p}(\tau) + 2 * \frac{1}{8} < \epsilon_s(t) sc_{E5-S}(t-\tau) + \epsilon_s(t-T_s/4) sc_{E5-S}(t-T_s/4-\tau) > \Lambda_{T_c}(\tau) \\
&= R_{ss_p}(\tau) + \frac{2}{\pi^2}[\cos(2\pi f_s(\tau-\Delta_s)) - \cos(2\pi f_s \tau)]\Lambda_{T_c}(\tau)
\end{aligned}
\tag{4.42}
$$

As seen previously, for typical receivers, the incoming distorted signal will suffer some low-pass filtering in the receiver's front-end. The crosscorrelation after said filtering is given by Eq. 4.11 where there is a dependency on the cross-power spectrum, $G_{\tilde{s}s_p}(f)$. Thus, we need to compute it.

$$
G_{\tilde{s}s_p}(f) = \mathcal{F}\{R_{\tilde{s}s_p}(\tau)\} = G_{ss_p}(\tau) + \frac{2}{\pi^2}\mathcal{F}\{[\cos(2\pi f_s(\tau-\Delta_s)) - \cos(2\pi f_s \tau)]\Lambda_{T_c}(\tau)\} \tag{4.43}
$$

But

$$
\begin{aligned}
\mathcal{F}\{\cos(2\pi f_s \tau)\Lambda_{T_c}(\tau)\} &= \mathcal{F}\{\cos(2\pi f_s \tau)\} * \mathcal{F}\{\Lambda_{T_c}(\tau)\} \\
&= \frac{1}{2}\left[\delta(f-f_s) + \delta(f+f_s)\right] * T_c \mathrm{sinc}^2(fT_c) \\
&= \frac{T_c}{2}\left[\mathrm{sinc}^2[T_c(f-f_s)] + \mathrm{sinc}^2[T_c(f+f_s)]\right]
\end{aligned}
\tag{4.44}
$$

$$
\begin{aligned}
\mathcal{F}\{cos(2\pi f_s(\tau-\Delta_s))\Lambda_{T_c}(\tau)\} &= \mathcal{F}\{cos(2\pi f_s \tau - 2\pi f_s \Delta_s)\} * \mathcal{F}\{\Lambda_{T_c}(\tau)\} \\
&= \frac{1}{2}\left[\exp(-j2\pi f_s \Delta_s)\delta(f-f_s) + \exp(j2\pi f_s \Delta_s)\delta(f+f_s)\right] * T_c \mathrm{sinc}^2(fT_c) \\
&= \frac{T_c}{2}\left[\exp(-j2\pi f_s \Delta_s)\mathrm{sinc}^2[T_c(f-f_s)] + \exp(j2\pi f_s \Delta_s)\mathrm{sinc}^2[T_c(f+f_s)]\right]
\end{aligned}
\tag{4.45}
$$

yielding

$$G_{\tilde{s}s_p}(f) = G_{ss_p}(\tau) + \frac{T_c}{\pi^2}\left\{\text{sinc}^2(T_c(f-f_s))[\exp(-j2\pi f_s\Delta_s)-1] + \text{sinc}^2(T_c(f+f_s))[\exp(j2\pi f_s\Delta_s)-1]\right\} \tag{4.46}$$

Replacing this result in Eq. 4.11 we get

$$\begin{aligned} R_A(\tau') = &\int_{-B}^{+B} G_{ss_p}(f)\exp(j2\pi f\tau')df \\ &+ \frac{T_c}{\pi^2}\int_{-B}^{+B}\text{sinc}^2(T_c(f-f_s))[\exp(-j2\pi f_s\Delta_s)-1]\exp(j2\pi f\tau')df \\ &+ \frac{T_c}{\pi^2}\int_{-B}^{+B}\text{sinc}^2(T_c(f+f_s))[\exp(j2\pi f_s\Delta_s)-1]\exp(j2\pi f\tau')df \end{aligned} \tag{4.47}$$

Doing $fT_c = x$ and $\Delta/T_c = D$ and using Eq. 3.14

$$\begin{aligned} R_A(\tau') = &\frac{B_0}{6}\int_{-BT_c}^{+BT_c}\text{sinc}^2\left(\frac{x}{6}\right)\cos\left(2\pi\frac{\tau'}{T_c}x\right)dx \\ &+ \sum_{m=1}^{2}\frac{B_m}{3}\int_{-BT_c}^{+BT_c}\text{sinc}^2\left(\frac{x}{6}\right)\cos\left(2\pi\frac{mx}{3}\right)\cos\left(2\pi\frac{\tau'}{T_c}x\right)df \\ &+ \sum_{n=0}^{5}\frac{C_n}{6}\int_{-BT_c}^{+BT_c}\text{sinc}^2\left(\frac{x}{12}\right)\cos\left(2\pi\frac{(2n+1)x}{12}\right)\cos\left(2\pi\frac{\tau'}{T_c}x\right)df \\ &+ \frac{1}{\pi^2}\int_{-BT_c}^{+BT_c}\text{sinc}^2(x-k)\left[\cos[2\pi(x\frac{\tau}{T_c}-kD_s)]-\cos(2\pi\frac{\tau}{T_c}x)\right]df \\ &+ \frac{1}{\pi^2}\int_{-BT_c}^{+BT_c}\text{sinc}^2(x+k)\left[\cos[2\pi(x\frac{\tau}{T_c}+kD_s)]-\cos(2\pi\frac{\tau}{T_c}x)\right]df \end{aligned} \tag{4.48}$$

where $k = \frac{f_s}{f_c} = 1.5$.

Fig. 4.6 shows the normalized crosscorrelation function for TM-A2 with AltBOC(15,10) signal and different delays.

4.2 Threat Model B

Threat Model B introduces amplitude modulation and models degradations in the analog subsection of the GNSS satellite. More specifically, it consists of the output from a second order system when the code modulated baseband signal is the input. The TM-B assumes that the degraded satellite subsystem can be described as a linear system dominated by a pair of complex conjugate poles. These poles are located at $\sigma \pm j2\pi f_d$, where σ is the damping factor in Mnepers/second and f_d is the resonant frequency in MHz [16].

In [3] is shown that the transfer function of the second order low-pass filter can be given by

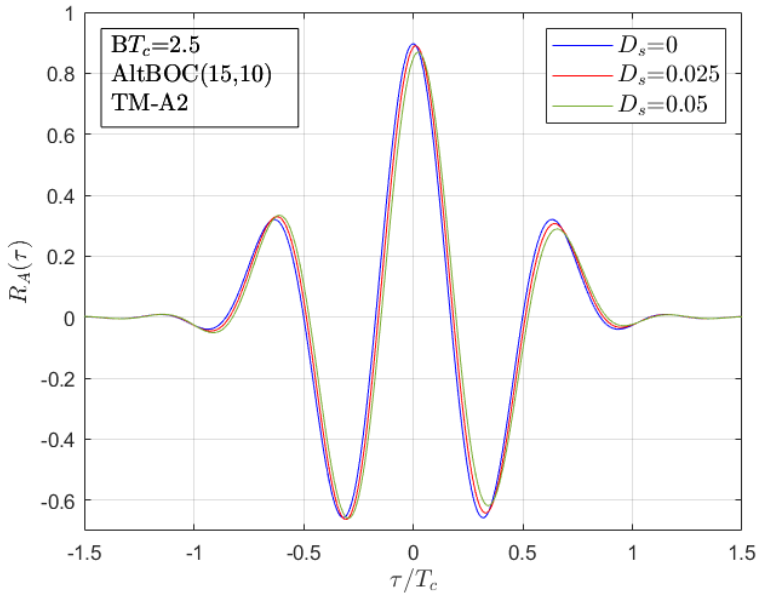

Figure 4.6: Normalized crosscorrelations $R_A(\tau)$ for BT_c = 2.5. TM-A2. Modulation: AltBOC(15,10).

$$\tilde{H}(\omega) = \frac{\omega_n^2}{\omega_n^2 - \omega^2 + j2\xi\omega_n\omega} \tag{4.49}$$

or doing $\Omega = \omega/\omega_n$

$$\tilde{H}(\Omega) = \frac{1}{1 - \Omega^2 + j2\xi\Omega} = \frac{\exp(-j\arctan\frac{2\xi\Omega}{1-\Omega^2})}{\sqrt{(1-\Omega^2)^2 + 4\xi^2\Omega^2}} \tag{4.50}$$

The natural frequency of the second order filter is given by

$$\omega_n = \sqrt{\sigma^2 + \omega_d^2} \tag{4.51}$$

and the normalized damping factor

$$\xi = \frac{\sigma}{\omega_n} \tag{4.52}$$

The filter response to the step function for $f_d = 10.5$MHz and different values of σ is shown in Fig. 4.7, illustrating the typical distortion that is introduced.

The cross-correlation function between the incoming distorted signal, $\tilde{s}$(t), and the pilot signal replica can be written as

$$\begin{aligned} R_A(\tau') &= \int_{-B}^{+B} G_{ss_p}(f)\exp(j2\pi f\tau')\tilde{H}(f)df \\ &= \int_{-B}^{+B} G_{ss_p}(f)\exp(j2\pi f\tau')\frac{\exp(-j\arctan\frac{2\xi\Omega}{1-\Omega^2})}{\sqrt{(1-\Omega^2)^2 + 4\xi^2\Omega^2}}df \end{aligned} \tag{4.53}$$

or

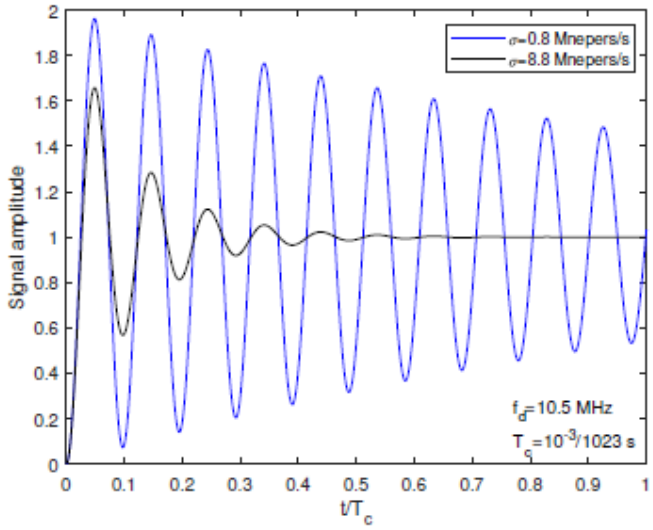

Figure 4.7: Filter response to the step function for $f_d = 10.5$MHz [13].

$$R_A(\tau') = \int_{-B}^{+B} \frac{(1-\Omega^2)G_{ss_p}(f)}{(1-\Omega^2)^2 + 4\xi^2\Omega^2} \cos(2\pi f\tau' - \arctan\frac{2\xi\Omega}{1-\Omega^2})df \tag{4.54}$$

But [13]

$$\cos(\arctan\frac{2\xi\Omega}{1-\Omega^2}) = \frac{1-\Omega^2}{\sqrt{(1-\Omega^2)^2 + 4\xi^2\Omega^2}} \tag{4.55}$$

$$\sin(\arctan\frac{2\xi\Omega}{1-\Omega^2}) = \frac{2\xi\Omega}{\sqrt{(1-\Omega^2)^2 + 4\xi^2\Omega^2}} \tag{4.56}$$

yielding

$$\begin{aligned} R_A(\tau') = &\int_{-B}^{+B} \frac{(1-\Omega^2)G_{ss_p}(f)}{(1-\Omega^2)^2 + 4\xi^2\Omega^2} \cos(2\pi f\tau')\, df \\ &+ 2\xi \int_{-B}^{+B} \frac{\Omega G_{ss_p}(f)}{(1-\Omega^2)^2 + 4\xi^2\Omega^2} \sin(2\pi f\tau')\, df \end{aligned} \tag{4.57}$$

4.2.1 BPSK(10) signal

Replacing the expression in Eq. 3.23 for the cross-spectrum in Eq. 4.57 and doing $\mu = \frac{\omega_n T_c}{2\pi}$, $\rho = \frac{2\pi B}{\omega_n}$, $x = \Omega$, $D = \Delta/T_c$ we obtain

$$\begin{aligned} R_A(\tau') = &2\mu \int_0^{\rho} (1-x^2)Q_1(\mu,\xi,x) \cos\left(2\pi\mu\frac{\tau'}{T_c}x\right) df \\ &+ 4\mu\xi \int_0^{\rho} xQ_1(\mu,\xi,x) \sin\left(2\pi\mu\frac{\tau'}{T_c}x\right) df \end{aligned} \tag{4.58}$$

with

$$Q_1\left(\mu,\xi,x\right)=\frac{0.21\text{sinc}^2(\mu x)}{\left(1-x^2\right)^2+4\xi^2x^2} \tag{4.59}$$

Fig. 4.8 shows the normalized cross-correlation function for TM-B with BPSK(10) signal.

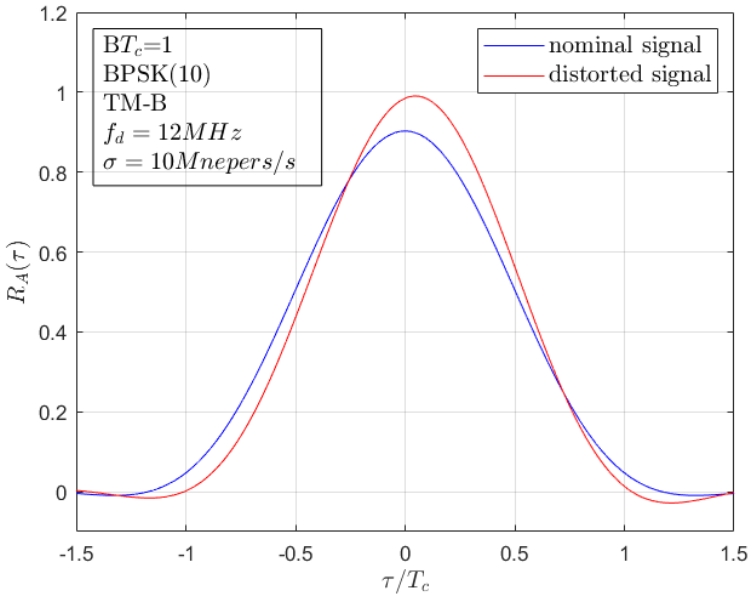

Figure 4.8: Normalized cross-correlations $R_A(\tau)$ for BT_c = 1. TM-B. Modulation: BPSK(10).

4.2.2 AltBOC(15,10) signal

Replacing the expression in Eq. 3.17 for the cross-spectrum in Eq. 4.57 and doing $\mu=\frac{\omega_n T_c}{2\pi}$, $\rho=\frac{2\pi B}{\omega_n}$, $x=\Omega$, $D=\Delta/T_c$ we obtain

$$\begin{aligned}R_A(\tau')=2\mu\int_0^{\rho}(1-x^2)Q_1(\mu,\xi,x)\cos\left(2\pi\mu\frac{\tau'}{T_c}x\right)df\\+4\mu\xi\int_0^{\rho}xQ_1(\mu,\xi,x)\sin\left(2\pi\mu\frac{\tau'}{T_c}x\right)df\end{aligned} \tag{4.60}$$

with

$$\begin{aligned}Q_2\left(\mu,\xi,x\right)=\frac{1}{\left(1-x^2\right)^2+4\xi^2x^2}\left[\frac{B_0}{6}\text{sinc}^2\left(\mu x/6\right)+\sum_{m=1}^{2}\frac{B_m}{3}\text{sinc}^2\left(\mu x/6\right)\cos\left(2\pi\mu x\frac{m}{3}\right)\right.\\\left.+\sum_{n=0}^{5}\frac{C_n}{6}\text{sinc}^2\left(\mu x/12\right)\cos\left(2\pi\mu x\frac{2n+1}{12}\right)\right]\end{aligned} \tag{4.61}$$

Fig. 4.9 shows the normalized cross-correlation function for TM-B with AltBOC(15,10) signal.

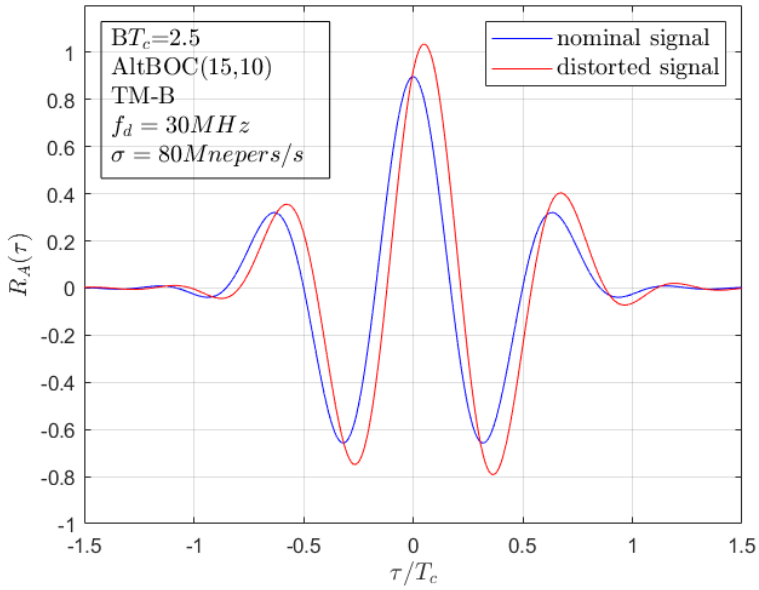

Figure 4.9: Normalized cross-correlations $R_A(\tau)$ for BT_c = 2.5. TM-B. Modulation: AltBOC(15,10).

4.3 Threat Model C

Threat Model C introduces both lead/lag and amplitude modulation. Specifically, it consists of outputs from a second order system when modulated baseband signal suffers from lead or lag. This waveform is a combination of TM-A and TM-B effects [10]. Thus the main difference between the expressions obtained in the case of TM-A and those to be derived for TM-C is that, Eq. 4.8 is now replaced by

$$\begin{aligned} R_A(\tau) &= \mathcal{F}^{-1}\{G_{\tilde{s}s_p}(f)H(f)\tilde{H}(f)\} \\ &= \int_{-\infty}^{+\infty} G_{\tilde{s}s_p}(f)H(f)\tilde{H}(f)\exp(j2\pi f\tau)df \end{aligned} \tag{4.62}$$

where $H(f)$ stands for the channel filter (due essentially to the receiver's front-end filtering effect) and $\tilde{H}(f)$, given by Eq. 4.49, is due to the degradation introduced in the analog section of the satellite [13].

Assuming, once again, an ideal rectangular filter of bandwidth B and group delay τ_0 for the channel filter, Eq. 4.62 can be simplified to

$$R_A(\tau') = \int_{-B}^{+B} G_{\tilde{s}s_p}(f)\tilde{H}(f)\exp(j2\pi f\tau')df \tag{4.63}$$

4.3.1 Threat Model C1

Considering the TM-A1 model presented in section 4.1.1 we have that $G_{\tilde{s}s_p}(f)$ can be given by Eq. 4.12. Replacing this result in Eq. 4.63 we obtain

$$R_A(\tau) = \frac{1}{2}\int_{-B}^{+B} G_{ss_p}(f)\tilde{H}(f)\exp(j2\pi f\tau')df + \frac{1}{2}\int_{-B}^{+B} G_{ss_p}(f)\tilde{H}(f)\exp(j2\pi f(\tau'-\Delta))df \tag{4.64}$$

and using Eq. 4.50

$$\begin{aligned} R_A(\tau') = &\int_0^{+B} \frac{(1-\Omega^2)G_{ss_p}(f)}{(1-\Omega^2)^2+4\xi^2\Omega^2}\cos(2\pi f\tau')\,df \\ &+ 2\xi\int_0^{+B} \frac{\Omega G_{ss_p}(f)}{(1-\Omega^2)^2+4\xi^2\Omega^2}\sin(2\pi f\tau')\,df \\ &+ \int_0^{+B} \frac{(1-\Omega^2)G_{ss_p}(f)}{(1-\Omega^2)^2+4\xi^2\Omega^2}\cos(2\pi f(\tau'-\Delta))\,df \\ &+ 2\xi\int_0^{+B} \frac{\Omega G_{ss_p}(f)}{(1-\Omega^2)^2+4\xi^2\Omega^2}\sin(2\pi f(\tau'-\Delta))\,df \end{aligned} \tag{4.65}$$

4.3.1.1 BPSK(10) signal

For the case of a BPSK(10) signal, the power spectrum is given by Eq. 3.23. Replacing this result in Eq. 4.65 yields

$$\begin{aligned} R_A(\tau') = &\mu\int_0^{\rho}\left(1-x^2\right)Q_1(\mu,\xi,x)\cos\left(2\pi\mu\frac{\tau'}{T_c}x\right)dx \\ &+ 2\mu\xi\int_0^{\rho} xQ_1(\mu,\xi,x)\sin\left(2\pi\mu\frac{\tau'}{T_c}x\right)dx \\ &+ \mu\int_0^{\rho}\left(1-x^2\right)Q_1(\mu,\xi,x)\cos\left[2\pi\mu\left(\frac{\tau'}{T_c}-D\right)x\right]dx \\ &+ 2\mu\xi\int_0^{\rho} xQ_1(\mu,\xi,x)\sin\left[2\pi\mu\left(\frac{\tau'}{T_c}-D\right)x\right]dx \end{aligned} \tag{4.66}$$

with $\mu = \frac{\omega_n T_c}{2\pi}$, $\rho = \frac{2\pi B}{\omega_n}$, $x = \Omega$, $D = \Delta/T_c$ and $Q_1(\mu,\xi,x)$ defined in Eq. 4.59.

Fig. 4.10 shows the normalized crosscorrelation function for TM-C1 with BPSK(10) signal.

4.3.1.2 AltBOC(15,10) signal

Considering, instead, an AltBOC(15,10) signal with the power spectrum in Eq. 3.17 we obtain

$$\begin{aligned} R_A(\tau') = &\mu\int_0^{\rho}\left(1-x^2\right)Q_2(\mu,\xi,x)\cos\left(2\pi\mu\frac{\tau'}{T_c}x\right)dx \\ &+ 2\mu\xi\int_0^{\rho} xQ_2(\mu,\xi,x)\sin\left(2\pi\mu\frac{\tau'}{T_c}x\right)dx \\ &+ \mu\int_0^{\rho}\left(1-x^2\right)Q_2(\mu,\xi,x)\cos\left[2\pi\mu\left(\frac{\tau'}{T_c}-D\right)x\right]dx \\ &+ 2\mu\xi\int_0^{\rho} xQ_2(\mu,\xi,x)\sin\left[2\pi\mu\left(\frac{\tau'}{T_c}-D\right)x\right]dx \end{aligned} \tag{4.67}$$

with $Q_2(\mu,\xi,x)$ defined in Eq. 4.61.

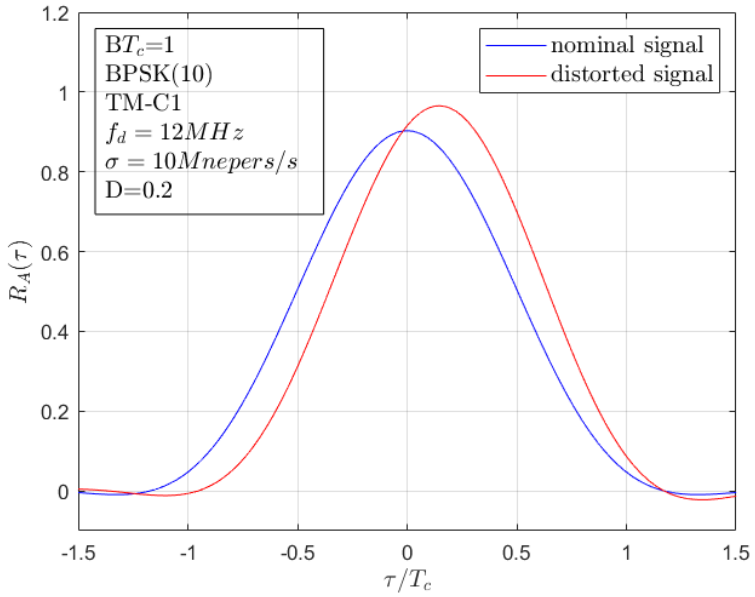

Figure 4.10: Normalized crosscorrelations $R_A(\tau)$ for BT_c = 1. TM-C1. Modulation: BPSK(10).

It is important to note that the formula presented in Eq. 4.67 is only valid for $|\Delta| < T_c/12$. The same analysis could be conducted for the extended TM-A1 model presented in Appendix B. However, for the study of the SQM techniques with the threat model TM-C1, it was not deemed necessary to increase the threat space (TS) beyond $|\Delta| < T_c/12$. Thus, this analysis is not presented.

Fig. 4.11 shows the normalized crosscorrelation function for TM-C1 with AltBOC(15,10) signal.

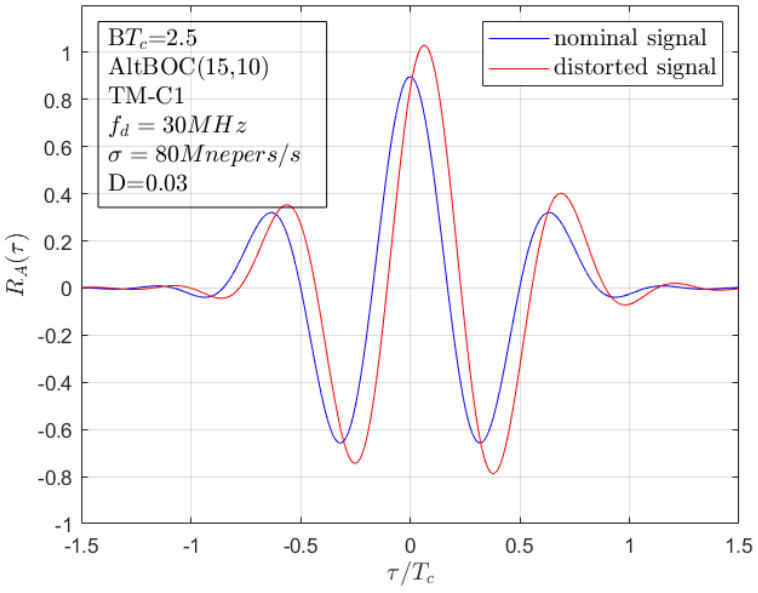

Figure 4.11: Normalized crosscorrelations $R_A(\tau)$ for BT_c = 2.5. TM-C1. Modulation: AltBOC(15,10).

4.3.2 Threat Model TM-C2

Similarly to what was done previously, in this section only the AltBOC(15,10) signal will be covered as it is the only one with subcarriers present.

4.3.2.1 AltBOC(15,10) signal

In the presence of a distortion of the type TM-C2, the receiver output correlation is given by Eq. 4.63 with $G_{\tilde{s}s_p}$ defined in Eq. 4.46.

$$\begin{aligned} R_A(\tau') = & \int_{-B}^{+B} G_{ss_p}(f)\tilde{H}(f)\exp(j2\pi f\tau')df \\ & + \frac{T_c}{\pi^2}\int_{-B}^{+B} \mathrm{sinc}^2(T_c(f-f_s))[\exp(-j2\pi f_s\Delta_s)-1]\tilde{H}(f)\exp(j2\pi f\tau')df \\ & + \frac{T_c}{\pi^2}\int_{-B}^{+B} \mathrm{sinc}^2(T_c(f+f_s))[\exp(j2\pi f_s\Delta_s)-1]\tilde{H}(f)\exp(j2\pi f\tau')df \end{aligned} \tag{4.68}$$

Using Eq. 4.50 we obtain

$$\begin{aligned} R_A(\tau') = & 2\int_0^{+B} \frac{(1-\Omega^2)G_{ss_p}(f)}{(1-\Omega^2)^2+4\xi^2\Omega^2}\cos(2\pi f\tau')\,df \\ & + 4\xi\int_0^{+B} \frac{\Omega G_{ss_p}(f)}{(1-\Omega^2)^2+4\xi^2\Omega^2}\sin(2\pi f\tau')\,df \\ & + \frac{2T_c}{\pi^2}\int_0^{+B} \frac{(1-\Omega^2)\mathrm{sinc}^2(T_c(f-f_s)))}{(1-\Omega^2)^2+4\xi^2\Omega^2}\left[\cos\left[2\pi(f\tau'-f_s\Delta_s)\right]-\cos(2\pi f\tau')\right]df \\ & + \frac{4\xi T_c}{\pi^2}\int_0^{+B} \frac{\Omega\mathrm{sinc}^2(T_c(f-f_s)))}{(1-\Omega^2)^2+4\xi^2\Omega^2}\left[\sin\left[2\pi(f\tau'-f_s\Delta_s)\right]-\sin(2\pi f\tau')\right]df \\ & + \frac{2T_c}{\pi^2}\int_0^{+B} \frac{(1-\Omega^2)\mathrm{sinc}^2(T_c(f+f_s)))}{(1-\Omega^2)^2+4\xi^2\Omega^2}\left[\cos\left[2\pi(f\tau'+f_s\Delta_s)\right]-\cos(2\pi f\tau')\right]df \\ & + \frac{4\xi T_c}{\pi^2}\int_0^{+B} \frac{\Omega\mathrm{sinc}^2(T_c(f+f_s)))}{(1-\Omega^2)^2+4\xi^2\Omega^2}\left[\sin\left[2\pi(f\tau'+f_s\Delta_s)\right]-\sin(2\pi f\tau')\right]df \end{aligned} \tag{4.69}$$

Finally, replacing $G_{ss_p}(f)$ by Eq. 3.17 and doing $\mu = \frac{\omega_n T_c}{2\pi}$, $\rho = \frac{2\pi B}{\omega_n}$, $x = \Omega$, $D = \Delta/T_c$ we obtain

$$\begin{aligned} R_A(\tau') = & \mu\int_0^{\rho} \left(1-x^2\right)Q_2(\mu,\xi,x)\cos\left(2\pi\mu\frac{\tau'}{T_c}x\right)dx \\ & + 2\mu\xi\int_0^{\rho} xQ_2(\mu,\xi,x)\sin\left(2\pi\mu\frac{\tau'}{T_c}x\right)dx \\ & + \frac{2\mu}{\pi^2}\int_0^{\rho}(1-x^2)Q_3(\mu,\xi,x)\left[\cos\left[2\pi(\mu\frac{\tau'}{T_c}x-kD_s)\right]-\cos(2\pi\mu\frac{\tau'}{T_c}x)\right]dx \\ & + \frac{4\mu\xi}{\pi^2}\int_0^{\rho} xQ_3(\mu,\xi,x)\left[\sin\left[2\pi(\mu\frac{\tau'}{T_c}x-kD_s)\right]-\sin(2\pi\mu\frac{\tau'}{T_c}x)\right]dx \\ & + \frac{2\mu}{\pi^2}\int_0^{\rho}(1-x^2)Q_4(\mu,\xi,x)\left[\cos\left[2\pi(\mu\frac{\tau'}{T_c}x-kD_s)\right]-\cos(2\pi\mu\frac{\tau'}{T_c}x)\right]dx \\ & + \frac{4\mu\xi}{\pi^2}\int_0^{\rho} xQ_4(\mu,\xi,x)\left[\sin\left[2\pi(\mu\frac{\tau'}{T_c}x-kD_s)\right]-\sin(2\pi\mu\frac{\tau'}{T_c}x)\right]dx \end{aligned} \tag{4.70}$$

with $Q_2\left(\mu,\xi,x\right)$ defined in Eq. 4.61, $k=\frac{f_s}{f_c}=1.5$ and

$$Q_3\left(\mu,\xi,x\right)=\frac{\mathrm{sinc}^2(\mu x-k)}{(1-x^2)^2+4\xi^2x^2} \tag{4.71}$$

$$Q_4\left(\mu,\xi,x\right)=\frac{\mathrm{sinc}^2(\mu x+k)}{(1-x^2)^2+4\xi^2x^2} \tag{4.72}$$

Fig. 4.12 shows the normalized crosscorrelation function for TM-C2 with AltBOC(15,10) signal.

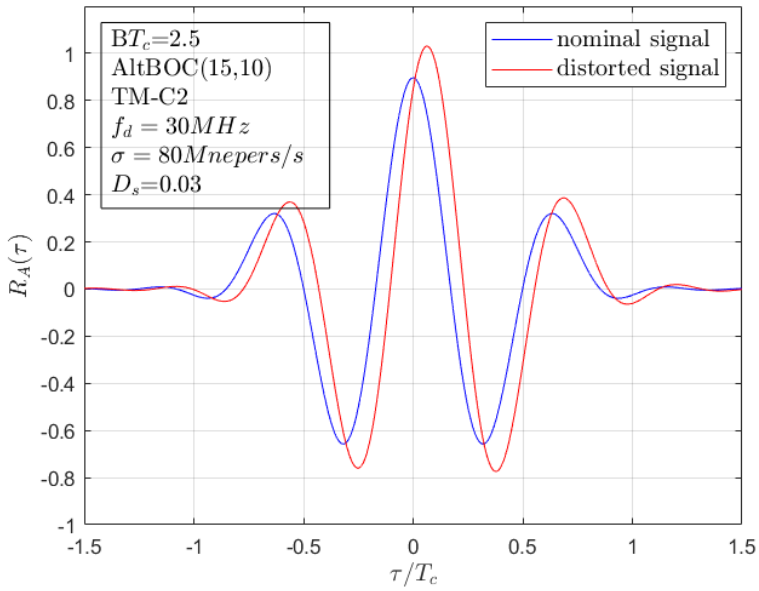

Figure 4.12: Normalized crosscorrelations $R_A(\tau)$ for BT_c = 2.5. TM-C2. Modulation: AltBOC(15,10).

Chapter 5

Signal Quality Monitoring Techniques

After proposing several EWF TMs for the BPSK(10) and AltBOC(15,10) signals in the previous chapters, it is necessary to make sure that the distortions which generate hazardous effects on the receivers are detected

In this chapter, the SQM techniques employed to detect the distortions introduced by the proposed threat models will be presented. These techniques consist on combining measurements estimated from the correlator outputs in order to form metrics that are compared to their nominal values.

In section 5.1, the correlator outputs are characterized. It is presented a statistical analysis of the correlator outputs.

In section 5.2, several metrics and tests to be employed by the SQM will be presented. An approach to define the thresholds for each test, using the Neyman-Pearson criterion, will be explained.

5.1 Correlator Outputs Analysis

Consider a receiver constituted by a bank of $2N + 1$ correlators, as sketched in Fig. 5.1 [6, 19].

In the figure, $r(t)$ is the received signal which includes the GNSS signal of power P and additive white Gaussian noise of power spectral density $N_0/2$. The corresponding carrier-to-noise ratio is (C/N_0) = P/N_0. The correlators spacing is Δ and ϵ denotes the code synchronization error. The baseband signal is

$$y(t) = \sqrt{2P}\tilde{s}(t) * h(t) + n(t) \tag{5.1}$$

where $\tilde{s}(t)$ is the complex baseband GNSS distorted signal, $h(t)$ the filter impulse response and $n(t)$ is complex Gaussian lowpass noise given by

$$n(t) = n_I(t) + jn_Q(t) \tag{5.2}$$

with power spectral density

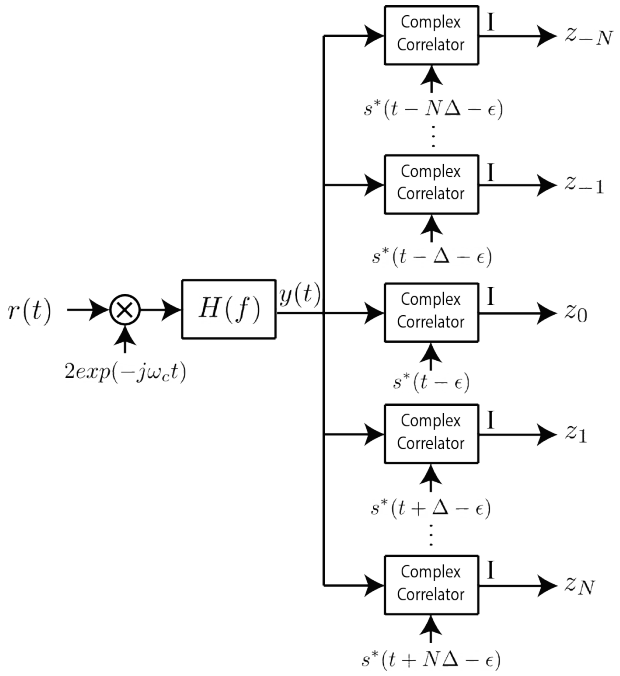

Figure 5.1: Receiver with bank of correlators.

$$G_{n_I}(f) = G_{n_Q}(f) = N_0|H(f)|^2 \approx N_0 \Pi\left(\frac{f}{2B}\right) \tag{5.3}$$

where B is the baseband filter bandwidth.

The real part of the complex correlator outputs are

$$Z_i = \overline{Z_i} + n_i, \quad i = 0, \pm ..., \pm N \tag{5.4}$$

with

$$\overline{Z_i} = \sqrt{2P} R_A(\epsilon - i\Delta) \tag{5.5}$$

The additive noise are

$$\begin{aligned} n_i =& \frac{1}{T}\int_0^T n_I(t) s_I(t - i\Delta - \epsilon)dt \\ &+ \frac{1}{T}\int_0^T n_Q(t) s_Q(t - i\Delta - \epsilon)dt, \quad i = 0, \pm ..., \pm N \end{aligned} \tag{5.6}$$

being correlated, zero-mean, Gaussian random variables, with common variance given by

$$\begin{aligned}\sigma_N^2 &= \frac{1}{T^2}\int_0^T\int_0^T E\{n_I(t)n_I(\lambda)\}s_I(t-i\Delta-\epsilon)s_I(\lambda-i\Delta-\epsilon)dtd\lambda \\ &+ \frac{1}{T^2}\int_0^T\int_0^T E\{n_Q(t)n_Q(\lambda)\}s_Q(t-i\Delta-\epsilon)s_Q(\lambda-i\Delta-\epsilon)dtd\lambda \\ &+ \frac{2}{T^2}\int_0^T\int_0^T E\{n_I(t)n_Q(\lambda)\}s_I(t-i\Delta-\epsilon)s_Q(\lambda-i\Delta-\epsilon)dtd\lambda\end{aligned} \tag{5.7}$$

But the in-phase and quadrature noise components are independent, thus, $E\{n_I(t)n_Q(\lambda)\} = 0$. Furthermore,

$$E\{n_I(t)n_I(\lambda)\} = E\{n_Q(t)n_Q(\lambda)\} = \mathcal{F}^{-1}\{G_{n_I}(f)\} = 2BN_0\mathrm{sinc}\left[2\mathrm{B}(\mathrm{t}-\lambda)\right] \tag{5.8}$$

Thus,

$$\begin{aligned}\sigma_N^2 &= \frac{1}{T^2}\int_0^T\int_0^T 2BN_0\mathrm{sinc}\left[2\mathrm{B}(\mathrm{t}-\lambda)\right]\mathrm{s_I}(\mathrm{t}-\mathrm{i}\Delta-\epsilon)\mathrm{s_I}(\lambda-\mathrm{i}\Delta-\epsilon)\mathrm{dtd}\lambda \\ &+ \frac{1}{T^2}\int_0^T\int_0^T 2BN_0\mathrm{sinc}\left[2\mathrm{B}(\mathrm{t}-\lambda)\right]\mathrm{s_Q}(\mathrm{t}-\mathrm{i}\Delta-\epsilon)\mathrm{s_Q}(\lambda-\mathrm{i}\Delta-\epsilon)\mathrm{dtd}\lambda\end{aligned} \tag{5.9}$$

Eq. 5.9 is really hard to compute. However, since, in general, $2BT \gg 1$, we can greatly simplify it by making $2B\mathrm{sinc}\left[2\mathrm{B}(\mathrm{t}-\lambda)\right] \approx \mathrm{N}_0\delta(\mathrm{t}-\lambda)$. Therefore,

$$\sigma_N^2 = \frac{N_0}{T^2}\int_0^T \left[s_I^2(\lambda-i\Delta-\epsilon) + s_Q^2(\lambda-i\Delta-\epsilon)\right]d\lambda = \frac{N_0}{T}\left[R_{s_I}(0) + R_{s_Q}(0)\right] = \frac{N_0}{T}R_s(0) \tag{5.10}$$

If the power of the received signal is normalized, i.e., $R_s(0) = 1$ watt, then

$$\sigma_N^2 = \frac{N_0}{T} = \frac{1}{(C/N_0)T} \tag{5.11}$$

Similarly, the crosscorrelations between the correlators' noises yielding

$$E\{n_i n_k\} = \frac{N_0}{T}R_s((k-i)\Delta) \tag{5.12}$$

The noise covariance matrix can, therefore, be written as

$$C = \frac{N_0}{T}\begin{bmatrix} 1 & \frac{R_s(\Delta)}{R_s(0)} & \cdots & \frac{R_s(2N\Delta)}{R_s(0)} \\ \vdots & \vdots & \ddots & \vdots \\ \frac{R_s(2N\Delta)}{R_s(0)} & \frac{R_s((2N-1)\Delta)}{R_s(0)} & \cdots & 1 \end{bmatrix} \tag{5.13}$$

Appendix C describes how to generate a noise vector $[n_{-N}, ..., n_0, ..., n_N]^T$ with covariance matrix C (Eq. 5.13) using independent, zero-mean, Gaussian r.v. of unity variance.

5.2 Metrics and Tests

SQM consists of a test to evaluate if the signal is affected by a distortion or not. These tests are based on the use of metrics, μ, to detect distortions of the correlation function. It consists in comparing the difference between the measured value of the metric and its nominal value to a threshold. The test based on a given metric j using the correlator output i is, mathematically, defined by

$$T_j^i = \frac{\mu_{j,\text{mea}}^i - \mu_{j,\text{nom}}^i}{\lambda_j^i} \tag{5.14}$$

where $\mu_{j,\text{mea}}^i$ is the measured value of the metric j using the correlator output i that can be affected by a distortion, $\mu_{j,\text{nom}}^i$ is the nominal value of the metric j (without additive noise or distortion) using the correlator output i and λ_j^i is the detection threshold associated to the metric j using the correlator output i, determined according to a required false alarm probability as explained later in this section. In practice, estimating the nominal value of a metric is usually a difficult task. A solution presented in [16] is to compute the median of that metric across all satellites in view. The method presented by Pagot, [3], is to estimate the nominal value from the average value of that metric for a given PRN.

In order to detect a faulty case in real time, a Neyman-Pearson hypothesis test is performed [32]. Consider the two hypotheses, H_0 (signal is not distorted) and H_1(signal is distorted). If $T_j^i < 1$, it is assumed that the signal is not distorted; whereas if $T_j^i \geq 1$, the signal is considered to be distorted. For a given test, we can, therefore, define the following probabilities:

$$P_{fa} = \text{prob}\{T_j^i \geq 1 | H_0\} \tag{5.15}$$

$$P_{md} = \text{prob}\{T_j^i < 1 | H_1\} \tag{5.16}$$

It is not possible to minimize simultaneously P_{fa} and P_{md} [6, 19]. The solution herein employed is the Neyman-Pearson criterion which consists of fixing P_{fa} in order to comply with the requirements and then minimizing P_{md} [32].

The probabilities of false alarm and missing detection are schematized in Fig. 5.2 and follow the Neyman-Pearson criterion described previously.

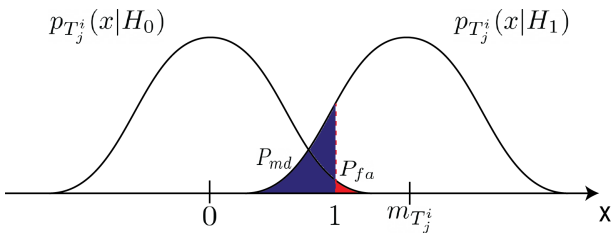

Figure 5.2: Probability density functions of the test T_i for hypotheses H_0 and H_1.

In [3], three tests based on ratio metrics were proposed: simple ratio metric, difference ratio metric and sum ratio metric. These are the metrics used in this dissertation.

5.2.1 Simple Ratio Metric

The tests based on ratio metrics, such as the simple ratio metric, attempt specifically to detect the presence of deadzones (flat correlation peaks) and abnormally sharp or elevated correlation peaks [16]. More specifically, the Simple Ratio Metric is the easiest metric to implement and permits to detect all kind of correlation function distortions [3].

Assuming that there are $2N+1$ correlators (as sketched in Fig. 5.1), it is possible to form $2N$ simple ratio metrics

$$\mu_1^i = \frac{Z_i}{Z_0}, \;\; i = \pm 1, ..., \pm N \tag{5.17}$$

Replacing this metric in the test (Eq. 5.14) and using the expression for the correlator outputs given in Eq. 5.4, yields

$$T_1^i = \frac{\left(\frac{\overline{Z}_i + n_i}{\overline{Z}_0 + n_0}\right)_{mea} - \left(\frac{\overline{Z}_i}{\overline{Z}_0}\right)_{nom}}{\lambda_1^i} \tag{5.18}$$

In the absence of EWF distortion (hypothesis H_0) the only disturbance in the correlator outputs is the additive noise. Thus, $(\overline{Z}_i)_{mea} = (\overline{Z}_i)_{nom} = \overline{Z}_i$ and $(\overline{Z}_0)_{mea} = (\overline{Z}_0)_{nom} = \overline{Z}_0$ and the test in Eq. 5.18 is

$$T_1^i = \frac{\frac{\overline{Z}_i + n_i}{\overline{Z}_0 + n_0} - \frac{\overline{Z}_i}{\overline{Z}_0}}{\lambda_i} = \frac{n_i - (\overline{Z}_i / \overline{Z}_0) n_0}{(\overline{Z}_0 + n_0)\lambda_1^i} \tag{5.19}$$

It can be shown (see appendix D) that T_1^i can be approximated by a zero-mean r.v. with variance

$$\sigma^2_{T_1^i} = \frac{(1+\rho_i^2)R_s(0) - 2\rho_i R_s(i\Delta)}{2(C/N_0)TR_A^2(0)\left[\lambda_1^i\right]^2} \tag{5.20}$$

with

$$\rho_i = \frac{R_A(i\Delta)}{R_A(0)}, \;\; i \neq 0 \tag{5.21}$$

Assuming that T_1^i is well approximated by a gaussian distribution, the probability of false alarm of the test i is

$$P_{fa}^i = \text{prob}\{T_1^i \geq 1 | H_0\} = Q\left(\frac{1}{\sigma_{T_1^i}}\right) \tag{5.22}$$

where $Q(\cdot)$ is the Gaussian error function defined by

$$Q(x) = \frac{1}{\sqrt{2\pi}} \int_x^\infty \exp(-\frac{y^2}{2}) dy \tag{5.23}$$

Consider now, for simplicity, that all tests have the same probability of false alarm, that is:

$$P_{fa}^i = P_{fa}, \;\; i = \pm 1, ..., \pm N \tag{5.24}$$

Using Eq. 5.20 and Eq. 5.22 we can obtain for the threshold

$$\lambda_1^i = \frac{Q^{-1}(P_{fa})}{R_A(0)} \sqrt{\frac{(1+\rho_i^2)R_s(0) - 2\rho_i R_s(i\Delta)}{2(C/N_0)T}} \tag{5.25}$$

where P_{fa} is such that the overall probability of false alarm is $P_{FA} = 1.5 \times 10^{-7}$. In this work we will consider a M of N search detection [1]. This criterion consists in declaring the presence of an anomaly if M (for $M \leq N$) or more tests assume that an anomaly is present. For simplicity we will consider henceforth that $M = 1$. Using this criterion and assuming independent tests, the overall probability of false alarm can be writen in terms of the single test probability of false alarm, P_{fa}, using a binominal distribution. Taking into considering the $2N$ possible tests

$$\begin{aligned} P_{FA} &= \sum_{k=1}^{2N} \binom{2N}{k} P_{fa}^k (1-P_{fa})^{2N-k} \\ &= 1 - (1-P_{fa})^{2N} \end{aligned} \tag{5.26}$$

Given that $P_{fa} << 1$, we can use the binomial approximation yielding

$$P_{FA} \approx 1 - (1 - 2NP_{fa}) = 2NP_{fa} \tag{5.27}$$

Hence, the threshold in Eq. 5.25 can be rewritten as

$$\lambda_1^i = \frac{Q^{-1}(P_{FA}/(2N))}{R_A(0)} \sqrt{\frac{(1+\rho_i^2)R_s(0) - 2\rho_i R_s(i\Delta)}{2(C/N_0)T}} \tag{5.28}$$

5.2.2 Difference Ratio Metric

This metric permits to detect distortions that affect the correlation function in an asymmetric way (asymmetry from the prompt) more efficiently than the simple ratio metric [3].

Considering the $2N+1$ correlators (Fig. 5.1) we can form N difference ratio metrics

$$\mu_2^i = \frac{Z_{-i} - Z_i}{Z_0}, \;\; i = 1, ..., N \tag{5.29}$$

Replacing this metric in the test (Eq. 5.14) and using the expression for the correlator outputs given in Eq. 5.4, yields

$$T_2^i = \frac{\left(\frac{\overline{Z}_{-i} + n_{-i} - \overline{Z}_i - n_i}{\overline{Z}_0 + n_0}\right)_{mea} - \left(\frac{\overline{Z}_{-i} - \overline{Z}_i}{\overline{Z}_0}\right)_{nom}}{\lambda_2^i} = \frac{\left(\frac{\overline{Z}_{-i} + n_{-i} - \overline{Z}_i - n_i}{\overline{Z}_0 + n_0}\right)_{mea}}{\lambda_2^i} \tag{5.30}$$

In the absence of EWF distortion (hypothesis H_0) the only disturbance in the correlator outputs is the additive noise. Thus, $(\overline{Z}_{-i})_{mea} = (\overline{Z}_i)_{mea}$ and the test in Eq. 5.30 is

$$T_2^i = \frac{n_{-i} - n_i}{\overline{Z}_0 + n_0 \lambda_2^i} \tag{5.31}$$

It can be shown (see appendix D) that T_2^i is a zero-mean r.v. with variance

$$\sigma^2_{T_2^i} = \frac{R_s(0) - R_s(2i\Delta)}{(C/N_0)TR_A^2(0)\left[\lambda_2^i\right]^2} \tag{5.32}$$

Assuming that T_2^i is well approximated by a Gaussian distribution, the probability of false alarm of the test i is

$$P_{fa}^i = \text{prob}\{|T_2^i| \geq 1|H_0\} = 2Q\left(\frac{1}{\sigma_{T_2^i}}\right) \tag{5.33}$$

Similarly to what was done for the Simple Ratio Metric, we assume that all tests are characterized by a common probability of false alarm (P_{fa}).

Using Eq. 5.32 and Eq. 5.33 we can obtain for the threshold

$$\lambda_2^i = \frac{Q^{-1}(P_{fa}/2)}{R_A(0)}\sqrt{\frac{R_s(0) - R_s(2i\Delta)}{(C/N_0)T}} \tag{5.34}$$

where, once again, P_{fa} is such that the overall probability of false alarm is $P_{FA} = 1.5 \times 10^{-7}$. Following a similar procedure as the one for the simple ratio tests, taking into considering the N possible tests we obtain for the overall probability of false alarm $P_{FA} \approx NP_{fa}$. Hence, the threshold in Eq. 5.34 can be rewritten as

$$\lambda_2^i = \frac{Q^{-1}(P_{FA}/(2N))}{R_A(0)}\sqrt{\frac{R_s(0) - R_s(2i\Delta)}{(C/N_0)T}} \tag{5.35}$$

5.2.3 Sum Ratio Metric

This metric permits to detect distortions that affect the correlation function in an symmetric way (symmetry from the prompt) more efficiently than the simple ratio metric [3].

Considering the $2N + 1$ correlators (Fig. 5.1) we can form N sum ratio metrics

$$\mu_3^i = \frac{Z_{-i} + Z_i}{Z_0}, \;\; i = 1, ..., N \tag{5.36}$$

Replacing this metric in the test (Eq. 5.14) and using the expression for the correlator outputs given in Eq. 5.4, yields

$$T_3^i = \frac{\left(\frac{\overline{Z}_{-i}+n_{-i}+\overline{Z}_i+n_i}{\overline{Z}_0+n_0}\right)_{mea} - \left(\frac{\overline{Z}_{-i}+\overline{Z}_i}{\overline{Z}_0}\right)_{nom}}{\lambda_3^i} = \frac{\left(\frac{\overline{Z}_{-i}+n_{-i}+\overline{Z}_i+n_i}{\overline{Z}_0+n_0}\right)_{mea}}{\lambda_3^i} - 2\frac{\rho_i}{\lambda_3^i} \tag{5.37}$$

with ρ_i given by Eq. 5.21.

In the absence of EWF distortion (hypothesis H_0) the only disturbance in the correlator outputs is the additive noise. Thus, $(\overline{Z}_{-i})_{mea} = (\overline{Z}_i)_{mea} = \overline{Z}_i = \rho\overline{Z}_0$ and the test in Eq. 5.37 is

$$T_3^i = \frac{n_{-i} + n_i - 2\rho_i n_0}{\overline{Z}_0 + n_0\lambda_3^i} \tag{5.38}$$

It can be shown (see appendix D) that T_2^i is a zero-mean r.v. with variance

$$\sigma^2_{T_3^i} = \frac{(1+2\rho^2)R_s(0) + R_s(2i\Delta) - 4\rho_i R_s(i\Delta)}{(C/N_0)TR_A^2(0)[\lambda_3^i]^2} \tag{5.39}$$

Assuming that T_3^i is well approximated by a Gaussian distribution, the probability of false alarm of the test i is

$$P_{fa}^i = \text{prob}\{T_3^i \geq 1 | H_0\} = Q\left(\frac{1}{\sigma_{T_3^i}}\right) \tag{5.40}$$

Similarly to what was done previously, we assume that all tests are characterized by a common probability of false alarm (P_{fa}).

Using Eq. 5.39 and Eq. 5.40 we can obtain for the threshold

$$\lambda_3^i = \frac{Q^{-1}(P_{fa})}{R_A(0)}\sqrt{\frac{(1+2\rho^2)R_s(0) + R_s(2i\Delta) - 4\rho_i R_s(i\Delta)}{(C/N_0)T}} \tag{5.41}$$

where, once more, P_{fa} is such that the overall probability of false alarm is $P_{FA} = 1.5\times10^{-7}$. Following a similar procedure as the one for the simple ratio tests, taking into considering the N possible tests we obtain for the overall probability of false alarm $P_{FA} \approx NP_{fa}$. Hence, the threshold in Eq. 5.41 can be rewritten as

$$\lambda_3^i = \frac{Q^{-1}(P_{FA}/N)}{R_A(0)}\sqrt{\frac{(1+2\rho^2)R_s(0) + R_s(2i\Delta) - 4\rho_i R_s(i\Delta)}{(C/N_0)T}} \tag{5.42}$$

Chapter 6

Implementation and Results

In this chapter, we propose to apply the tests and metrics introduced in chapter 5 to detect EWF distortions described by the threat models presented in chapter 4.

In section 6.1 the different aspects for each processing option are presented. Namely, it is described the threat models corresponding to each processing option, as well as, the SQM characteristics.

In section 6.2 the results obtained are presented. These results are divided in three groups according to the type of EWF distortion. It is also established a comparison between each receiver's performance.

6.1 Implementation Aspects

The performance of the EWF anomaly detectors in the presence of several types of anomalies will be carried out for different types of signal processing (whole E5 signal, sub-bands E5a/E5b or E5a+E5b). Each one of these scenarios will have differences when it comes to the threat models employed and/or the SQM techniques.

The results will be displayed as plots of detectability and hazard regions. An anomaly will be considered to be successfully detected if the probability of missing detection is $P_{md} \leq 10^{-3}$ for a probability of false alarm $P_{FA} = 1.5 \times 10^{-7}$. However, in certain cases the failure to detect the anomaly will not be harmful to the receiver's operation as it can lead to a code discriminator error smaller than a certain pre-defined value called Maximum-Allowable Error in Range (MERR). Undetected EWF anomalies that yield code discriminator errors above the MERR constitute the hazard region. To determine the hazard region, besides detecting the anomalies, the simulation program must compute the associated code discriminator errors.

The equilibrium solution of the code discriminator with E-L spacing Δ_{EL} requires that

$$R_A(\tau_1) = R_A(\tau_2), \quad \text{with} \quad \tau_2 = \tau_1 + \Delta_{\mathrm{EL}} \tag{6.1}$$

The equilibrium solution is the mid position of τ_1 and τ_2. That is

$$\epsilon = \frac{\tau_1 + \tau_2}{2} = \tau_1 + \frac{\Delta_{\mathrm{EL}}}{2} \tag{6.2}$$

In the absence of EWF anomaly the filtered version of the code ACF exhibits symmetry around its maximum leading to $\epsilon = 0$ and the DLL presents no tracking error. In the presence of EWF anomaly the filtered code ACF typically presents a shift regarding the version without EWF or an asymmetry, or both effects (see example in Fig. 4.11). In those scenarios, typically $\epsilon \neq 0$, which corresponds to a tracking error of the DLL. The two scenarios (with and without EWF anomaly) are illustrated in Fig. 6.1.

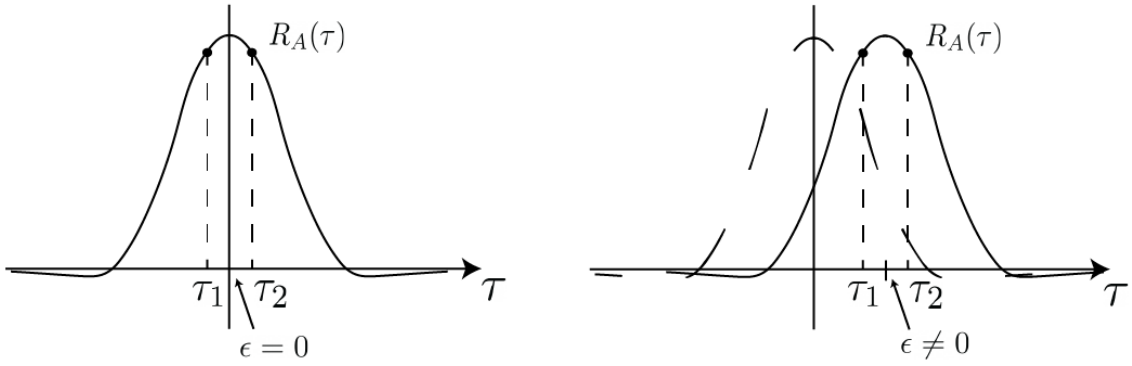

(a) Scenario without EWF.

(b) Scenario with EWF.

Figure 6.1: Code discriminator equilibrium solution with E-L spacing.

Computing the DLL tracking error ϵ from Eq. 6.1 and Eq. 6.2 is, in general, cumbersome when the expressions of the ACF $R_A(\tau)$ are complicated. For this reason, numerical computations was carried out.

The required number of Monte Carlo runs was obtained using the halt criterion described in appendix E. In order to obtain a confidence level of 95% ($\alpha = 0.05$) and a length of the confidence interval of $L = 0.4p$ it was seen that $n \approx 100$ missed detections were required. Taking into consideration that the target probability of missed detection is $P_{md} = 10^{-3}$, a total number of runs $N = 100/10^{-3} = 10^5$ are needed. Even though the halt criterion in appendix E suggests the use of a variable number of runs, having a fixed number of Monte Carlo runs was seen to be beneficial in order to take advantage of Matlab's matrix computational performance.

6.1.1 Processing the whole AltBOC signal

The first scenario considered is the one where the whole E5 signal is processed. Naturally, for this scenario, we will consider the threat models developed for the AltBOC(15,10) signal in chapter 4. It will be assumed an ideal code delay synchronization for the DLL using a pair of correlators with early-late spacing equal to $0.1T_c$. However, we have not included channel noise aiming to simulate the noise reduction introduced by the DLL loop filter [19]. For this reason, the value chosen for the DLL spacing doesn't influence too much the results.

As for the SQM, we will consider the bank of correlators sketched in Fig. 5.1 where $H(f)$ is an ideal rectangular filter with bandwidth $B_{RF} = 51.15$ MHz. This bandwidth is the receiver reference bandwidth for the E5 signal [20]. The considered baseband bandwidth chip rate product is, therefore, $BT_c = 2.5$. The number of pair of correlators, N, and the spacing, Δ, were obtained by minimizing the hazardous

region as will be seen later.

It is stated in [19] that the best SQM results are obtained when using all the tests mentioned in section 5.2. Consequently, all $2N$ simple ratio tests, N difference ratio tests and N sum ratio tests are used. The thresholds were adjusted to achieve an overall probability of false alarm $P_{FA} = 1.5 \times 10^{-7}$. The probability is defined as

$$P_{FA} = 1 - \text{prob}\{T_1^{-i} < 1, T_1^i < 1, |T_2^i| < 1, T_3^i < 1, i = 1, ..., N | H_0\} \tag{6.3}$$

where T_j^i denotes the output of test j (with $j = 1, 2, 3$) obtained with the correlator pair of index i as depicted in Fig. 5.1. The hypothesis H_0 assumes that the incoming signal is not distorted and is only affected by additive Gaussian white noise and front-end filtering.

The thresholds λ_1^i, λ_2^i and λ_3^i are defined by Eq. 5.28, Eq. 5.35 and Eq. 5.42, respectively. However, the overall probability of false alarm, P_{FA}, has to be adjusted to take into consideration the new number of tests. Therefore, P_{FA} is replaced by $P_{FA}/3$ as we are assuming that each of the three tests contributes with one third to the overall probability of false alarm, yielding

$$\lambda_1^i = \frac{Q^{-1}(P_{FA}/(6N))}{R_A(0)} \sqrt{\frac{(1+\rho_i^2)R_s(0) - 2\rho_i R_s(i\Delta)}{2(C/N_0)T}} \tag{6.4}$$

$$\lambda_2^i = \frac{Q^{-1}(P_{FA}/(6N))}{R_A(0)} \sqrt{\frac{R_s(0) - R_s(2i\Delta)}{(C/N_0)T}} \tag{6.5}$$

$$\lambda_3^i = \frac{Q^{-1}(P_{FA}/(3N))}{R_A(0)} \sqrt{\frac{(1+2\rho^2)R_s(0) + R_s(2i\Delta) - 4\rho_i R_s(i\Delta)}{(C/N_0)T}} \tag{6.6}$$

The hazard region corresponds to the threat space parameters for which the range error exceeds the maximum-allowable error in range (MERR) and the EWF anomaly is not detected. In order to find the optimal values for N and Δ we adopted the criterion of minimizing the hazard region for a pre-defined MERR. Herein, we considered MERR=1m. This value was chosen to be conservative. A more detailed approach on how to compute MERR can be found, for instance, in [3].

Figure 6.2 displays the percentages of the hazard region for three different threat models: TM-A1, TM-A2 and TM-B. The signal-to-noise ratio used for the simulations is $C/N_0 = 50$ dB-Hz.

For TM-A1 the area corresponding to $0 < D < 0.165$ and $0 < T < 0.5$ seconds was considered. This threat space was seen to be sufficient to analyze the action of the SQM. The plot shows that there are two major regions where the criterion is minimized: $\Delta \geq 0.125T_c$ for $N \geq 3$ and $0.165T_c \leq \Delta \leq 0.21T_c$. Even though both regions are valid, the second one is preferable in terms of hardware implementation. The smaller the correlator spacing, the higher the sampling frequency has to be, which in turn, implies the usage of more expensive hardware and larger power consumption. Thus, the first region is not sufficiently better to justify the implementation burden. Therefore, it is going to be neglected.

For TM-A2 the area corresponding to $0 < D_s < 1/12$ and $0 < T < 0.5$ s was considered. The plot shows the criterion is minimized for $0.15T_c \leq \Delta \leq 0.17T_c$ and $N \geq 3$.

Finally, for TM-B the area corresponding to $0 < f_d < 65$ MHz and $0 < \sigma < 400$ Mnepers/s was

considered. The time of correlation was set to $T = 0.5$ s. The plot shows the criterion is minimized for $0.16T_c \leq \Delta \leq 0.22T_c$ for $N \geq 4$.

The remaining thread models (TM-C1 and TM-C2) were not studied due to being a combination of TM-A1/TM-A2 with TM-B, respectively. Thus, it is assumed that minimizing the hazard region of those threat models will also improve the results for TM-C1/TM-C2. Furthermore, conducting this analysis for TM-C1/TM-C2 would be computationally extremely demanding due to the large number of variables.

For the sake of simplicity, the optimal regions obtained for each threat model are described in table 6.1. It is also stated the common region for all the threat models, $N \geq 4$ and $0.165T_c \leq \Delta \leq 0.17T_c$. This is the region of interest when choosing the number of pair of correlators, N, and the spacing, Δ. This analysis shows that there is no improvement in using a number of pair of correlators larger than 4. This result allows us to greatly reduce the complexity of the bank of correlators. Hence, we adopt the value $N = 4$ and $\Delta = 0.17$ for all the simulations presented for the signal E5.

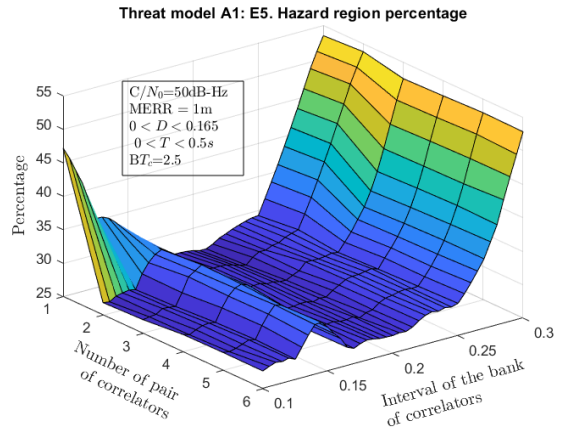

(a) Threat model TM-A1.

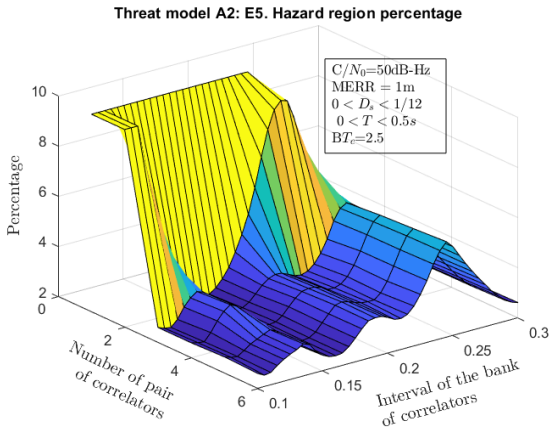

(b) Threat model TM-A2.

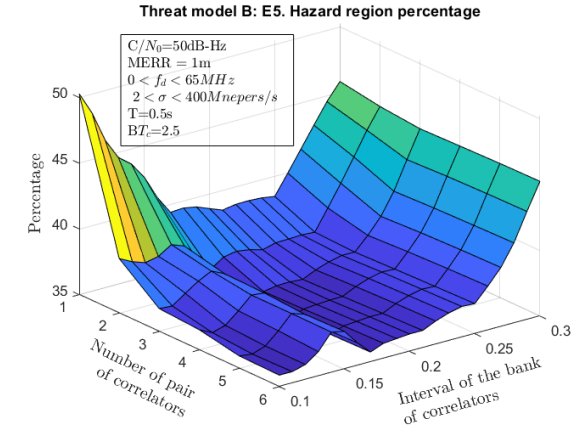

(c) Threat model TM-B.

Figure 6.2: Percentages of the hazard region for three threat models. Signal: E5.

Table 6.1: Optimal region for N and Δ. Signal: E5.

	N	Δ/T_c
TM-A1	[3,6]	[0.165,0.21]
TM-A2	[3,6]	[0.15,0.17]
TM-B	[4,6]	[0.16,0.22]
Union	[4,6]	[0.165,0.17]

6.1.2 Processing one of the sub-bands

The second scenario considered is the processing of one of the sub-bands, either E5a or E5b (henceforth denoted as E5a/E5b). For this scenario, we will consider the threat models developed for the BPSK(10) signal in chapter 4. Once again, it will be assumed an ideal code delay synchronization for the DLL using a pair of correlators with early-late spacing equal to $0.1T_c$. However, we have not included channel noise aiming to simulate the noise reduction introduced by the DLL loop filter [19].

The SQM architecture is really similar to the previous one, apart from the bandwidth. The typical RF bandwidth for a E5a/E5b receiver is $B_{RF} = 20.46$ MHz ([25]) which results in a chip period times baseband bandwidth product of $BT_c = 1$. To improve the SQM results, once more, all the tests will be employed. Assuming that each of the three tests contributes with one third to the overall probability of false alarm, the thresholds are given by Eqs. 6.4-6.6.

The remaining parameters to be defined are N and Δ. Once more, these parameters were chosen to minimize the hazard region for a pre-defined MERR=1m. Figure 6.3 sketches the percentages of the hazard region for two different models: TM-A1 and TM-B. The signal-to-noise ratio used for the simulations is $C/N_0 = 47$ dB-Hz. It is 3 dB less than the signal-to-noise ratio used for the E5 signal simulations. This is because when tracking only one sub-band using a single band receiver, approximately only 50% of the power is utilized when compared with tracking the E5 pilot signal. This is equivalent to a loss of 3 dB.

For TM-A1 the area corresponding to $0 < D < 0.5$ and $0 < T < 0.5$ seconds was considered. This threat space is a little bigger than the one employed for the E5 signal. This is because the signal BPSK(10) yields worse results, hence, the tests only start detecting the presence of anomalies for larger delays. The plot shows that the criterion is minimized for $\Delta \geq 0.16T_c$ for $N \geq 4$.

For TM-B the area corresponding to $0 < f_d < 20$ MHz and $0 < \sigma < 200$ Mnepers/s was considered. Contrarily, this threat space is smaller than the E5 counterpart. This is because the distortions are larger for smaller values of f_d and σ. Hence, the tests stop detecting the presence of anomalies for lower values of those variables. The time of correlation was set to $T = 0.5$ s. The plot shows the criterion is minimized for $\Delta \geq 0.2T_c$ for $N \geq 4$.

The remaining threat model (TM-C1) was not studied due to being a combination of TM-A1 with TM-B. The threat models TM-A2 and TM-C2 are not considered because, as explained in chapter 4, the BPSK(10) signal doesn't have subcarriers.

Notice, also, that the percentages of the hazard region are much higher than the ones obtained for

the E5 signal (Fig. 6.2). Even though this has, in part, to do with the worse performance of the BPSK(10) signal, we cannot neglect the fact that the threat space areas used are different in both cases. Thus, we cannot make any conclusions out of this aspect. The comparison between the two processing options will be presented later.

The optimal regions obtained for each threat model are described in table 6.2. The common region for all the threat models, $N \geq 4$ and $\Delta \geq 0.2T_c$ is also presented. This is the region of interest when choosing the number of pair of correlators, N, and the spacing, Δ. This analysis shows that there is also no improvement in using a number of pair of correlators larger than 4. Hence, we adopt the value $N = 4$ and $\Delta = 0.2T_c$ for all the simulations presented for the signal E5a/E5b.

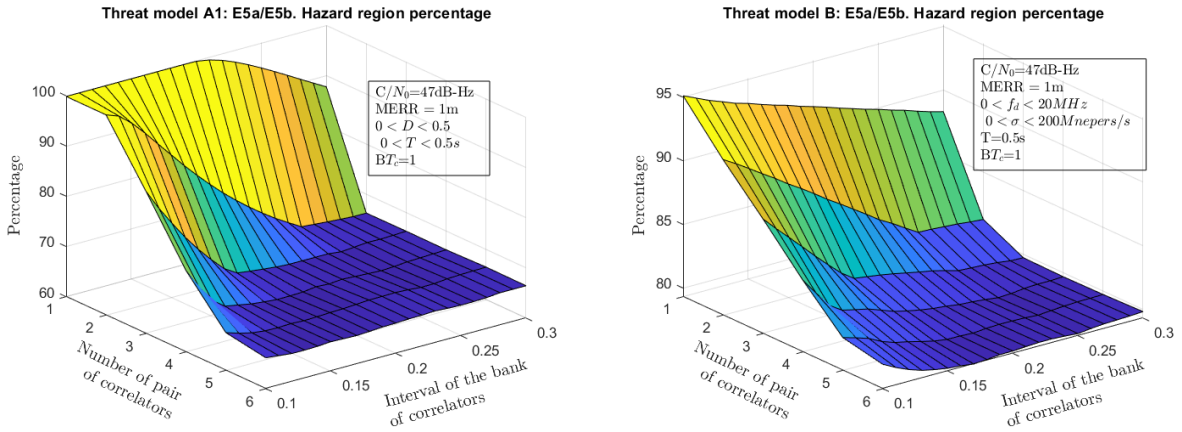

(a) Threat model TM-A1.

(b) Threat model TM-B.

Figure 6.3: Percentages of the hazard region for two threat models. Signal: E5a/E5b.

Table 6.2: Optimal region for N and Δ. Signal: E5a/E5b.

	N	Δ/T_c
TM-A1	[4,6]	[0.16,0.3]
TM-B	[4,6]	[0.2,0.3]
Union	[4,6]	[0.2,0.3]

6.1.3 Processing both sub-bands separately

The third and last scenario considered is the processing of both sub-bands separately. For this scenario, we will consider for each one of the sub-bands the threat models developed for the BPSK(10) signal in chapter 4. Once more, it will be assumed an ideal code delay synchronization for the DLL using a pair of correlators with early-late spacing equal to $0.1T_c$.

The SQM architecture is a little more complex than the previous ones. We will consider two independent banks of correlators, one for each sub-band. Given that the signal E5a and E5b are independent to each other and so are the noises in each sub-band, the outputs of the correlators are also independent. From the outputs of each sub-band, we will form $2N$ simple ratio tests, N difference ratio tests and N sum ratio tests. Thus, we will use twice the number of tests. The overall probability of false alarm is,

therefore, defined as

$$P_{FA} = 1 - \text{prob}\{T^{-i}_{1,E5a} < 1, T^{i}_{1,E5a} < 1, |T^{i}_{2,E5a}| < 1, T^{i}_{3,E5a} < 1, \\ T^{-i}_{1,E5b} < 1, T^{i}_{1,E5b} < 1, |T^{i}_{2,E5b}| < 1, T^{i}_{3,E5b} < 1, i = 1, ..., N | H_0\} \tag{6.7}$$

The thresholds λ^i_1, λ^i_2 and λ^i_3 are derived from Eq. 5.28, Eq. 5.35 and Eq. 5.42, respectively. However, this time, P_{FA} has to be replaced by $P_{FA}/6$ as we are assuming that each of the six tests contributes with one sixth to the overall probability of false alarm, yielding

$$\lambda^i_1 = \frac{Q^{-1}(P_{FA}/(12N))}{R_A(0)} \sqrt{\frac{(1+\rho_i^2)R_s(0) - 2\rho_i R_s(i\Delta)}{2(C/N_0)T}} \tag{6.8}$$

$$\lambda^i_2 = \frac{Q^{-1}(P_{FA}/(12N))}{R_A(0)} \sqrt{\frac{R_s(0) - R_s(2i\Delta)}{(C/N_0)T}} \tag{6.9}$$

$$\lambda^i_3 = \frac{Q^{-1}(P_{FA}/(6N))}{R_A(0)} \sqrt{\frac{(1+2\rho^2)R_s(0) + R_s(2i\Delta) - 4\rho_i R_s(i\Delta)}{(C/N_0)T}} \tag{6.10}$$

The typical RF bandwidth used is $B_{RF} = 20.46$ MHz ([25]) which results in a chip period times baseband bandwidth product of $BT_c = 1$.

Fig. 6.4 shows the Monte Carlo results for P_{FA} of the three processing options with 10^9 independent runs. The results show good agreement with the desired overall probability of false alarm of $P_{FA} = 1.5 \times 10^{-7}$. These results could be improved by refining the thresholds using Monte Carlo simulation. However, to obtain probabilities of false alarm of $P_{FA} = 1.5 \times 10^{-7}$ would require a very large number of runs which becomes rapidly prohibitive.

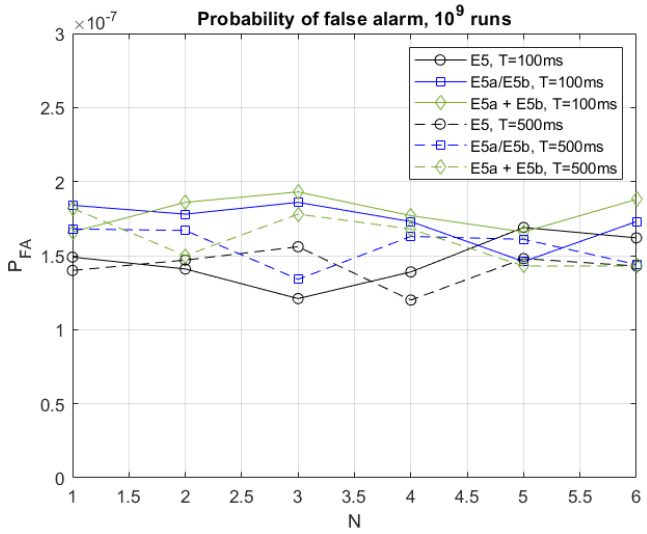

Figure 6.4: Monte Carlo results for P_{FA} obtained with 10^9 independent runs.

The parameters N and Δ still need to be defined. Once more, these parameters were chosen to minimize the hazard region for a pre-defined MERR=1m. Figure 6.5 shows the percentages of the haz-

ard region for two different models: TM-A1 and TM-B. The signal-to-noise ratio used for the simulations is $C/N_0 = 47$ dB.

For both TM-A1 and TM-B were considered the same areas as for the single band receiver. The plots show that, for TM-A1, the criterion is minimized for $\Delta \geq 0.16T_c$ for $N \geq 4$. On the other hand, for TM-B, the optimal region is given by $\Delta \geq 0.2T_c$ and $N \geq 4$. It is no surprise that the optimal regions are the same as for the single band receiver given that both these receivers use the same signal (BPSK(10)).

The remaining threat model (TM-C1) was not studied due to being a combination of TM-A1 with TM-B. The threat models TM-A2 and TM-C2 are not considered because, as explained in chapter 4, the BPSK(10) signal doesn't have subcarriers.

The optimal regions obtained for each threat model are described in table 6.3. The common region for all the threat models, $N \geq 4$ and $\Delta \geq 0.2T_c$ is also presented. This is the region of interest when choosing the number of pair of correlators, N, and the spacing, Δ. This analysis shows that there is no improvement in using a number of pair of correlators larger than 4. Hence, we adopt the value $N = 4$ and $\Delta = 0.2T_c$ for all the simulations presented for the signal E5a+E5b.

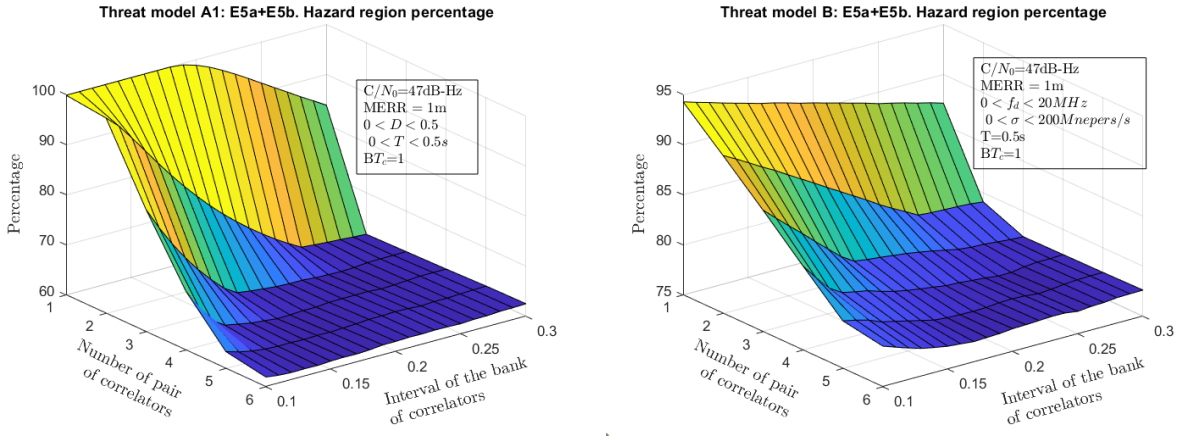

(a) Threat model TM-A1.

(b) Threat model TM-B.

Figure 6.5: Percentages of the hazard region for two threat models. Signal: E5a/E5b.

Table 6.3: Optimal region for N and Δ. Signal: E5a+E5b.

	N	Δ/T_c
TM-A1	[4,6]	[0.16,0.3]
TM-B	[4,6]	[0.2,0.3]
Union	[4,6]	[0.2,0.3]

Table 6.4 summarizes the parameters used for each one of the receivers.

6.2 Simulation Results

The simulations are divided in three groups according to the type of EWF distortion: TM-A, TM-B and TM-C. This division allows for an easy comparison between the performance of each processing

Table 6.4: Simulation Parameters for each processing option.

	N	Δ/T_c	BT_c
E5	4	0.17	2.5
E5a/E5b	4	0.2	1
E5a+E5b	4	0.2	1

option.

6.2.1 Threat Model A

In the presence of EWF anomaly the solution of the code discriminator is affected by an error, as shown in Fig. 6.6. The tracking errors present a linear region. The code discriminator error solely due to the TM-A1 anomaly for the signal E5a+E5b is not presented as it is the same as the error of the signal E5a/E5b (both were considered to use a BPSK(10) signal).

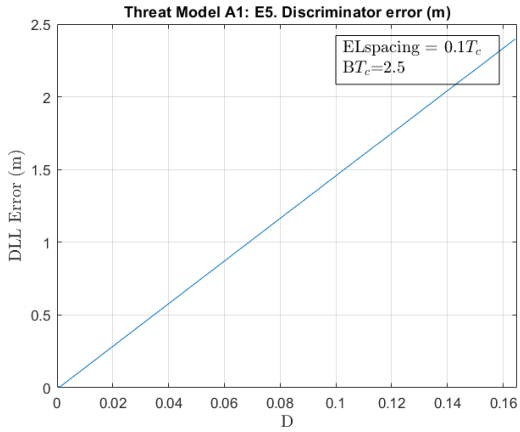

(a) Threat model TM-A1: E5.

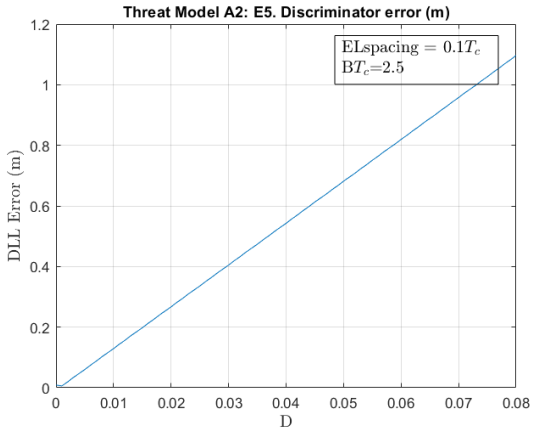

(b) Threat model TM-A2: E5.

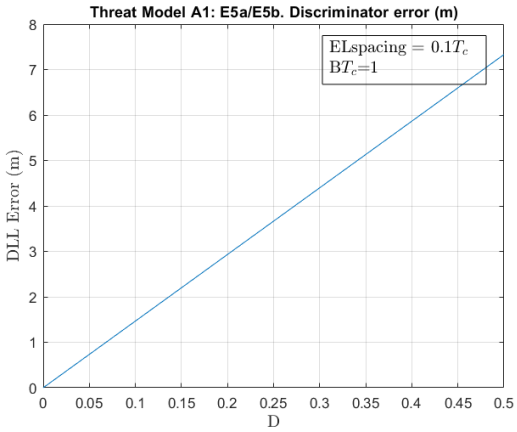

(c) Threat model TM-A1: E5a/E5b.

Figure 6.6: Code discriminator errors in the presence of TM-A distortion.

Figure 6.7 displays the detectability region for TM-A1 and TM-A2 with E5 signal versus parameters D and T. It can be recognized that, in both graphs, there is a large area for which the anomaly is

not detected (with $T \leq 0.5$ s). A solution to this problem would be increasing the time of correlation. However, by increasing the time of correlation, the system would become slower. Besides, there are some other effects such as the variation of the Doppler shift that would prevent using large correlation times [2].

It is also interesting to note that the threat model A2 is much more disruptive than the threat model A1. While the SQM was only able to detect the presence of a TM-A1 anomaly for $D \approx 0.08$ (for $T = 0.5$ s), the presence of a TM-A2 anomaly was detected for $D_s \approx 0.04$ (for $T = 0.5$ s).

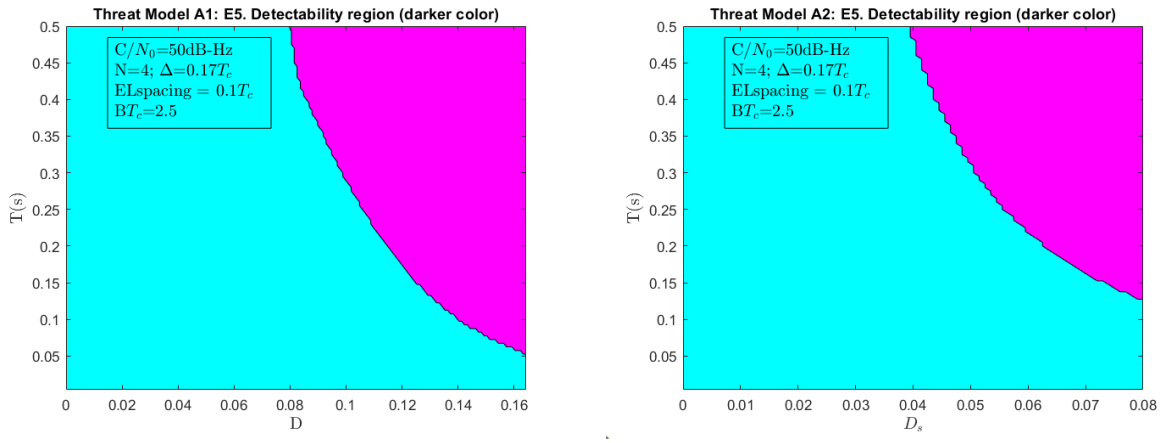

(a) Threat model TM-A1: E5.

(b) Threat model TM-A2: E5.

Figure 6.7: Detectability regions for threat models A1 and A2 with E5 signal.

Figure 6.8 shows the corresponding hazard regions for MERR=1m. Despite the TM-A1 anomalies with $D < 0.07$ not being detected for any of the plotted correlation times, it can be seen that they are outside of the hazard region. This is because the code discriminator error is less than MERR. The hazard region for TM-A2 is really small showing that the SQM works very well for this type of anomaly.

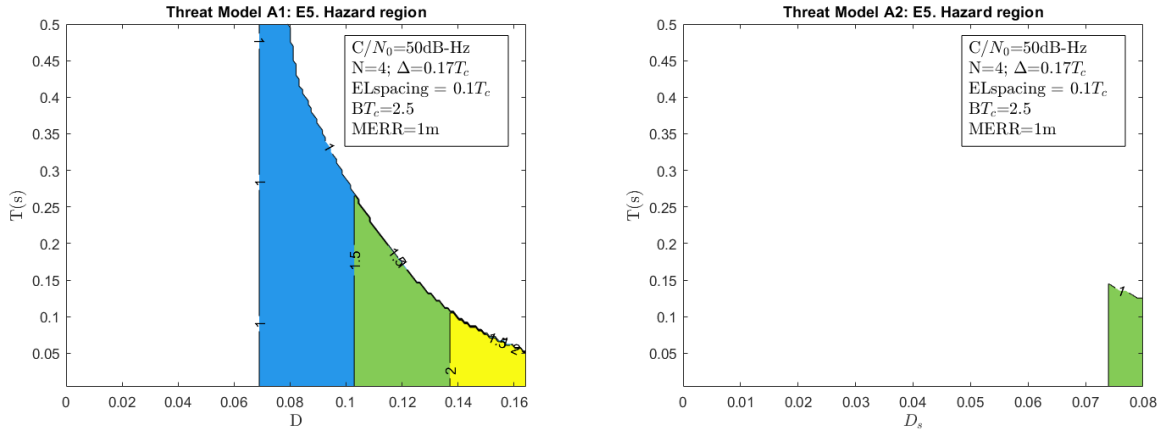

(a) Threat model TM-A1: E5.

(b) Threat model TM-A2: E5.

Figure 6.8: Hazard regions for threat models A1 and A2 with E5 signal.

Figure 6.9 displays the detectability regions for TM-A1 with E5a/E5b and E5a+E5b signals. The plots are very similar and exhibit worse results than the E5 case. Only for $D > 0.275$ is the anomaly detected with the signal E5a/E5b (for $T = 0.5$ s) and $D > 0.255$ with the signal E5a+E5b. By comparing both

images, we can conclude that the improvement in using both sub-bands instead of one is really shallow. The improvement that would come from using two times the number of tests is mitigated by the need to readjust the thresholds to maintain the probability of false alarm.

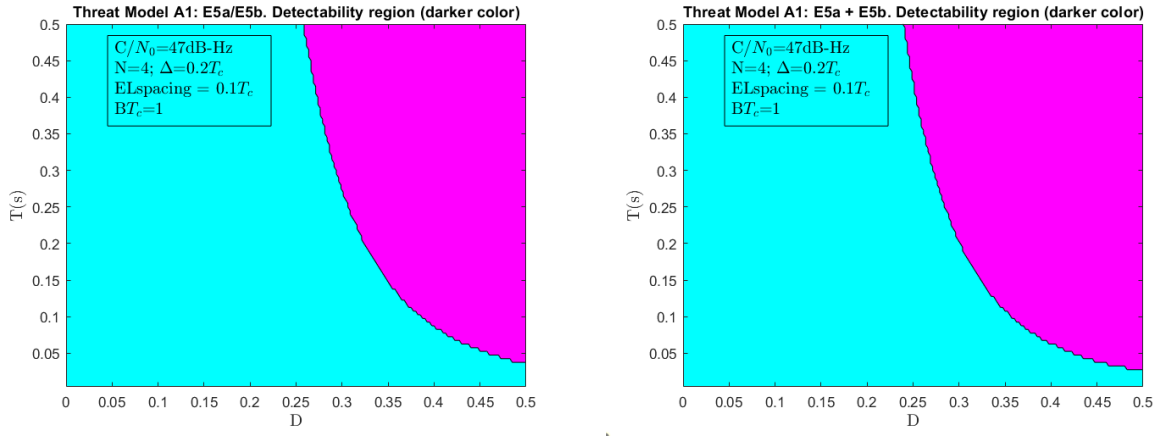

(a) Threat model TM-A1: E5a/E5b.

(b) Threat model TM-A1: E5a+E5b.

Figure 6.9: Detectability regions for threat models A1 with E5a/E5b and E5a+E5b signals.

In fact, Fig. 6.10 shows that by using both sub-bands there is a gain of approximately 1.2 dB when compared to using only one. Note that this gain is independent of the delay. Besides, notice how the probability of missed detection decays asymptotically with C/N_0 as the channel is Gaussian.

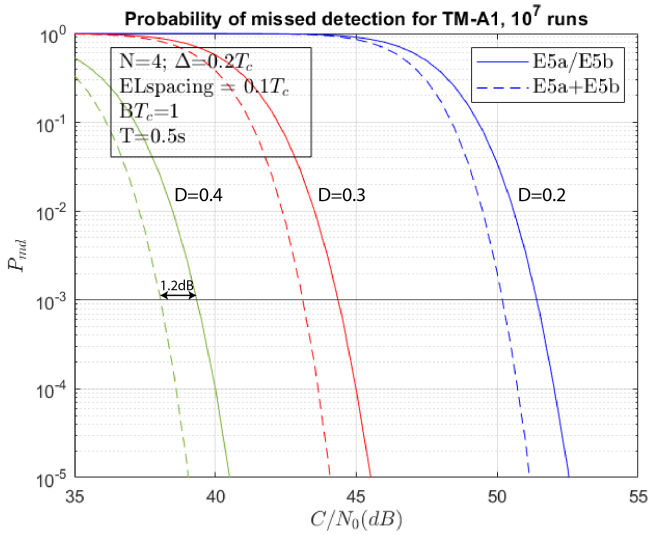

Figure 6.10: Probability of missed detection for TM-A1 with different delays for E5a/E5b and E5a+E5b signals.

Figure 6.11 shows the corresponding hazard regions for MERR=1m. Comparing these results with Fig. 6.8 we come to the conclusion that both receivers using sub-bands have much worse results than the receiver using the whole E5 signal.

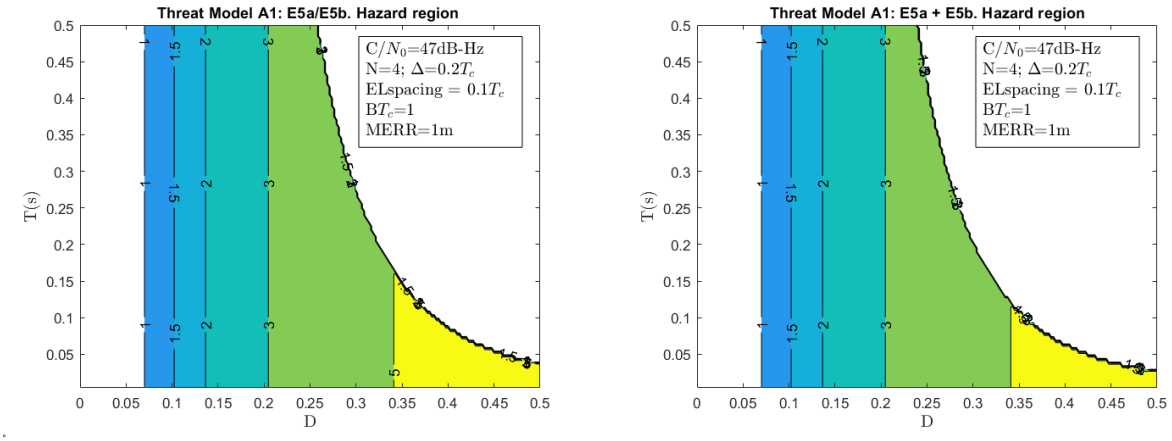

(a) Threat model TM-A1: E5a/E5b.

(b) Threat model TM-A1: E5a+E5b.

Figure 6.11: Hazard regions for threat models A1 with E5a/E5b and E5a+E5b signals.

6.2.2 Threat Model B

The code discriminator errors obtained with threat model B are shown in Fig. 6.12. The TS considered is $0 < f_d < 65$ MHz and $0 < \sigma < 400$ Mnepers/s.

In general, the errors increase as f_d and σ approach simultaneously zero, yielding errors larger than 30 m. On top of that, when both variables tend to zero, exists a really large correlation loss which will most likely result in signal tracking loss [18]. The code discriminator error for the signal E5a+E5b is not presented as it is the same as the error of the signal E5a/E5b concerning solely the errors induced by the distortion of the signal (both were considered to use a BPSK(10) signal).

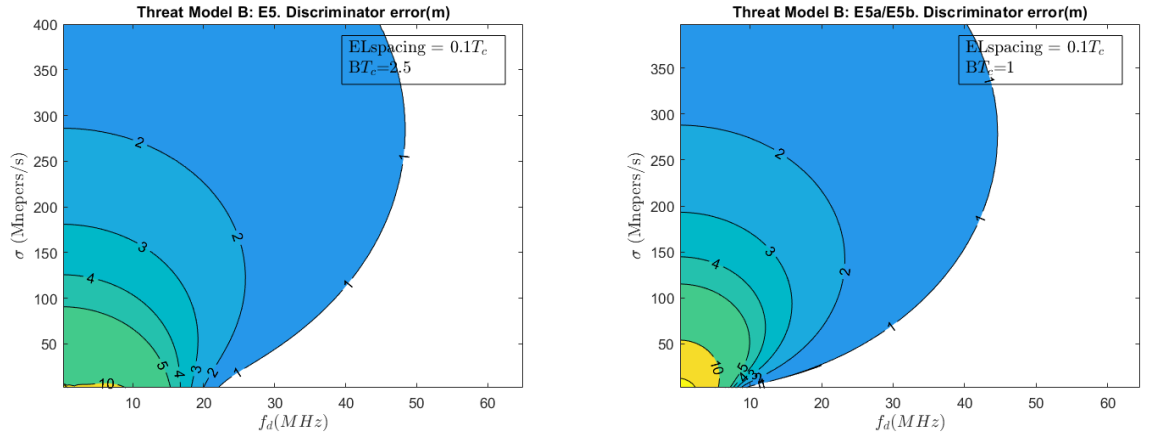

(a) Threat model TM-B: E5.

(b) Threat model TM-B: E5a/E5b.

Figure 6.12: Code discriminator errors in the presence of TM-B distortion.

Figure 6.13 presents the detectability region for TM-B with E5, E5a/E5b and E5a+E5b signals. The correlation time was set to $T = 0.5$ s in all simulations. It is clear that the signal E5 yields much better results than the remaining two signals. The E5a/E5b and E5a+E5b signals have a very similar performance.

Note that, although the discriminator errors indicated in Fig 6.12 exceed one meter, the correspond-

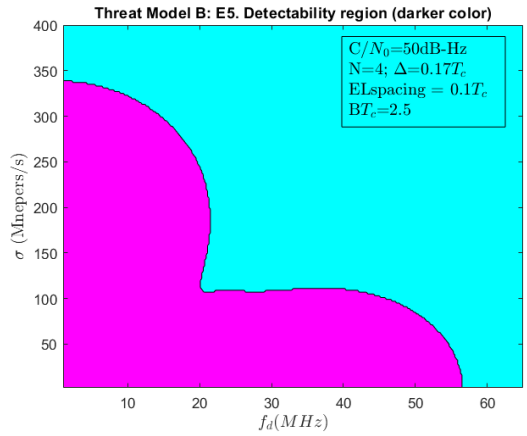

(a) Threat model TM-B: E5.

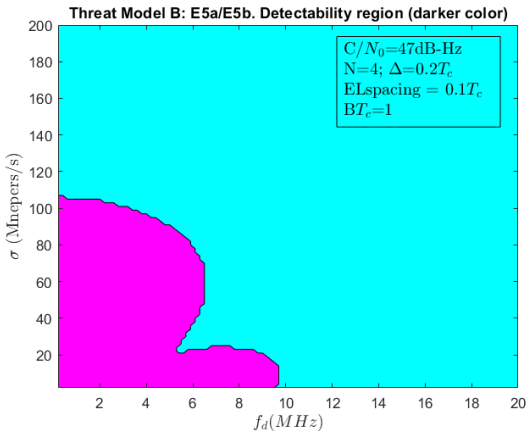

(b) Threat model TM-B: E5a/E5b.

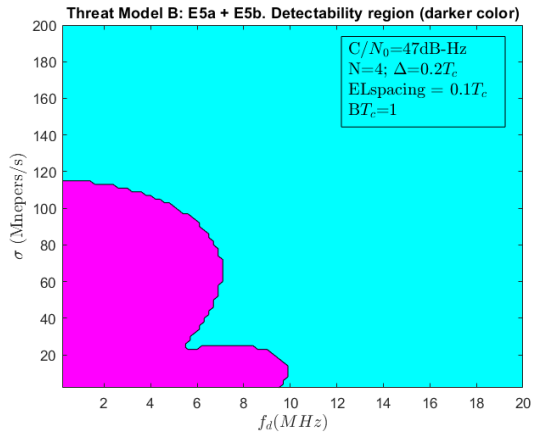

(c) Threat model TM-B: E5a+E5b.

Figure 6.13: Detectability regions for threat model B with E5, E5a/E5b and E5a+E5b signals.

ing EWF anomalies can be detected in some regions of the TS, as illustrated in Fig. 6.13. Thus, the hazard regions will be subsets of the plots of Fig. 6.12.

Figure 6.14 presents the hazard region for TM-B with E5, E5a/E5b and E5a+E5b signals. For E5a/E5b and E5a+E5b signals, the code tracking error in the hazard region may reach values above 5m. On the other hand, the worst code tracking error for the E5 signal is about 2m.

6.2.3 Threat Model C

The threat model C includes the analog and digital EWF anomalies. Therefore, it is expectable that the effects of the two types of distortions are added. Fig. 6.15 shows the code discriminator errors. We have considered a delay $\Delta = \Delta_s = 0.03T_c$ for the E5 signal with TM-C1/TM-C2, respectively. For the sub-band signals, we used a delay $\Delta = 0.2T_c$ with TM-C1. Ideally, we would want to use the same delay for both signals in order to compare them. However, as it was seen previously, the E5 signal is much more sensible to the distortions. Thus, we need to employ a different scale of anomalies to obtain noticeable results in each case.

Analyzing Fig. 6.15 we conclude that there isn't much difference between the code discriminator error

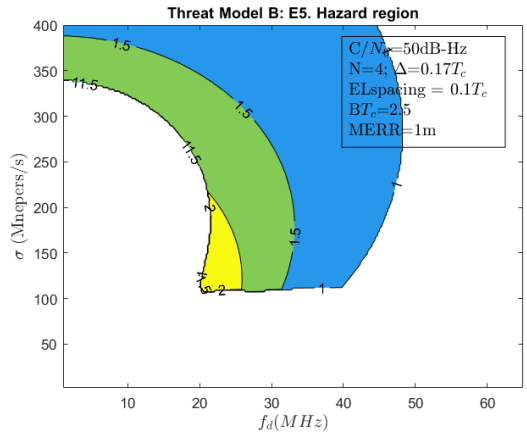

(a) Threat model TM-B: E5.

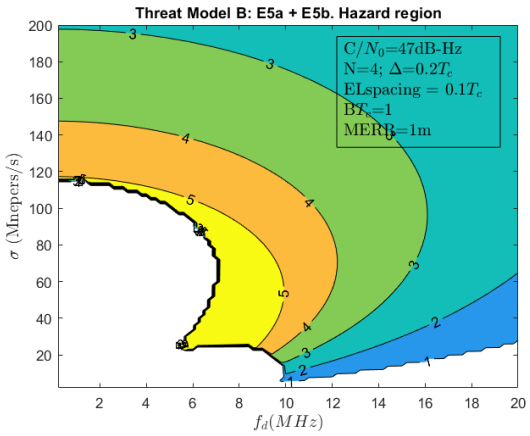

(b) Threat model TM-B: E5a/E5b.

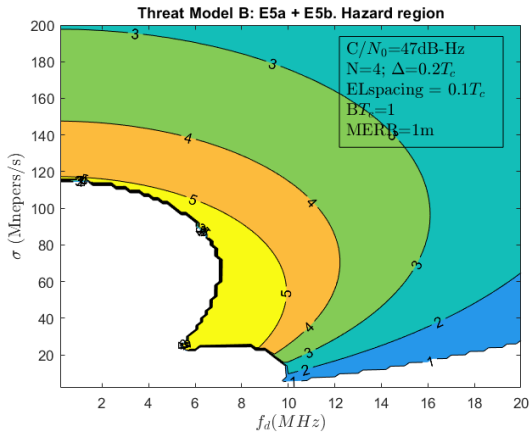

(c) Threat model TM-B: E5a+E5b.

Figure 6.14: Hazard regions for threat model B with E5, E5a/E5b and E5a+E5b signals.

for TM-C1 and TM-C2. This result was to be expected when taking into account the results obtained for TM-A1 and TM-A2 in Fig. 6.6. It was seen that for the same delay, both these threat models present similar code discriminator error. It is also evident that the errors for the sub-band signals are larger than for the E5 signal. This has to do, not only, with the poorer performance of the sub-band signals but also due to the larger delay chosen. Finally, comparing Fig. 6.15 with Fig. 6.12 we see the errors become larger as a result of the digital failure.

Figure 6.16 displays the detectability region for TM-C1 and TM-C2 with E5 signal. Comparing Fig. 6.16 with Fig. 6.13, it can be concluded that the regions of detectability of TM-B are approximately equal or are contained in the regions of TM-C. The expansion of the detectability region is carried out only in the σ-axis. This result suggests that, even though for TM-B the tests are insensitive to large values of σ, the detection of anomalies is due, essentially, to the digital component introduced by the TM-A.

Figure 6.17 shows the corresponding hazard regions for MERR=1m. Despite the reduction of the hazard region when compared to Fig 6.14 (TM-B), the code tracking errors are larger. This has to do with the addition of the digital EWF distortion. On one hand, the addition of the digital anomaly increases the detectability region. On the other hand, it also increases the code discriminator errors.

Figure 6.18 displays the detectability regions for TM-C1 with E5a/E5b and E5a+E5b signals. The

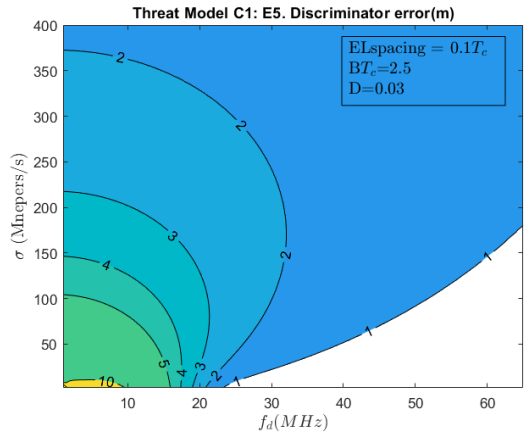

(a) Threat model TM-C1: E5.

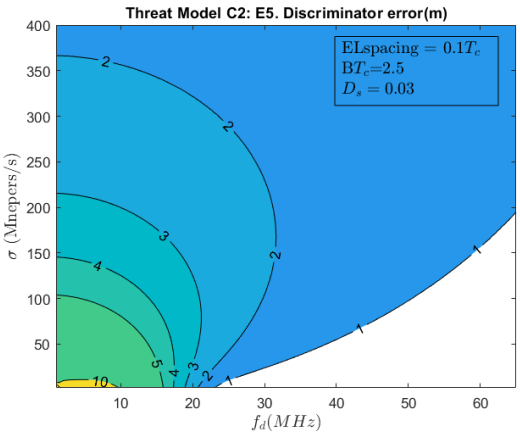

(b) Threat model TM-C2: E5.

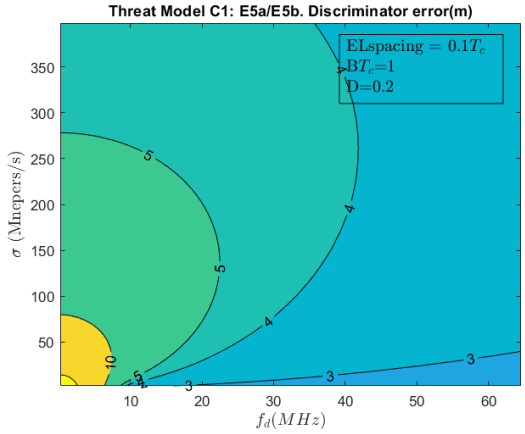

(c) Threat model TM-C1: E5a/E5b.

Figure 6.15: Code discriminator errors in the presence of TM-C distortion.

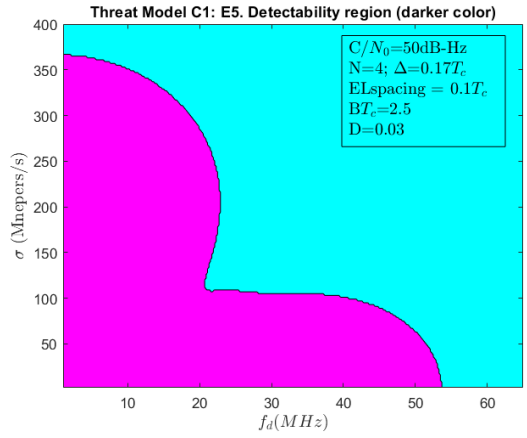

(a) Threat model TM-C1: E5.

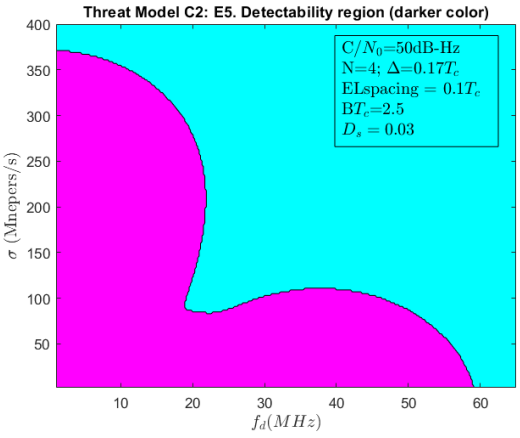

(b) Threat model TM-C2: E5.

Figure 6.16: Detectability regions for threat models C1 and C2 with E5 signal.

plots exhibit worse results than the E5 case. Contrarily to what was seen for the TM-B, the difference in performance between E5a/E5b and E5a+E5b is more evident. Namely, this difference occurs in the σ-axis. This result can be explained when taking into consideration the better performance registered for E5a+E5b with TM-A1.

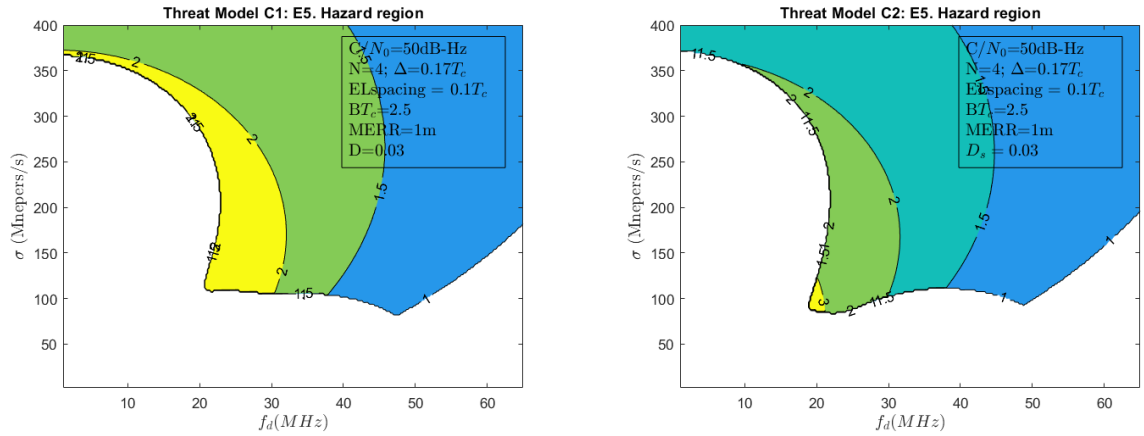

(a) Threat model TM-C1: E5.

(b) Threat model TM-C2: E5.

Figure 6.17: Hazard region for threat models C1 and C2 with E5 signal.

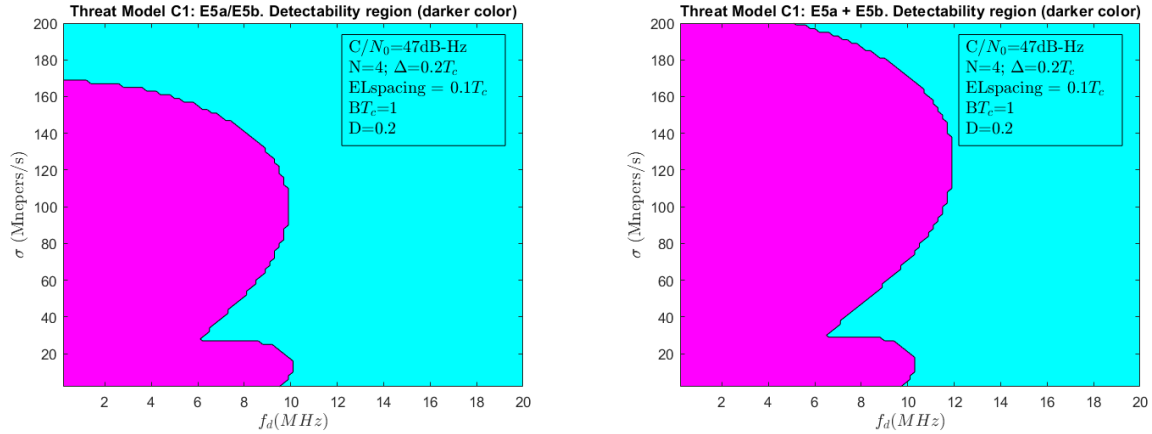

(a) Threat model TM-C1: E5a/E5b.

(b) Threat model TM-C: E5a+E5b.

Figure 6.18: Detectability regions for threat models C1 with E5a/E5b and E5a+E5b signals.

Figure 6.19 shows the corresponding hazard regions for MERR=1m. Comparing these results with Fig. 6.17 we come to the conclusion that both receivers using sub-bands have much worse results than the receiver using the whole E5 signal. Not only do they have a larger hazard region, but also larger code discriminator errors. Note that in Fig. 6.17 a) the sub region of the TS with $0 < fd < 20$ MHz and $0 < \sigma < 200$ Mnepers/s is a hazard-free region.

Figure 6.20 presents the detectability regions for TM-C1 with E5, E5a/E5b and E5a+E5b signals with lower C/N_0. We can see that the region of detectability diminishes significantly when the signal-to-noise ratio decreases. In fact, it was concluded that the important parameter to be considered in the performance analysis is the product $(C/N_0)T$. This means that, in order to maintain the same level of performance, for smaller values of C/N_0, larger integration intervals are required. This result corroborates the conclusions made in [19]. The corresponding hazard region plots are shown in Fig. 6.21. As expected, the code discriminator errors inside the hazard region are much larger. Comparing the plots of Fig. 6.17 a) and Fig. 6.21 a) we can also conclude that the area of the hazard region for the same TS increases as the product $(C/N_0)T$ diminishes.

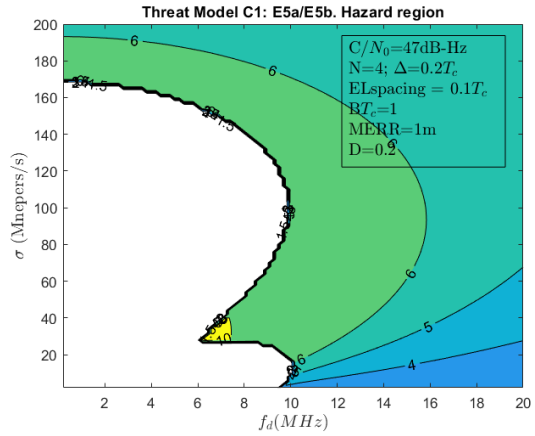

(a) Threat model TM-C1: E5a/E5b.

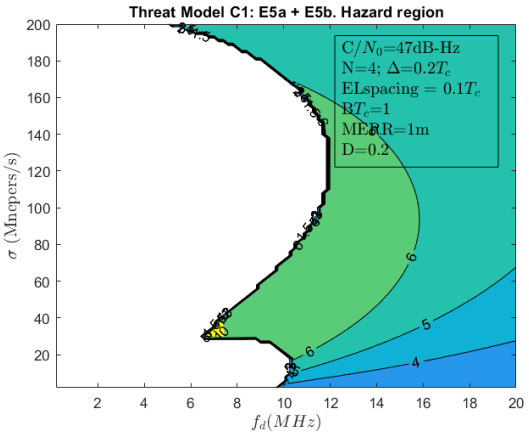

(b) Threat model TM-C1: E5a+E5b.

Figure 6.19: Hazard regions for threat models C1 with E5a/E5b and E5a+E5b signals.

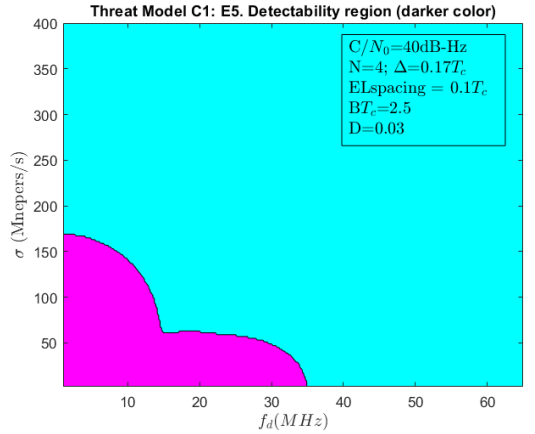

(a) Threat model TM-C1: E5.

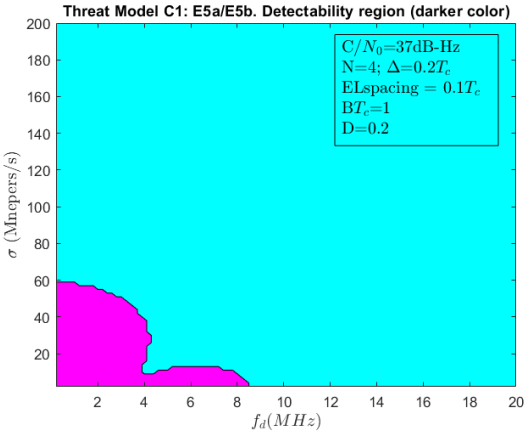

(b) Threat model TM-C1: E5a/E5b.

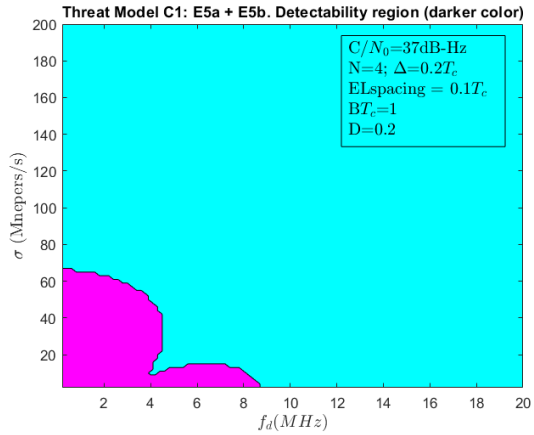

(c) Threat model TM-C1: E5a+E5b.

Figure 6.20: Detectability regions for threat model C1 with E5, E5a/E5b and E5a+E5b signals with lower $\mathrm{C/N_0}$.

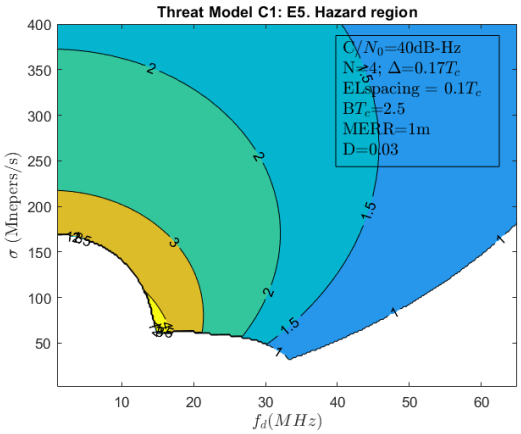

(a) Threat model TM-C1: E5.

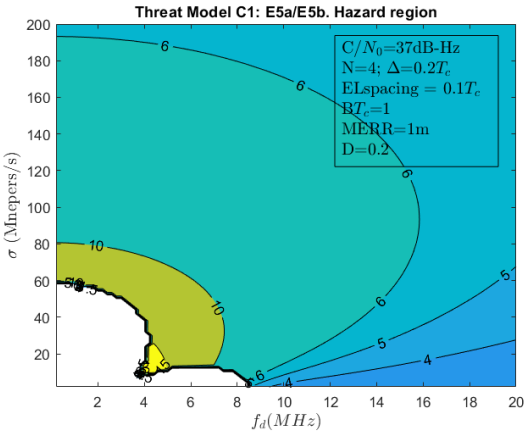

(b) Threat model TM-C1: E5a/E5b.

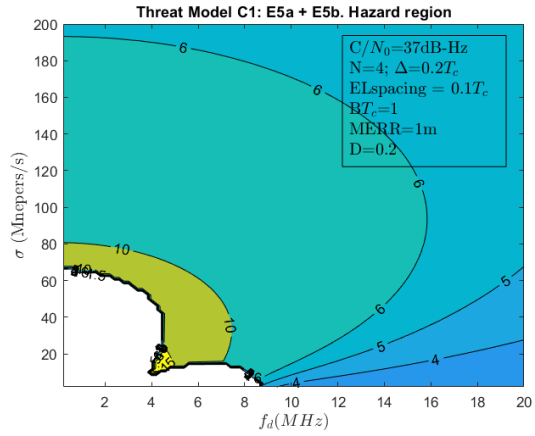

(c) Threat model TM-C1: E5a+E5b.

Figure 6.21: Hazard regions for threat model C1 with E5, E5a/E5b and E5a+E5b signals with lower C/N_0.

Chapter 7

Conclusions

This chapter presents in section 7.1 the conclusions drawn from the present dissertation and, in section 7.2, future work recommendations.

7.1 Achievements

The main objective of this work, as stated in chapter 1, was to establish a comparison of the performance between the SQM techniques using each processing option for the AltBOC signal: (i) process the entire signal; (ii) process both sub-bands, but separately; (iii) process only one of the sub-bands.

In chapter 2, an introduction to the Galileo E5 AltBOC signal was conducted, describing how the AltBOC modulation can be derived from the BOC modulation and listing the characteristics of the signal.

Given the complexity of the AltBOC signal, there are different processing options that lead to different types of receivers. In chapter 3, these different receivers were described, highlighting the advantages and drawbacks of each one. Furthermore, the autocorrelation functions of the pilot signals used for tracking were computed. These expressions were especially useful when defining the threat models in chapter 4. It was noted that for the single band receiver, the tracking technique is similar to the tracking of a BPSK(10) signal making it the simplest receiver model. Contrarily, the coherent dual band receiver is the most complex receiver model because it takes advantage of the whole AltBOC signal, leading to the best performance.

In chapter 4, the expressions of the threat models for the AltBOC modulation were developed. These threat models were based on the 2OS model presented in the literature and adopted by ICAO for GPS/GLONASS C/A code signal. These expressions correspond to the crosscorrelation between the incoming distorted pilot signal and the pilot signal replica generated in the receiver. Taking into consideration the receiver models presented in chapter 3, it was necessary to make a distinction between processing the whole AltBOC signal or a sub-band. Therefore, both the BPSK(10) and AltBOC(15,10) signals were considered.

In chapter 5, the SQM technique based on the multicorrelator architecture was presented. It was seen that this technique consisted in combining measurements estimated from the correlator outputs in

order to form metrics that are compared to their nominal values. The metrics presented were the simple ratio metric, difference ratio metric and sum ratio metric. A statistical analysis of each one of the metrics was conducted. These analysis were of paramount importance to define thresholds for each test in order to comply with the desired probability of false alarm.

Chapter 6 aimed on applying the tests and metrics introduced in chapter 5 to detect the EWFs described by the threat models developed in chapter 4. As stated previously, one of the main objectives of this work was to establish a comparison between the performance of the SQM using three different processing options, each one with different characteristics. Thus, in section 6.1, some SQM architecture aspects for the different receiver options were covered, namely, the thresholds for the tests, the number of pair of correlators and its spacing. While the thresholds for the tests were defined using the expressions developed in chapter 5 for an overall probability of false alarm $P_{FA} = 1.5 \times 10^{-7}$, the number of pair of correlators and its spacing were obtained through simulation. For each processing option, several simulations were performed using a different number of pairs of correlators and spacing. The optimal regions for these quantities were found by minimizing the hazardous region. It was seen that, regardless of the type of anomaly or processing option, a number of pair of correlators greater than 4 led to no major improvement of the hazardous region. This result allowed us to greatly reduce the complexity of the bank of correlators. Section 6.2 presents the results of the signal quality monitoring for each processing option. These results were displayed as the detectability region and the hazard region for MERR=1m. The goal was to achieve the probability of EWF missed detection $P_{md} < 10^{-3}$. It was clear that, regardless of the type of anomaly, processing the entire AltBOC signal outperformed every other signal processing option. Processing both sub-bands, but separately, performed better than processing only one of the sub-bands, although not by much.

Another important conclusion is that the correlation time needed to obtain substantial regions of detectability is large. This may present a problem in applications that require a really low latency time (such as aviation or autonomous vehicles). In fact, it was concluded that the regions of detectability tend to increase with the growth of the product $(C/N_0)T$. Thus, for scenarios where the signal-to-noise ratio is really low, the correlation time must be larger to maintain the same level of performance (at the cost of longer latency times).

Finally, it was verified that the signal distortions introduced by the satellite anomalies are similar to the ones introduced by multipath. Therefore, it is expected that for a mobile receiver affected by multipath, the probability of false alarm greatly increases. A possible solution for this problem would be to use fixed stations with highly directive antennas to detect EWF anomalies and broadcasting the SQM status of each satellite to the mobile receiver. The drawbacks of this solution would be to have an additional equipment to broadcast the SQM status of each satellite and the delays induced by the station-to-receiver link.

7.2 Future Work

There are several paths for improving the work presented in this dissertation. Some of the most relevant ones are now highlighted:

- **Implementation of DLL, PLL and C/N_0 estimator**: In this work it was assumed a perfect DLL and PLL. Furthermore, it was assumed that the signal-to-noise ratio (used to define the tests' thresholds) is known or at least correctly estimated. The inclusion of these blocks would allow for more realistic simulation results.

- **Testing other threat models**: Even if the threat models herein described are very useful concepts, they do not represent all signal distortions that could appear on a GNSS signal. Therefore, other threat models could be investigated and tested.

- **Testing in presence of multipath**: Testing the SQM techniques in multipath scenarios can be very useful especially when considering its applicability to mobile receivers. Multipath has similar effects on the correlation functions as EWFs. Therefore, it is expected that the probability of false alarm increases in its presence. An interesting topic of study would be to assess the effect of multipath in SQM of EWFs for different modulations (not only AltBOC). Besides, the application of the techniques used to mitigate the multipath effect, which includes code discriminators based on multicorrelator architectures, could be beneficial in the presence of EWF anomalies.

- **Testing other EWF detection techniques**: The proposed EWF detection techniques could be complemented with other detection algorithms, such as the Receiver Autonomous Integrity Monitoring (RAIM).

- **Testing a non-uniform correlator spacing**: The proposed multicorrelator architecture used an uniform spacing. It would be interesting to study if there is any optimal position for the correlators without forcing them to be uniformly spaced.

Bibliography

[1] E. Kaplan and C. Hegarty. *Understanding GPS. Principles and Applications*. Artech House, second edition, 2006.

[2] J. W. Betz. *Engineering Satellite-Based Navigation and Timing: Global Navigation Satellite Systems, Signals, and Receivers*. John Wiley & Sons, 2016.

[3] M. J. B. Pagot. *Modeling and Monitoring of New GNSS Signal Distortions in the Context of Civil Aviation*. PhD thesis, Université de Toulouse, 2016.

[4] S. Stephenson. *Automotive Applications of High Precision GNSS*. PhD thesis, University of Nottingham, December 2016.

[5] N. Joubert, T. Reid, and F. Noble. Developments in Modern GNSS and Its Impact on Autonomous Vehicle Architectures. In *2020 IEEE Intelligent Vehicles Symposium (IV)*, pages 2029–2036, 2020.

[6] A. Negrinho, P. Fernandes, P. Boto, F. Nunes, and F. Sousa. Evil Waveforms Detection Solutions for Autonomous Navigation Integrity. In *Proceedings of the 34th International Technical Meeting of the Satellite Division of The Institute of Navigation (ION GNSS+ 2021)*, pages 4097 – 4115, St. Louis, Missouri, September 2021.

[7] C. Edgar, F. Czopek, and B. Barker. A Co-operative Anomaly Resolution on PRN-19. In *Proceedings of the 12th International Technical Meeting of the Satellite Division of The Institute of Navigation (ION GPS 1999)*, pages 2269–2268, Nashville, TN, September 1999.

[8] K. W. Shallberg, S. D. Ericson, E. Phelts, T. Walter, K. Kovach, and E. Altshuler. Catalog and Description of GPS and WAAS L1 C/A Signal Deformation Events. In *Proceedings of the 2017 International Technical Meeting of The Institute of Navigation*, pages 508–520, Monterey, California, January 2017.

[9] P. Enge, E. Phelts, and A. Mitelman. Detecting Anomalous signals from GPS Satellites. *ICAO, GNSS/P, France*, 1999.

[10] *ICAO Convention - Annex 10: Aeronautical Telecommunications - Volume 1: Radio Navigation Aids*. ICAO, sixth edition, July 2006.

[11] C. Sun, H. Zhao, W. Feng, and C. Zhuang. A Novel Digital Threat Model and Effect Analysis on Modernized BeiDou Signals. In *Proceedings of the 2016 International Technical Meeting of The Institute of Navigation*, pages 401 – 413, Monterey, California, January 2016.

[12] J. B. Pagot, P. Thevenon, O. Julien, F. Amarillo-Fernandez, and D. Maillard. Threat Models Design for New GNSS Signals. In *Proceedings of the 2016 International Technical Meeting of The Institute of Navigation*, pages 970 – 982, Monterey, California, January 2016.

[13] F. Nunes and F. Sousa. Analysis of Threat Models. MONINT project: ESA/GMV/IT, December 2020.

[14] D. Fontanella, M. Paonni, and B. Eissfeller. A novel evil waveforms threat model for new generation GNSS signals: Theoretical analysis and performance. In *2010 5th ESA Workshop on Satellite Navigation Technologies and European Workshop on GNSS Signals and Signal Processing (NAVITEC)*, pages 1–8, 2010.

[15] C. Zhuang, H. Zhao, C. Sun, and W. Feng. Detection and Classification of GNSS Signal Distortions Based on Quadratic Discriminant Analysis. *IEEE Access*, 8:25221–25236, 2020. doi: 10.1109/ACCESS.2020.2965617.

[16] R. E. Phelts. *Multicorrelator Techniques for Robust Mitigation of Threats to GPS Signal Quality*. PhD thesis, Stanford University, 2001.

[17] J. B. Pagot, P. Thevenon, O. Julien, F. Amarillo-Fernandez, and D. Maillard. Signal Quality Monitoring for New GNSS Signals. In *Proceedings of the 29th International Technical Meeting of the Satellite Division of The Institute of Navigation (ION GNSS+ 2016)*, pages 1750 – 1763, Portland, Oregon, September 2016.

[18] I. Selmi, P. Thevenon, C. Macabiau, O. Julien, and M. Mabilleau. Signal Quality Monitoring Algorithm Applied to Galileo Signals for Large Evil Waveform Threat Space. In *Proceedings of the 2020 International Technical Meeting of The Institute of Navigation*, pages 352–365, San Diego, California, January 2020.

[19] F. Nunes and F. Sousa. Signal quality monitoring. MONINT project: ESA/GMV/IT, February 2021.

[20] *European GNSS (Galileo) Open Service: Signal-in-Space Interface Control Document*, January 2021. Issue 2.0.

[21] L. Lestarquit, G. Artaud, and J.-L. Issler. AltBOC for Dummies or Everything You Always Wanted To Know About AltBOC. In *Proceedings of the 21st International Technical Meeting of the Satellite Division of The Institute of Navigation (ION GNSS 2008)*, pages 961 – 970, Savannah, GA, September 2008.

[22] D. Margaria. *Analysis of Receiver Architectures, Acquisition Strategies and Multipath Mitigation Techniques for the E5 AltBOC Signal*. PhD thesis, Politecnico di Torino, 2007.

[23] L. Ries et al. New Investigations on Wideband GNSS2 Signals. In *Proceedings of the ION ENC GNSS 2003*, pages 147 – 155, Graz, Austria, April 2003.

[24] L. Ries et al. A Software Simulation Tool for GNSS2 BOC Signals Analysis. In *Proceedings of the 15th International Technical Meeting of the Satellite Division of The Institute of Navigation (ION GPS 2002)*, pages 2225 – 2239, Portland, OR, September 2002.

[25] J. Ángel Ávila Rodríguez. *On Generalized Signal Waveforms for Satellite Navigation*. PhD thesis, University FAF Munich, Germany, June 2008.

[26] F. Sousa and F. Nunes. New Expressions for the Autocorrelation Function of BOC GNSS Signals. *NAVIGATION, Journal of the Institute of Navigation*, 60(1):1 – 9, 2013.

[27] M. Soellner and P. Erhard. Comparison of AWGN Code Tracking Accuracy for Alternative-BOC, Complex-LOC and Complex-BOC Modulation Options in Galileo E5-Band. In *Proceedings of ION ENC GNSS 2003*, Graz, Austria, April 2003.

[28] N. C. Shivaramaiah. *Enhanced Receiver Techniques for Galileo E5 AltBOC Signal Processing*. PhD thesis, The University of New South Wales, June 2011.

[29] G. X. Gao, S. Datta-Barua, T. Walter, and P. Enge. Ionosphere Effects for Wideband GNSS Signals. In *Proceedings of the 63rd Annual Meeting of The Institute of Navigation (2007)*, pages 147 – 155, Cambridge, MA, April 2007.

[30] R. F. D. Nunes. Simplified AltBOC Receiver Performance Analysis. Master's thesis, Instituto Superior Técnico, 2016.

[31] N. C. Shivaramaiah, A. G. Dempster, and C. Rizos. Hybrid tracking loop architectures for the Galileo E5 signal. In *Proceedings of the European navigation conference on global navigation satellite systems ENC GNSS 2009, Napoli, Italy*, 2009.

[32] S. M. Kay. *Fundamentals of Statistical Signal Processing, Volume II: Detection Theory*. Prentice Hall, 1st edition, 1998.

[33] C. W. Therrien. *Discrete Random Signals and Statistical Signal Processing*. Prentice-Hall, 1992.

[34] A. Papoulis. *Probability, Random Variables, and Stochastic Processes*. McGraw-Hil, N. York, third edition, 1991.

[35] J. Hayya, D. Armstrong, and N. Gressis. A Note on the Ratio of Two Normally Distributed Variables. *Management Science*, 21(11):1338–1341, July 1975.

[36] M. Jeruchim, P. Balaban, and K. Shanmugan. *Simulation of Communication Systems. Modeling, Methodology and Techniques*. Kluwer, 2000.

[37] L. D. Brown, T. T. Cai, and A. DasGupta. Approximate is Better than "Exact" for Interval Estimation of Binomial Proportions. *Statistical Science*, 16(2):101–133, May 2001.

[38] A. Agresti and B. Coull. Approximate is Better than “Exact” for Interval Estimation of Binomial Proportions. *The American Statistician*, 52(2):119–126, May 1998.

Appendix A

Crosscorrelation between two rectangular pulses

In this annex will be computed the crosscorrelation between two rectangular pulses with different length and centre.

Consider two rectangular pulses

$$\Pi_{L_0}(x - x_0) = \begin{cases} 1, & |x - x_0| < L_0/2 \\ 0, & \text{otherwise} \end{cases} \tag{A.1}$$

$$\Pi_{L_1}(x - x_1) = \begin{cases} 1, & |x - x_1| < L_1/2 \\ 0, & \text{otherwise} \end{cases} \tag{A.2}$$

with $L_1 \geq L_0$. Fig. A.1 represents these two functions.

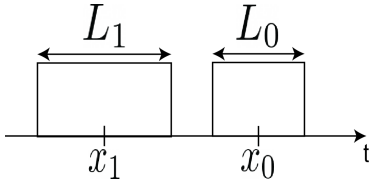

Figure A.1: Two rectangular pulses.

The crosscorrelation between the two pulses is given by

$$\begin{aligned} R(\tau) &= \int_{-\infty}^{+\infty} \Pi_{L_0}(x - x_0)\Pi_{L_1}(x - \tau - x_1)dx \\ &= \int_{x_0 - L_0/2}^{x_0 + L_0/2} \Pi_{L_1}(x - \tau - x_1)dx \end{aligned} \tag{A.3}$$

For $\tau < x_0 - x_1 - \frac{L_0 + L_1}{2}$ or $\tau > x_0 - x_1 + \frac{L_0 + L_1}{2}$ the integral is equal to 0.

On the other hand, for $x_0 - x_1 - \frac{L_1 - L_0}{2} < \tau < x_0 - x_1 + \frac{L_1 - L_0}{2}$ we have a maximum.

Thus, the crosscorrelation between two rectangular pulses with different centres and lengths is displayed in Fig. A.2.

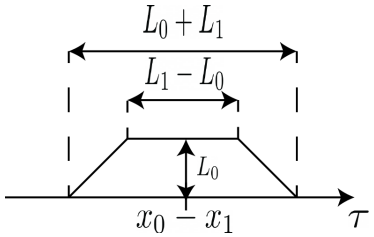

Figure A.2: crosscorrelation between two rectangular pulses.

This function, herein called $\Xi_{L_0,L_1}(\tau)$, can be written analytically as the difference between two triangular pulses

$$\Xi_{L_0,L_1}[\tau-(x_0-x_1)] = \frac{L_0+L_1}{2}\Lambda_{\frac{L_0+L_1}{2}}[\tau-(x_0-x_1)] - \frac{L_1-L_0}{2}\Lambda_{\frac{L_1-L_0}{2}}[\tau-(x_0-x_1)] \tag{A.4}$$

Consider now that the rectangular pulse $\Pi_{L_0}(x-x_0)$ is lowpass filtered by an ideal rectangular filter with a frequency response given by Eq. 4.9. Let $\Xi^F_{L_0,L_1}[\tau-(x_0-x_1)]$ be the filtered crosscorrelation function, using Eq. 4.8, we obtain

$$\begin{aligned}\Xi^F_{L_0,L_1}[\tau'-(x_0-x_1)] &= \int_{-B}^{B}\mathcal{F}\{\Xi_{L_0,L_1}[\tau-(x_0-x_1)]\}\exp(j2\pi f\tau')df \\ &= \int_{-B}^{B}\left[\frac{L_0+L_1}{2}\right]^2\operatorname{sinc}^2\left(f\frac{L_0+L_1}{2}\right)\cos[2\pi f(\tau'-(x_0-x_1))]df \\ &- \int_{-B}^{B}\left[\frac{L_1-L_0}{2}\right]^2\operatorname{sinc}^2\left(f\frac{L_1-L_0}{2}\right)\cos[2\pi f(\tau'-(x_0-x_1))]df\end{aligned} \tag{A.5}$$

Appendix B

Error model extension for Threat Model TM-A1 with AltBOC(15,10) signal

This appendix contains the extension of the error models presented in section 4.1.1.2 for the TM-A1 model with AltBOC(15,10) signal.

In Fig. B.1 is represented the typical waveform for TM-A1 real/imaginary part of AltBOC(15,10) signal for a delay $\Delta > T_c/12$ using the error model presented in Eq. 4.16.

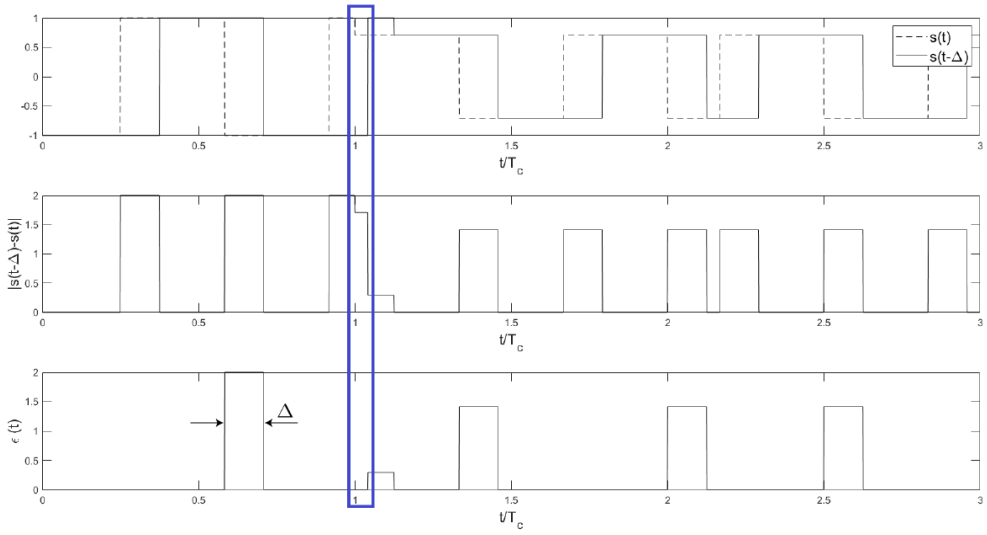

Figure B.1: Typical waveform for TM-A1 with real/imaginary part of AltBOC(15,10) signal and $|\Delta| > T_c/12$ using the model described in Eq. 4.16.

It can be seen that the previously presented error model doesn't introduce any correction in the area marked by the blue rectangle even though it should to comply with the physical model. For that reason,

it was necessary to develop an extension of such model in order to cover larger delays.

Consider now the following expression for the extended error model

$$\epsilon(t) = \epsilon_0(t) + \epsilon_1(t) \tag{B.1}$$

We can understand Eq. B.1 as a sum of error models, where $\epsilon_1(t)$ introduces corrections that weren't covered by $\epsilon_0(t)$.

$\epsilon_1(t)$ is given by Eq. 4.16 and

$$\begin{aligned}\epsilon_1(t) = &\frac{1}{2}\Re\{s(t - T_c/12) - \tilde{s}_1(t)\}[1 + \text{sign}\{\Re\{s(t - T_c/12) - \tilde{s}_1(t)\}\}] \\ &+ \frac{j}{2}\Im\{s(t - T_c/12) - \tilde{s}_1(t)\}[1 + \text{sign}\{\Im\{s(t - T_c/12) - \tilde{s}_1(t)\}\}]\end{aligned} \tag{B.2}$$

where $\tilde{s}_1(t)$ is the distorted signal containing the previous corrections given by $\tilde{s}_1(t) = s(t) + \epsilon_0(t)$.

This formulation allows us to extend the model up to $|\Delta| < T_c/6$.

Multiplying this new error term, $\epsilon_1(t)$, by the conjugate of the delayed version of the pilot signal and time-averaging

$$\begin{aligned}< \epsilon_1(t)\, s_p^*(t-\tau) > = &\frac{1}{2} < \Re\{s(t - T_c/12) - \tilde{s}_1(t)\} s_p^*(t-\tau) > \\ &+ \frac{1}{2} < |\Re\{s(t - T_c/12) - \tilde{s}_1(t)\}| s_p^*(t-\tau) > \\ &+ \frac{j}{2} < \Im\{s(t - T_c/12) - \tilde{s}_1(t)\} s_p^*(t-\tau) > + \frac{j}{2} < |\Im\{s(t - T_c/12) - \tilde{s}_1(t)\}| s_p^*(t-\tau) > \\ = &\frac{1}{2} < [s(t - T_c/12) - \tilde{s}_1(t)] s_p^*(t-\tau) > + \frac{1}{2} < |\Re\{s(t - T_c/12) - \tilde{s}_1(t)\}| s_p^*(t-\tau) > \\ &\frac{j}{2} < |\Im\{s(t - T_c/12) - \tilde{s}_1(t)\}| s_p^*(t-\tau) >\end{aligned} \tag{B.3}$$

Unlike what was stated previously for the case of $\epsilon_0(t)$ in section 4.1.1.2, the $\text{prob}\{\Re\{s(t - T_c/12) - \tilde{s}(t)\} > 0\} \neq \text{prob}\{\Re\{s(t - T_c/12) - \tilde{s}(t)\} < 0\}$ as well as $\text{prob}\{\Im\{s(t - T_c/12) - \tilde{s}(t)\} > 0\} \neq \text{prob}\{\Im\{s(t - T_c/12) - \tilde{s}(t)\} < 0\}$. One could study these probabilities and compute the cross-correlation functions taking them into account. However, herein, another approach was followed.

The signal $\epsilon_1(t)$ was evaluated for each one of the possible waveforms the AltBOC(15,10) signal can take. Assuming equal probable symbols, we were able to compute the complex cross-correlation functions between $\epsilon_1(t)$ and $s_p(t)$.

The AltBOC(15,10) signal is composed of 4 independent codes which means that there are 16 equiprobable different symbols. However, since the signal $\epsilon_1(t)$ is obtained using a delayed version of the AltBOC(15,10) signal, in order to study the transitions, we need not only to consider one symbol duration but two, making a total of $16^2 = 256$ waveforms.

Furthermore, it was seen previously in section 2.4 that the AltBOC(15,10) signal waveform also depends on time due to the sub-carrier phase.

We can then conclude that in order to fully characterize the $\epsilon_1(t)$ signal we need to take into consideration 512 waveforms. This is a rather tedious task. Fortunately, it can be simplified.

The purpose of defining the signal $\epsilon_1(t)$ is to correlate it with $s_p(t)$. Since the pilot signal only has the pilot bits, each symbol is composed by only 2 bits instead of 4. While there are 16 different symbols in the AltBOC(15,10) signal, there are only 4 in the pilot signal. This means that, for instance, the $\epsilon_1(t)$ waveforms corresponding to all these symbols: $[e_{AI}, e_{BI}, e_{AQ}, e_{BQ}] = [0,0,0,0]$, $[e_{AI}, e_{BI}, e_{AQ}, e_{BQ}] = [0,1,0,0]$, $[e_{AI}, e_{BI}, e_{AQ}, e_{BQ}] = [1,0,0,0]$ and $[e_{AI}, e_{BI}, e_{AQ}, e_{BQ}] = [1,1,0,0]$ correlate with the same pilot waveform (given by the symbol $[e_{AQ}, e_{BQ}] = [0,0]$). This allows us to sum up those waveforms of $\epsilon_1(t)$ for all those cases and compute only one cross-correlation.

As stated previously, the AltBOC(15,10) symbols can have two different waveforms depending on the phase of the subcarriers. However, it can be seen that these two waveforms are symmetric to each other (Fig. 4.5). This means that instead of correlating each $\epsilon_1(t)$ waveform with the corresponding pilot signal (with the same subcarrier phase), we can subtract those $\epsilon_1(t)$ corrections and correlate them with a single pilot signal.

Taking these properties into account we can significantly simplify the study of the $\epsilon_1(t)$ signal. With this simplification, to study every possible waveform we need to compute only 16 cross-correlations.

The corresponding waveforms, which for simplicity will be called ϵ_1^T, that are to be correlated with the pilot signal are represented in Fig. B.2. In the figure are also mentioned the pilot symbols corresponding to each one of the corrections.

Δ_1 is defined as

$$\Delta_1 = \begin{cases} \Delta - T_c/12, & T_c/12 < \Delta \leq T_c/6 \\ 0, & \text{otherwise} \end{cases} \tag{B.4}$$

To obtain the cross-correlation between $\epsilon_1(t)$ and $s_p(t)$ we need to compute the pilot signal for each possible combination of symbols using Eq. 3.2 and correlate it with the waveforms presented in Fig. B.2.

$$< \epsilon_1(t)\, s_p^*(t-\tau) >= \frac{1}{512} \sum_{s_0=00}^{11} \sum_{s_1=00}^{11} \frac{1}{T_c} \int_0^{T_c} \epsilon_1^T(t)|_{s_0,s_1} s_p^*(t-\tau)|_{s_0,s_1} dt \tag{B.5}$$

where $s_0 = [e_{AQ}(t) e_{BQ}(t)]_0$ represents the symbol at time slot 0 and $s_1 = [e_{AQ}(t) e_{BQ}(t)]_1$ at time slot 1.

Note now that the pilot signal can be written in terms of the subcarriers, which, in turn, can be computed as a sum of rectangular pulses (Eq. 2.16). Likewise, $\epsilon_1^T(t)$ depicted in Fig. B.2, is also a sum of rectangular pulses for each case. Thus, the cross-correlation between $\epsilon_1(t)$ and $s_p(t)$ is equal to the sum of cross-correlations between several rectangular pulses with different centre, length and height, which can be computed using the result presented in Appendix A.

Computing B.5 taking into account that both signals can be written as a sum of rectangles and grouping every common term, we obtain that

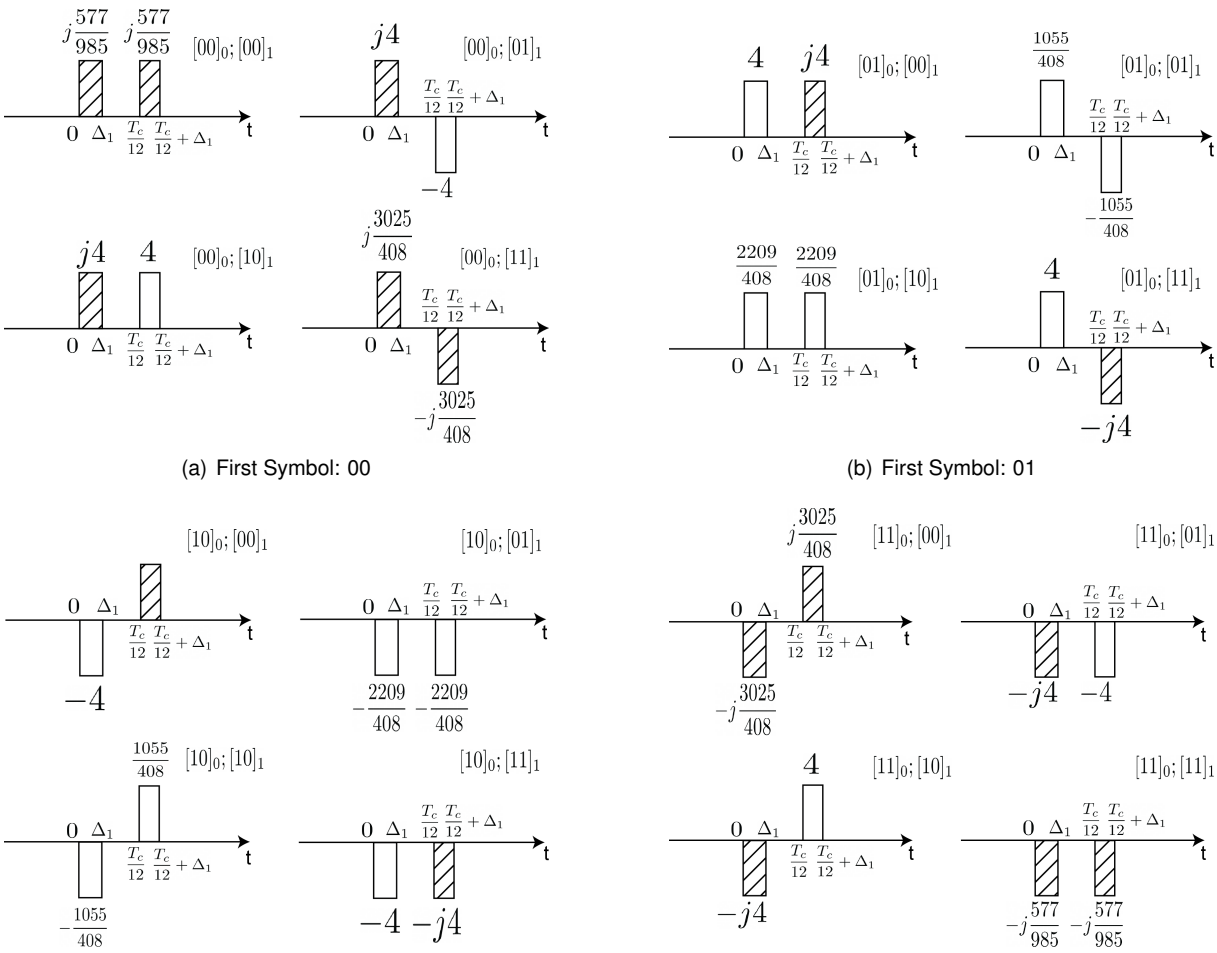

(a) First Symbol: 00

(b) First Symbol: 01

(c) First Symbol: 10

(d) First Symbol: 11

Figure B.2: Sum of the corrections employed by $\epsilon_1(t)$, $\epsilon_1^T(t)$, for each pilot signal symbol.

$$< \epsilon_1(t)\, s_p(t-\tau) >= \sum_{n=-11}^{13} \frac{\gamma_n}{T_c} \Xi_{\Delta_1, T_c/12}\left[\tau - \frac{T_c}{12}\left(n - \frac{1}{2} + 6D_2\right)\right] \tag{B.6}$$

with $\Xi_{L_0,L_1}[\tau-(x_0-x_1)]$ defined in Eq. A.4, $D_1 = \frac{\Delta_1}{T_c}$. The coefficients, $gamma_n$, are given by

Table B.1: Coefficients for the extended TM-A1 model.

n	-11	-10	-9	-8	-7	-6	-5	-4	-3	-2	-1	0	1
γ_n	$\frac{207}{10975}$	$-\frac{259}{3433}$	$-\frac{207}{2195}$	$-\frac{53}{915}$	$\frac{53}{4278}$	$\frac{259}{3433}$	$\frac{207}{2195}$	$\frac{53}{915}$	$-\frac{53}{4278}$	$-\frac{259}{3433}$	$-\frac{207}{2195}$	$-\frac{53}{915}$	$\frac{1}{16}$

n	2	3	4	5	6	7	8	9	10	11	12	13
γ_n	$-\frac{53}{915}$	$-\frac{207}{2195}$	$-\frac{259}{3433}$	$-\frac{53}{4278}$	$\frac{53}{915}$	$\frac{207}{2195}$	$\frac{259}{3433}$	$\frac{53}{4278}$	$-\frac{53}{915}$	$-\frac{207}{2195}$	$-\frac{259}{3433}$	$\frac{207}{10975}$

Finally, using 4.23 and B.6 we have for $\Delta < T_c/6$

$$R_{\tilde{s}s_p}(\tau) = \frac{1}{2}[R_{ss_p}(\tau) + R_{ss_p}(\tau-\Delta)] + \sum_{n=-11}^{13} \frac{\gamma_n}{T_c} \Xi_{\Delta_1, T_c/12}\left[\tau - \frac{T_c}{12}\left(n - \frac{1}{2} + 6D_2\right)\right] \tag{B.7}$$

Lastly, if the incoming distorted signal were to be low-pass filtered, as it is usual for real receivers, we would obtain using Eqs. 4.26,A.5:

$$
\begin{aligned}
R_A(\tau') = & \frac{B_1}{12}\int_{-BT_c}^{BT_c} \operatorname{sinc}^2\left(\frac{x}{6}\right)\cos\left(2\pi\frac{\tau'}{T_c}x\right)dx + \frac{B_1}{12}\int_{-BT_c}^{BT_c} \operatorname{sinc}^2\left(\frac{x}{6}\right)\cos\left(2\pi\left(\frac{\tau'}{T_c}-D\right)x\right)dx \\
& + \sum_{m=1}^{2}\frac{B_m}{6}\int_{-BT_c}^{BT_c} \operatorname{sinc}^2\left(\frac{x}{6}\right)\cos\left(2\pi\frac{mx}{3}\right)\cos\left(2\pi\frac{\tau'}{T_c}x\right)dx \\
& + \sum_{m=1}^{2}\frac{B_m}{6}\int_{-BT_c}^{BT_c} \operatorname{sinc}^2\left(\frac{x}{6}\right)\cos\left(2\pi\frac{mx}{3}\right)\cos\left(2\pi\left(\frac{\tau'}{T_c}-D\right)x\right)dx \\
& + \sum_{n=0}^{5}\frac{C_m}{12}\int_{-BT_c}^{BT_c} \operatorname{sinc}^2\left(\frac{x}{12}\right)\cos\left(2\pi\frac{(2n+1)x}{12}\right)\cos\left(2\pi\frac{\tau'}{T_c}x\right)dx \\
& + \sum_{m=1}^{2}\frac{C_m}{12}\int_{-BT_c}^{BT_c} \operatorname{sinc}^2\left(\frac{x}{12}\right)\cos\left(2\pi\frac{(2n+1)x}{12}\right)\cos\left(2\pi\left(\frac{\tau'}{T_c}-D\right)x\right)df \\
& + \sum_{n=-11}^{13}\int_{-BT_c}^{BT_c}\gamma_n\left[\frac{1}{24}+\frac{D_1}{2}\right]^2 \operatorname{sinc}^2\left(x\left[\frac{1}{24}+\frac{D_1}{2}\right]\right)\cos\left(2\pi\left[\frac{\tau'}{T_c}-\frac{1}{12}\left(n-\frac{1}{2}+6D_1\right)\right]x\right)dx \\
& - \sum_{n=-11}^{13}\int_{-BT_c}^{BT_c}\gamma_n\left[\frac{1}{24}-\frac{D_1}{2}\right]^2 \operatorname{sinc}^2\left(x\left[\frac{1}{24}-\frac{D_1}{2}\right]\right)\cos\left(2\pi\left[\frac{\tau'}{T_c}-\frac{1}{12}\left(n-\frac{1}{2}+6D_1\right)\right]x\right)dx
\end{aligned}
\tag{B.8}
$$

In Fig. B.3 is represented a graph that shows the difference on the cross-correlation function between the simple and the extended model for $BT_c = 1$.

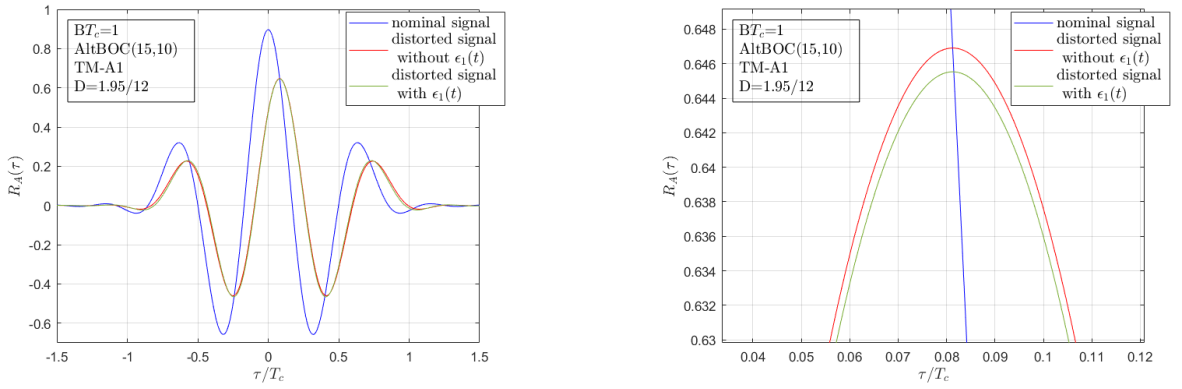

(a) Normal plot

(b) Zoomed plot

Figure B.3: Correlation Function for AltBOC signal with TM-A1 distortion, D=$\frac{1.95T_c}{12}$, with and without taking ϵ_1 into account.

Appendix C

Generation of random correlated Gaussian noise vectors

In the present thesis, it is required to generate vectors of correlated noise for use in the various simulations undertaken. This annex will address a method for generating those vectors. The method here presented is described in further detail in [19].

Consider the problem of generating a zero-mean Gaussian noise vector, U, with covariance matrix C using a zero-mean Gaussian Vector, W, with independent components of unity variance. Thus, the aim is to determine a certain matrix, G, that satisfies

$$U = GW \tag{C.1}$$

The covariance matrix, C, can be computed from

$$\begin{aligned} C = E\{UU^T\} &= E\{GWW^TG^T\} \\ &= GE\{WW^T\}G^T \\ &= GG^T \end{aligned} \tag{C.2}$$

According to [33], the covariance matrix can be written in terms of its eigenvalues and eigenvectors as

$$C = V\Lambda V^T \tag{C.3}$$

with V being a matrix whose columns are the eigenvectors of C and Λ is a diagonal matrix with the eigenvalues of C. Comparing Eq. C.2 and Eq. C.3 we obtain the expression for G:

$$G = V\Lambda^{1/2} = V\mathrm{diag}\{\sqrt{\lambda_1}, \sqrt{\lambda_2}, ..., \sqrt{\lambda_M}\} \tag{C.4}$$

Appendix D

Statistical analysis of Tests

In this appendix will be presented a statistical characterization of the tests proposed in section 5.2. This analysis is of extreme importance to define the thresholds for the tests to comply with the requirements for the probability of false alarm. This characterization is defined is further detail in [19].

Consider the following test $T = g(X, Y)$ defined as a function of two correlated gaussian random variables, $X \sim N(m_X, \sigma_X^2)$ and $Y \sim N(m_Y, \sigma_Y^2)$. According to [34], the mean, m_T and variance, σ_T^2, can be estimated in terms of the mean, variance, and covariance of X and Y:

$$m_T \approx g(m_X, m_Y) + \frac{1}{2}\left(\frac{\partial^2 g}{\partial x^2}\sigma_X^2 + 2\frac{\partial^2 g}{\partial x \partial y} r\sigma_X\sigma_Y + \frac{\partial^2 g}{\partial y^2}\sigma_Y^2\right) \tag{D.1}$$

$$\sigma_T^2 \approx \left(\frac{\partial g}{\partial x}\right)^2 \sigma_X^2 + 2\left(\frac{\partial g}{\partial x}\right)\left(\frac{\partial g}{\partial y}\right) r\sigma_X\sigma_Y + \left(\frac{\partial g}{\partial y}\right)^2 \sigma_Y^2 \tag{D.2}$$

where

$$r = \frac{E\{XY\} - m_X m_Y}{\sigma_X \sigma_Y} \tag{D.3}$$

is the correlation coefficient. The derivatives in Eq. D.1 and Eq. D.6 are evaluated at $x = m_X$ and $y = m_Y$:

$$\begin{aligned} &\frac{\partial g}{\partial x} = \frac{1}{m_Y}, \quad \frac{\partial g}{\partial y} = -\frac{m_X}{m_Y^2} \\ &\frac{\partial^2 g}{\partial x \partial y} = -\frac{1}{m_Y^2} \\ &\frac{\partial^2 g}{\partial x^2} = 0, \quad \frac{\partial^2 g}{\partial y^2} = \frac{2m_X}{m_Y^3} \end{aligned} \tag{D.4}$$

Replacing Eq. D.4 in Eq. D.1 and D.6 we obtain (see also [35])

$$m_T \approx \frac{m_X}{m_Y} - \frac{r\sigma_X\sigma_Y}{m_Y^2} + \frac{m_X\sigma_Y^2}{m_Y^3} \tag{D.5}$$

$$\sigma_T^2 \approx \frac{\sigma_X^2}{m_Y^2} - \frac{2rm_X\sigma_X\sigma_Y}{m_Y^3} + \frac{m_X^2\sigma_Y^2}{m_Y^4} \tag{D.6}$$

D.1 Test T_1^i

For the scenario without distortion (H_0), the test T_1^i is given by Eq. 5.19

$$T_1^i = \frac{X}{Y} = \frac{n_i - (\overline{Z}_i/\overline{Z}_0)n_0}{(\overline{Z}_0 + n_0)\lambda_1^i} \tag{D.7}$$

The mean $m_X = 0$ and $m_Y = \overline{Z}_0\lambda_1^i$. The variances of X and Y are

$$\sigma_X^2 = \frac{N_0}{T}\left[R_s(0)(1+\rho_i^2) - 2\rho_i R_s(i\Delta)\right] \tag{D.8}$$

$$\sigma_Y^2 = \left[\lambda_1^i\right]^2 \frac{N_0}{T} R_s(0) \tag{D.9}$$

Besides, $E\{XY\} = 0$ yielding $r = 0$. Using these results, we obtain for the mean and variance of the r.v. T_1^i

$$m_{T_1^i} = 0 \tag{D.10}$$

$$\sigma_{T_1^i}^2 = \frac{(1+\rho_i^2)R_s(0) - 2\rho_i R_s(i\Delta)}{2(C/N_0)TR_A^2(0)\left[\lambda_1^i\right]^2} \tag{D.11}$$

D.2 Test T_2^i

For the scenario without distortion (H_0), the test T_2^i is given by Eq. 5.31

$$T_2^i = \frac{X}{Y} = \frac{n_{-i} - n_i}{\overline{Z}_0 + n_0\lambda_2^i} \tag{D.12}$$

The mean $m_X = 0$ and $m_Y = \overline{Z}_0\lambda_2^i$. The variances of X and Y are

$$\sigma_X^2 = E\{(n_{-i} - n_i)^2\} = 2\frac{N_0}{T}[R_s(0) - R_s(2i\Delta)] \tag{D.13}$$

$$\sigma_Y^2 = \left[\lambda_2^i\right]^2 \frac{N_0}{T} R_s(0) \tag{D.14}$$

Besides, $E\{XY\} = 0$ yielding $r = 0$. Using these results, we obtain for the mean and variance of the r.v. T_2^i

$$m_{T_2^i} = 0 \tag{D.15}$$

$$\sigma^2_{T_2^i} = \frac{R_s(0) - R_s(2i\Delta)}{(C/N_0)TR_A^2(0)\left[\lambda_2^i\right]^2} \tag{D.16}$$

D.3 Test T_3^i

For the scenario without distortion (H_0), the test T_3^i is given by Eq. 5.38

$$T_3^i = \frac{X}{Y} = \frac{n_{-i} + n_i - 2\rho_i n_0}{\overline{Z}_0 + n_0\lambda_3^i} \tag{D.17}$$

The mean $m_X = 0$ and $m_Y = \overline{Z}_0\lambda_3^i$. The variances of X and Y are

$$\sigma_X^2 = \frac{N_0}{T}\left[(2 + 4\rho_i^2)R_s(0) + 2R_s(2i\Delta) - 8\rho_i R_s(i\Delta)\right] \tag{D.18}$$

$$\sigma_Y^2 = \left[\lambda_3^i\right]^2 \frac{N_0}{T}R_s(0) \tag{D.19}$$

Then

$$E\{XY\} = 2\lambda_3^i\frac{N_0}{T}[R_s(i\Delta) - R_s(0)] \tag{D.20}$$

yielding for the correlation coefficient

$$r = \frac{2[R_s(i\Delta)/R_s(0) - 1]}{\sqrt{2 + 4\rho_i^2 + 4R_s(2i\Delta)/R_s(0) - 8\rho_i R_s(i\Delta)/R_s(0)}} \tag{D.21}$$

Using these results, we obtain for the mean and variance of the r.v. T_3^i

$$m_{T_3^i} \approx \frac{R_s(0) - R_s(i\Delta)}{\lambda_3^i(C/N_0)TR_A^2(0)} \approx 0 \tag{D.22}$$

$$\sigma^2_{T_3^i} \approx \frac{(1 + 2\rho^2)R_s(0) + R_s(2i\Delta) - 4\rho_i R_s(i\Delta)}{(C/N_0)TR_A^2(0)[\lambda_3^i]^2} \tag{D.23}$$

Appendix E

Halt criterion for the Monte Carlo simulation

An important issue in Monte Carlo simulation is to determine how many runs are necessary to achieve a given accuracy for the probability of false alarm and missing detection probabilities. The brute force solution would be to use a very large number of runs. However, the larger the number of runs, the longer the run time. Thus, a trade off between the run time and accuracy must be taken into consideration.

Assuming N independent trials such that the number of error events n is binomially distributed, B(N,p), where p is the a priori probability of error event, for a given N, the estimate of p is given by $\hat{p} = n/N$ [36].

Consider now the random variable X that follows a binomial distribution with parameters N and p. The probability of having exactly n error events, with n = 0,1,...,N is

$$\text{prob}\{X \ = \ n\} = \binom{N}{n} p^n (1-p)^{N-n} \tag{E.1}$$

where

$$\binom{N}{n} = \frac{N!}{(N-n)!n!} \tag{E.2}$$

X has mean $E\{X\} = Np$ and variance $\sigma^2 = Np(1-p)$ [34].

Because $B(N,p)$ is a binomial distribution, it is not possible to determine a confidence interval with exactly a specified confidence level $1-\alpha$, with $\alpha << 1$. However, it is possible to obtain an interval with a coverage probability of, at least, $1-\alpha$. Most introductory statistic textbooks present the confidence interval based on the normal approximation. Nevertheless, this approximation fails when the a priori probability, p, is close to 0 (as is the case) [37].

The strategy herein followed, is the Clopper-Pearson "exact" confidence interval for p, that is obtained by solving [38]

$$\sum_{k=n}^{N} \binom{N}{k} h_1^k (1-h_1)^{N-k} = \frac{\alpha}{2} \tag{E.3}$$

and

$$\sum_{k=0}^{n} \binom{N}{k} h_2^k (1-h_2)^{N-k} = \frac{\alpha}{2} \tag{E.4}$$

where h_1 and h_2 are, respectively, the lower and upper limit of the confidence interval and $1-\alpha$ is the confidence level. When $N \to \infty$ and $p \to 0$, such that $Np = \lambda$ (constant), we can obtain for Eq. E.3 and E.4 [34]

$$\sum_{k=n}^{N} \binom{N}{k} h_1^k (1-h_1)^{N-k} \approx \sum_{k=n}^{N} \binom{N}{k} \frac{\lambda_1^k}{k!} \exp(-\lambda_1) = \frac{\alpha}{2} \tag{E.5}$$

and

$$\sum_{k=0}^{n} \binom{N}{k} h_2^k (1-h_2)^{N-k} \approx \sum_{k=0}^{n} \binom{N}{k} \frac{\lambda_2^k}{k!} \exp(-\lambda_2) = \frac{\alpha}{2} \tag{E.6}$$

with

$$h_1 = \frac{\lambda_1}{N}, \quad h_2 = \frac{\lambda_2}{N} \tag{E.7}$$

Normalizing these limits by $p = n/N$ yields

$$\rho_1 = \frac{h_1}{p} = \frac{\lambda_1}{n}, \quad \rho_2 = \frac{h_2}{p} = \frac{\lambda_2}{n} \tag{E.8}$$

The confidence interval is, thus, given by

$$\rho_1 p \leq \hat{p} \leq \rho_2 p \tag{E.9}$$

The length of the confidence interval is $L = (\rho_2 - \rho_1)p$.

Table E.1 contains the lower and upper factors ρ_1 and ρ_2 for different numbers of error events n and confidence levels $1-\alpha$. As expected, it can be seen that by increasing the number of available error events, the confidence intervals become narrower and better accuracies are obtained. For instance, selecting $\alpha = 0.05$ and $L = 0.04p$ requires $n \approx 100$. This provides the halt criterion for the Monte Carlo simulation: the simulation process is stopped after 100 error events are obtained. For a typical missing detection probability $P_{md} = 10^{-3}$, the average of runs is $N = 100/10^{-3} = 10^5$.

Table E.1: Confidence intervals for the estimation of p.

	$\alpha = 0.1$		$\alpha = 0.05$		$\alpha = 0.01$	
n	ρ_1	ρ_2	ρ_1	ρ_2	ρ_1	ρ_2
10	0.543	1.696	0.480	1.839	0.372	2.140
25	0.695	1.397	0.647	1.476	0.560	1.640
50	0.779	1.266	0.742	1.318	0.673	1.425
100	0.841	1.181	0.814	1.216	0.761	1.288
125	0.858	1.160	0.832	1.191	0.785	1.254